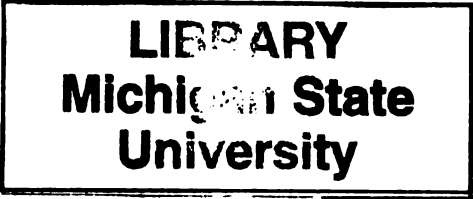




THESIS  
1  
2001



This is to certify that the  
dissertation entitled

**ADAPTIVE COMPENSATION OF SENSOR RUNOUT AND MASS  
UNBALANCE IN ACTIVE MAGNETIC BEARINGS**

presented by

*Joga Dharma Setiawan*

has been accepted towards fulfillment  
of the requirements for

Ph.D. degree in Mechanical Engineering

  
Major professor

Date 5/8/01

**PLACE IN RETURN BOX to remove this checkout from your record.  
TO AVOID FINES return on or before date due.  
MAY BE RECALLED with earlier due date if requested.**

DATE DUE	DATE DUE	DATE DUE
<del>FEB 25 2004</del>		

ADAPTIV

IN

**ADAPTIVE COMPENSATION OF SENSOR RUNOUT  
AND MASS UNBALANCE  
IN ACTIVE MAGNETIC BEARINGS**

By

*Joga Dharma Setiawan*

A DISSERTATION

Submitted to  
Michigan State University  
in partial fulfillment of the requirements  
for the degree of

DOCTOR OF PHILOSOPHY

Department of Mechanical Engineering

2001

## ADAPTI

Active mag  
speed, high-per  
tactless and fri  
they require ca  
niques have bee  
SRO) has been  
periodic disturb  
unbalance comp

To improve  
time an adaptiv  
individually and  
metric center. I  
perurbed to cre  
of the harmonic

## ABSTRACT

# ADAPTIVE COMPENSATION OF SENSOR RUNOUT AND MASS UNBALANCE IN ACTIVE MAGNETIC BEARINGS

By

*Joga Dharma Setiawan*

Active magnetic bearings (AMBs) have increasingly become the choice for high-speed, high-performance rotating machinery because they provide the scope for contactless and frictionless operation. Since magnetic bearings are open-loop unstable, they require careful control system design. Although general feedback control techniques have been proposed for precise shaft levitation, the problem of sensor runout (SRO) has been largely overlooked due to its similarities with unbalance in creating periodic disturbances. Furthermore, the important problem of synchronous SRO and unbalance compensation has not been adequately investigated.

To improve the accuracy of magnetically levitated rotors, we propose for the first time an adaptive control framework that can compensate SRO and unbalance, both individually and simultaneously, while providing shaft stabilization about the geometric center. In our approach, bias currents in the magnetic coils are periodically perturbed to create persistency of excitation that guarantees individual identification of the harmonic components of the synchronous disturbances. Through feed-forward

cancellation of the  
vides geometric co  
values. While Ly  
a solid theoretica  
establish the simp  
applies to both S  
are expected to b

cancellation of the disturbances and careful control system design, the algorithm provides geometric center stabilization that is robust to uncertainty in plant parameters values. While Lyapunov stability theory and its derived passivity formalism provide a solid theoretical framework for the algorithm, corroborating experimental results establish the simplicity of the design and implementation procedure. The algorithm applies to both SISO and MIMO systems involving a rigid rotor and future studies are expected to broaden its applicability to flexible rotor models.

Copyright © by  
Joga Dharma Setiawan  
2001

**To my parents**

I thank all  
of their contri  
complete. In  
Mukherjee, fo  
a great pleas  
Clark J. Rad  
Shaw, for his  
nonlinear con  
magnetism an

My deepe  
University of  
valuable reso  
movers in the

I thank Re  
during exper  
read my type

I would lik  
care, and love

## ACKNOWLEDGMENTS

I thank all those who contributed to the completion of this research. Without each of their contributions, this work would have been more difficult, if not impossible, to complete. In particular, the author wishes to thank my major advisor, Dr. Ranjan Mukherjee, for his support, guidance, enthusiasm, and patience. It has always been a great pleasure to work with him. I thank the members of the Ph.D committee: Dr. Clark J. Radcliffe, for sharing his mechatronics experimental experience; Dr. Steve Shaw, for his input on rotor vibration; Dr. Hassan M. Khalil, for making sure the nonlinear control aspects went smoothly; and Dr. Mahanti, for his input on electro-magnetism and its principles.

My deepest gratitude goes to Dr. Eric H. Maslen, from the ROMAC Laboratory, University of Virginia, whose expertise in active magnetic bearings has been an invaluable resource. His kindhearted assistance and encouragement have been prime movers in the completion of this research.

I thank Roy Bailiff, a very reliable staff in the department. His prompt assistance during experimental set-up is greatly appreciated. I thank Craig Gunn, who proof-read my typo-ridden first draft, and focused my later editions.

I would like to give special thanks to my wife Esti K. Wardhani for her faithfulness, care, and love, and to my parents, who have morally supported me throughout.

List of Tables

List of Figures

**1** Introduction

1.1 Motiv

1.2 Litera

1.3 Scope

1.4 Nomen

**2** Magnetic

2.1 Intro

2.2 Singl

2.3 Stand

2.4 Sense

2.5 Off-l

2.6 Unba

2.7 Defi

**3** Adaptive

3.1 Intro

3.2 Cho

3.3 Pro

3.4 Rob

3.5 Con

3.6 Sim

3.6.1

3.6.2

3.7 Exp

3.8 Exp

3.9 Sur

# TABLE OF CONTENTS

<b>List of Tables</b>	<b>x</b>
<b>List of Figures</b>	<b>xi</b>
<b>1 Introduction</b>	<b>1</b>
1.1 Motivation . . . . .	1
1.2 Literature Review . . . . .	2
1.3 Scope and Content of the Thesis . . . . .	4
1.4 Nomenclature . . . . .	6
<b>2 Magnetic Bearing Modeling</b>	<b>9</b>
2.1 Introduction . . . . .	9
2.2 Single Degree-of-Freedom Model . . . . .	9
2.3 Standard PD Controller . . . . .	12
2.4 Sensor Runout (SRO) Disturbance . . . . .	13
2.5 Off-line SRO Identification . . . . .	13
2.6 Unbalance Verification Using a Trial Mass . . . . .	15
2.7 Definition of Most Commonly Used Terms . . . . .	15
<b>3 Adaptive Sensor Runout Compensation (ASRC)</b>	<b>18</b>
3.1 Introduction . . . . .	18
3.2 Choice of Adaptive Controller . . . . .	18
3.3 Proof of Stability and Parameter Convergence . . . . .	20
3.4 Robustness to Parameter Uncertainties . . . . .	24
3.5 Convergence Rate Analysis Using Averaging . . . . .	28
3.6 Simulation Results . . . . .	31
3.6.1 Known Plant Parameters Case . . . . .	31
3.6.2 Uncertain Plant Parameters Case . . . . .	33
3.7 Experimental Procedure . . . . .	37
3.8 Experimental Results . . . . .	41
3.9 Summary and Remarks . . . . .	44

4 Simultaneous  
Using M

4.1 Intro

4.2 Con

4.3 Sim

4.4 Pra

4.5 Sum

5 Simultaneous  
via Bias

5.1 Intro

5.2 Ada

5.3 Pro

5.4 Rob

5.4.1

5.4.2

5.4.3

5.5 Sim

5.6 Sim

5.7 Expe

5.8 Expe

5.9 Inter

5.10 Sum

6 Extension

6.1 Intro

6.2 MIN

6.3 ASR

6.3.1

6.3.2

6.4 SRU

6.4.1

6.4.2

6.5 ASR

6.6 Sum

7 Conclusion

7.1 Reser

<b>4</b>	<b>Simultaneous Sensor Runout and Unbalance Compensation (SRUC)</b>	
	<b>Using Multiple Speeds</b>	<b>47</b>
4.1	Introduction . . . . .	47
4.2	Controller Design . . . . .	47
4.3	Simulation Results . . . . .	53
4.4	Practical Implementation Issues . . . . .	54
4.5	Summary and Remarks . . . . .	56
<b>5</b>	<b>Simultaneous Sensor Runout and Unbalance Compensation (SRUC)</b>	
	<b>via Bias Current Excitation (BCE)</b>	<b>57</b>
5.1	Introduction . . . . .	57
5.2	Adaptive Control with Bias Current Excitation . . . . .	58
5.3	Proof of Stability and Parameter Convergence . . . . .	62
5.4	Robustness to Parameter Uncertainties . . . . .	66
	5.4.1 Mass Uncertainty . . . . .	66
	5.4.2 Magnetic Stiffness Uncertainty . . . . .	69
	5.4.3 Actuator Gain Uncertainty . . . . .	71
5.5	Simulation Results . . . . .	72
5.6	Simulation Studies of the Convergence Rate . . . . .	78
5.7	Experimental Procedure . . . . .	81
5.8	Experimental Results . . . . .	83
5.9	Interpretation of Experimental Results . . . . .	88
5.10	Summary and Remarks . . . . .	92
<b>6</b>	<b>Extension to MIMO Systems</b>	<b>94</b>
6.1	Introduction . . . . .	94
6.2	MIMO Model of Magnetic Bearing with Rigid Rotor . . . . .	94
6.3	ASRC for 2-DOF systems . . . . .	100
	6.3.1 Controller Design . . . . .	100
	6.3.2 Simulation Results . . . . .	103
6.4	SRUC-BCE for 2-DOF Systems . . . . .	103
	6.4.1 Controller Design . . . . .	103
	6.4.2 Simulation Results . . . . .	107
6.5	ASRC-BCE for 2-DOF systems . . . . .	108
6.6	Summary and Remarks . . . . .	111
<b>7</b>	<b>Conclusions</b>	<b>114</b>
7.1	Research Summary . . . . .	114

7.2 Futu

## Appendices

### A. Exper:

A.1 Y

A.2 S

A.3 I

A.4 I

A.5 .

A.6 I

A.7 I

A.8 .

### B. Analy

B.1 .

B.2 S

B.3 S

### C. Param

C.1 C

C.2 C

### D. Passiv

## Bibliograph

7.2 Future Work . . . . .	116
<b>Appendices</b>	<b>118</b>
A. Experimental Set-up . . . . .	118
A.1 Magnetic Bearing Set-Up . . . . .	118
A.2 Structural-Dynamic Analysis of Two-Bearing Rotor . . . . .	118
A.3 Plant Parameters . . . . .	123
A.4 Power Amplifier Data . . . . .	126
A.5 Analog PD Control Circuit . . . . .	127
A.6 Radial Position Sensor . . . . .	129
A.7 Digital Signal Processors . . . . .	129
A.8 Absolute Encoder . . . . .	130
B. Analysis of Persistently Exciting Condition . . . . .	131
B.1 ASRC: Equation 3.14 . . . . .	132
B.2 SRUC Using Multiple Speeds: Equation 4.25 . . . . .	132
B.3 SRUC-BCE: Equation 5.41 . . . . .	133
C. Parameter Convergence Using Averaging Method . . . . .	138
C.1 Convergence Rate of ASRC . . . . .	138
C.2 Convergence Rate of SRUC-BCE . . . . .	140
D. Passivity . . . . .	144
<b>Bibliography</b>	<b>152</b>

## LIST OF TABLES

3.1	Time constants of the averaged system . . . . .	30
3.2	Parameters for ASRC simulation . . . . .	32
3.3	Numerical values of variables assuming $m, c, K_s, K_c$ are over-estimated by 100% in the actual case . . . . .	33
4.1	Parameters for Simulation . . . . .	53
5.1	Experimental results with the balance disk located at the rotor midspan: part (a) . . . . .	85
5.2	Experimental results with the balance disk located at the rotor midspan: part (b) . . . . .	86
5.3	Experimental results with the balance disk located closer to bearing B: part (a) . . . . .	90
5.4	Experimental results with the balance disk located closer to bearing B: part (b) . . . . .	91
6.1	Simulation parameters for 2-DOF magnetic bearing systems . . . . .	102
A.1	Two-bearing rotor data . . . . .	119
A.2	Free-free undamped natural frequencies of rotor . . . . .	121
A.3	Magnetic bearing parameters for single-DOF Model . . . . .	123
A.4	Servo amplifier specifications . . . . .	127

## LIST OF FIGURES

2.1	Diagram of a typical active magnetic bearing system . . . . .	10
2.2	Single-DOF model of magnetic bearing with rotor schematic . . . . .	11
2.3	Off-line SRO identification . . . . .	14
2.4	Unbalance verification using a trial mass . . . . .	15
3.1	Block diagram of magnetic bearing system with ASRC . . . . .	19
3.2	Block diagram of closed-loop system in the presence of uncertain plant parameters . . . . .	25
3.3	Estimated parameters of sensor runout . . . . .	34
3.4	Stabilization of rotor geometric center using ASRC . . . . .	35
3.5	Transients of currents of ASRC . . . . .	35
3.6	Averaged approximation of ASRC . . . . .	36
3.7	Time constants of estimated parameters in ASRC . . . . .	37
3.8	Sensor runout estimation in uncertain plant . . . . .	38
3.9	Stabilization of rotor geometric center using ASRC in uncertain plant	38
3.10	Transients of currents of ASRC in uncertain plant . . . . .	39
3.11	Averaged approximation of ASRC in uncertain plant . . . . .	39
3.12	Time constants of estimated parameters in uncertain plant . . . . .	40
3.13	Trajectory of estimated rotor geometric center and regenerated sensor signals . . . . .	42
3.14	Trajectory of estimated Fourier coefficients of sensor runout . . . . .	43
3.15	Trajectory of control currents . . . . .	43
3.16	Trajectory of estimated rotor geometric center and regenerated sensor signals . . . . .	44
3.17	Trajectory of estimated Fourier coefficients of sensor runout . . . . .	45
3.18	Trajectory of control currents . . . . .	45
4.1	Block diagram of SRO and unbalance compensation framework . . . . .	48
4.2	Geometric center $x$ and sensor signal with runout $x_s$ . . . . .	54
4.3	Estimated Fourier coefficients . . . . .	55
5.1	Block diagram of SRUC via bias current excitation . . . . .	61
5.2	Geometric center $x$ and sensor signal with runout $x_s$ . . . . .	73
5.3	Estimated Fourier coefficients . . . . .	74
5.4	Top and bottom bias currents . . . . .	74

5.5 Eff.  
5.6 Eff.  
5.7 Eff.  
5.8 Eff.  
5.9 Eff.  
5.10 Eff.  
5.11 Eff.  
5.12 Time  
5.13 Time  
6.1 Free  
6.2 Geor  
for 2  
6.3 High  
6.4 Geor  
BCE  
6.5 High  
6.6 Geor  
BCI  
6.7 High  
A.1 Ma  
A.2 Pic  
A.3 Dir  
A.4 Fre  
A.5 Ro  
A.6 Bo  
A.7 3-I  
A.8 M  
A.9 M  
A.10 B  
A.11 A  
A.12 B  
A.13 S  
D.1 F

5.5	Effect of mass uncertainty to SRUC-BCE . . . . .	75
5.6	Effect of magnetic stiffness uncertainty to SRUC-BCE . . . . .	76
5.7	Effect of actuator gain uncertainty to SRUC-BCE . . . . .	77
5.8	Effect of excitation amplitude; $f_e = 0.5f$ . . . . .	79
5.9	Effect of excitation amplitude when $f_e \neq 0.5f$ . . . . .	79
5.10	Effect of excitation frequency . . . . .	80
5.11	Effect the number of excitation harmonics . . . . .	80
5.12	Time history of geometric center $x$ and position sensor signal $x_s$ . . .	85
5.13	Time trace of estimated Fourier coefficients for Expt. 2 in Table 5.1 .	87
6.1	Freebody diagram of a magnetically levitated rigid-rotor . . . . .	95
6.2	Geometric position, sensor signal, and DC component error of ASRC for 2-DOF system model . . . . .	104
6.3	Higher harmonics error of ASRC for 2-DOF system model . . . . .	105
6.4	Geometric position, sensor signal, and DC component error of SRUC- BCE for 2-DOF system model . . . . .	109
6.5	Higher harmonics error of SRUC-BCE for 2-DOF system model . . .	110
6.6	Geometric position, sensor signal and DC component error of ASRC- BCE for 2-DOF system model . . . . .	112
6.7	Higher harmonics error of ASRC-BCE for 2-DOF system model . . .	113
A.1	Magnetic bearing rig schematic . . . . .	118
A.2	Picture of magnetic bearing set-up . . . . .	119
A.3	Dimension of two-bearing rotor with balanced disk . . . . .	119
A.4	Free-free modes shapes of rotor . . . . .	120
A.5	Rotor critical speed map . . . . .	120
A.6	Bode plot of single-DOF magnetic bearing model . . . . .	124
A.7	3-D Plot of magnetic force surface . . . . .	124
A.8	Magnetic force vs. Position . . . . .	125
A.9	Magnetic force vs. Current . . . . .	125
A.10	Bode plot of servo amplifier . . . . .	126
A.11	Analog PD control circuit . . . . .	127
A.12	Bode plot of analog PD controller $V_{out}(S)/V_{in}(s)$ . . . . .	128
A.13	Simulink block diagram for the absolute encoder . . . . .	130
D.1	Feedback configuration for passivity analysis . . . . .	145

# CHAP

## Introd

### 1.1 Mo

Active magne

less operation

higher efficien

include the e

suitability for

characteristic

tive features.

in rotating s

wheels, preci

The desi

plines inclu

back control

an open-loop

of the feedb

Moreover, t

position sen

circuits or d

# CHAPTER 1

## Introduction

### 1.1 Motivation

Active magnetic bearings (AMBs) levitate rotors and enable contactless and frictionless operation. They have a number of advantages over conventional bearing including higher efficiency, longer life, and ability to operate at higher rpm. Other advantages include the elimination of mechanical maintenance of the bearing and lubrication, suitability for clean or vacuum room operation, and adjustable stiffness and damping characteristics achieved through active control of bearing forces. Due to the attractive features, magnetic bearings have been implemented in a variety of applications in rotating systems. These applications include flywheel energy storage, momentum wheels, precision machinery, turbomachinery, vacuum pumps, and medical devices.

The design of magnetic bearing systems requires the knowledge of several disciplines including mechanical/rotor dynamics, electromagnetics, electronics and feedback controls. This is due to the fact that a rotor supported by magnetic bearings is an open-loop unstable system, stabilized through feedback control. The integration of the feedback control strategy must carefully consider the dynamics of the rotor. Moreover, the feedback control in magnetic bearings necessitates the knowledge of position sensors with signal conditioning, switching-power amplifier, either analog circuits or digital signal processor (DSP), and magnetic coils as the actuators.

Due to t  
abundant re  
and addition  
In the recent  
areas such as  
as multi-vari  
in order to m  
sensing schem  
zero-power m

This thes  
mance of ma  
turing proces  
to reject the

## 1.2 Li

Periodic dis  
ical to the p  
disturbance  
unbalance r  
axis of iner  
speed. Me  
not comple  
available s  
assembly. S  
sensing sur  
ing surface

Due to the rapid progress in electronics including DSPs technology, there are abundant research problems in AMBs. Performance improvement, cost reduction, and additional design objectives within specific applications are some of the examples. In the recent years, researchers working on magnetic bearings have been focusing in areas such as (1) rotor vibration minimization using modern control method such as multi-variable controls, robust controls, non-linear controls, and adaptive controls in order to minimize rotor vibration; (2) levitation of flexible rotors; (3) robust self-sensing schemes; (4) integration of magnetic bearings with electric motor; and (5) zero-power magnetic bearings using superconductor materials.

This thesis focuses on utilizing modern control methods to improve the performance of magnetic bearings without demanding additional precision in the manufacturing process. In particular, this thesis explores a new adaptive control framework to reject the effect of the most common periodic disturbances in AMBs.

## 1.2 Literature Review

Periodic disturbances are common in rotating machinery. Such disturbances are critical to the performance of systems using AMBs. The dominant sources of periodic disturbance in magnetic bearings are mass unbalance and sensor runout (SRO). Mass unbalance results from lack of alignment between the geometric axis and the principal axis of inertia, which results in an unbalance force synchronous with rotor angular speed. Mass unbalance can be significantly reduced in industrial applications, if not completely eliminated by rotor balancing. In comparison, sensor runout is unavoidable since it results from manufacturing imperfections in the magnetic bearing assembly. Specifically, SRO disturbance originates from a lack of concentricity of the sensing surface and non-uniform electrical or magnetic properties around the sensing surface. Unlike mass unbalance, SRO also generates a disturbance at multiple

harmonics of

runout distu

Stabilization

compensatio

Though

combined ur

compensatio

pensation has

drawback of

which can re

[15, 3, 24]. A

forward cont

estimated an

resemblance

consideration

closed-loop s

Park [24] pro

that compen

[19] and out

rotor stabili

Though

stabilization

tering, accep

geometric ce

problems we

tion about r

disturbance

harmonics of angular speed. Despite differences between mass unbalance and sensor runout disturbances, the control objective for their compensation is often similar. Stabilization of the rotor about the geometric center, which is the objective for SRO compensation, is often the objective for unbalance compensation.

Though few researchers [11, 33] have addressed the problem of compensation of combined unbalance and SRO disturbances, there exists a large volume of research on compensation of individual disturbances. Some of the early work on unbalance compensation has been based on the insertion of a notch filter in the control loop [2]. The drawback of this approach stems from negative phase of the notch transfer function, which can reduce stability margin of the closed-loop system and lead to instability [15, 3, 24]. Another approach for periodic disturbance cancellation is adaptive feed-forward control [34, 9], where Fourier coefficients of the disturbance are continually estimated and used for cancellation. These adaptive controllers, operationally bear resemblance to the notch filters [24] and can result in instability if designed without a consideration for the underlying structure of the system. To preserve stability of the closed-loop system, Herzog et al. [7] developed the generalized notch filter and Na and Park [24] proposed a variation of the least mean square algorithm. Other approaches that compensate unbalance while ensuring stability include adaptive auto-centering [19] and output regulation with internal stability [21]. Both these approaches achieve rotor stabilization about the center-of-mass.

Though unbalance compensation has been widely studied with the objective of stabilization about the mass center, most users and vendors push for geometric centering, accepting that the real objective is to avoid seal or aero tip collisions. While geometric center stabilization has been addressed by a few researchers [8, 37] both problems were investigated in references [28, 22]. These results indicate that stabilization about mass center or geometric center can be achieved through cancellation of disturbance in the current signal or the displacement signal, respectively. In a general

and experim  
form of rotor  
of the pre-c  
the algorithm  
results were  
into two ind  
cessfully, th  
Some of the  
control desi

Unfortun  
selves to run  
lem, widely a  
of observabil  
distinguish b  
plant or its  
rotor angular  
most applica

### 1.3 Sc

Our approach  
seen applicat  
bearings. The  
geometric ce  
ually identify  
persistence of  
the regressor

and experimental approach for disturbance attenuation by Knospe et al. [16, 17], any form of rotor vibration that can be measured can be attenuated using pseudo-inverse of the pre-computed influence coefficient matrix. The stability and performance of the algorithm in the presence of uncertainties were investigated, and experimental results were used to demonstrate effectiveness. The method decouples the problem into two independent control tasks; and while it has been demonstrated to work successfully, there is no theoretical basis for stability of the two interacting processes. Some of the other approaches employed for unbalance compensation include robust control designs [6, 30], Q-parameterization control [23], and neural networks [27].

Unfortunately, most of the approaches found in the literature do not lend themselves to runout estimation in the presence of significant mass unbalance. This problem, widely acknowledged in the literature but essentially unsolved, stems from a lack of observability of disturbances with the same frequency content. A credible way to distinguish between these disturbances is to perturb the operating conditions of the plant or its parameters. However, recent studies [11, 33] that propose variation in rotor angular speed as a means to enhance observability may not be acceptable for most applications.

### **1.3 Scope and Content of the Thesis**

Our approach to the problem is based on traditional adaptive control designs that has seen applications with a variety of electromechanical systems [4, 31] but not magnetic bearings. The objective of rotor stabilization is to precisely spin the rotor about the geometric center in the presence of SRO and unbalance. In our approach, we individually identify synchronous mass unbalance and SRO at constant rotor speed through persistence of excitation. Our adaptive control framework enable us to uniquely excite the regressor vector, if necessary, to provide the persistently exciting (PE) condition.

It is widely  
asymptotic  
level of robu

The thes  
and unbalan

An off-line S  
adaptive alg  
used variabl

3 an adaptiv  
stability, par  
averaging an

and experim  
the challeng

of adaptive c  
a solution to

currents. Th  
convergence

simulation an  
the adaptive

bearing syst  
for future res

It is widely known in adaptive control field that PE conditions can contribute to an asymptotic convergence of estimated parameters to the true values and provide some level of robustness [25].

The thesis is organized as follows. In Chapter 2 we introduce the problem of SRO and unbalance using a simplified single-degree of freedom magnetic bearing model. An off-line SRO identification that is useful for verification of the results given by adaptive algorithms is also presented. In Chapter 2 we include the most commonly used variables to avoid repeating their definition in the next chapters. In Chapter 3 an adaptive sensor runout compensation (ASRC) is presented including proof of stability, parameter convergence, robustness to plant parameters uncertainty, and averaging analysis to approximate the convergence rate of adaptation. Simulation and experimental results are also provided in Chapter 3. In Chapter 4 we discuss the challenge posed by the combined SRO and unbalance problem and the limitation of adaptive control implementation via multiple angular speeds. Chapter 5 present a solution to the combined SRO and unbalance problem by excitation of the bias currents. The robustness of the algorithm is studied using a passivity analysis. The convergence rate of adaptation is investigated using the averaging method. Both simulation and experimental results are provided in Chapter 5. Chapter 6 extends the adaptive algorithms in Chapters 3 and 5 for implementation in MIMO magnetic bearing systems. Chapter 7 provides concluding remarks and provides suggestions for future research problems.

1.4 No

Arabic Sy

a, b

c

d

e

F

f<sub>a</sub>

f<sub>c</sub>

g

I

I

I<sub>a</sub>

I<sub>r</sub>

i

i<sub>w</sub>

i<sub>x</sub>

k

K

K

l

r

n

p

t

## 1.4 Nomenclature

### Arabic Symbols

$a_i, b_i$	Harmonic Fourier coefficients of sensor runout
$c$	Constant
$d$	Sensor runout disturbance
$\bar{e}$	Weighted sum of position error and velocity error
$F$	Magnetic force
$f_u$	Disturbance force due to mass unbalance
$f_c$	Force due to controlled current
$g$	Gravity
$I$	Controlled current
$\mathbf{I}$	Identity matrix
$I_a$	Axial moment of inertia of rotor
$I_T$	Transverse moment of inertia of rotor
$i$	Harmonic number
$i_{10}$	Top bias current
$i_{20}$	Bottom bias current
$k$	Electromagnetic constant
$K_c$	Actuator gain or current stiffness
$K_s$	Bearing stiffness or position stiffness
$l$	Nominal air gap
$n$	Highest harmonic number considered
$m$	Mass
$p, q$	Harmonic Fourier coefficients of mass unbalance
$t$	Time

$x$	Geometric center position
$x_s$	Position sensor signal
$Y_m$	Regressor Vector
$V$	Lyapunov's function

### **Greek Symbols**

$\delta$	Bias current excitation
$\Delta$	Dimensionless parameter
$\epsilon$	Eccentricity
$\Gamma$	Adaptation gain matrix for SRO part
$\Gamma_u$	Adaptation gain matrix for unbalance part
$\gamma_i$	Adaptation gain constants for SRO part
$\gamma_p, \gamma_q$	Adaptation gain constants for unbalance part
$\lambda$	Error gain
$\omega$	Rotor angular speed
$\phi$	Vector containing Fourier coefficients of sensor runout
$\phi_u$	Vector containing Fourier coefficients of mass unbalanced
$\theta_u$	Phase of mass unbalance

### **Superscripts**

$( )^*$	Nominal value
$( \hat{ } )$	Estimated parameter
$( \tilde{ } )$	Difference between the actual parameter and the estimated parameter

**Acronym**

AMB

ASRC

BCE

DSP

MIMO

PE

RPM

SISO

SPR

SRO

SRUC

**Operator** $\text{Re}(\cdot)$  $(\cdot)^T$  $(\cdot)^{-1}$

## Acronyms

AMB	Active magnetic bearing
ASRC	Adaptive sensor runout compensation
BCE	Bias current excitation
DSP	Digital signal processor
MIMO	Multi-input multi-output
PE	Persistently exciting
RPM	Revolutions per minute
SISO	Single-input single-output
SPR	Strictly positive real
SRO	Sensor runout
SRUC	Sensor runout and unbalance compensation

## Operators

$\text{Re}(\cdot)$	Real part
$(\cdot)^T$	Matrix or vector transpose
$(\cdot)^{-1}$	Matrix inverse

CHAP

Magn

2.1 In

In this cha

our resear

bearing mo

We outline

used term

2.2 S

AMB syste

each of the

a one DOF

are similar

In our stud

the magnet

system with

control sta

sensors mea

# CHAPTER 2

## Magnetic Bearing Modeling

### 2.1 Introduction

In this chapter, we present the dynamics of a rigid rotor magnetic bearing used in our research. We start our study by considering a single degree of freedom magnetic bearing model. The effects of unbalance and sensor runout (SRO) are then introduced. We outline the procedure to manually identify SRO and present the most commonly used terms in the development of our adaptive algorithms.

### 2.2 Single Degree-of-Freedom Model

AMB systems have, in general, five degrees-of-freedom (DOF): two radial DOF at each of the shaft ends and perhaps one axial DOF. However, this chapter considers a one DOF system only by assuming that the dynamics in all four radial directions are similar and can be controlled independently and that the rotor is axially fixed. In our study we assume that the effect of non-collocation between the gap sensor and the magnetic coil actuator is negligible. The typical diagram of a magnetic bearing system with a decentralized feedback control is shown in Figure 2.1. The feedback control stabilizes the rotor position in the following manner. The differential gap sensors measure the location of the center of geometry relative to the stator. After

comparing  
sent to the  
provides the  
magnetic c  
arranged to

P

s

F

Now con  
two degrees  
measured b  
which are b  
the z axis.

where  $m$  is  
magnetic f

comparing the position measurement to the reference position, the resulting error is sent to the compensator. The compensator, which can be an analog circuit or a DSP, provides the necessary command to the power amplifiers that drive currents in the magnetic coils. The signs of the signal sent to the top and the bottom amplifiers are arranged to be opposite to each other.

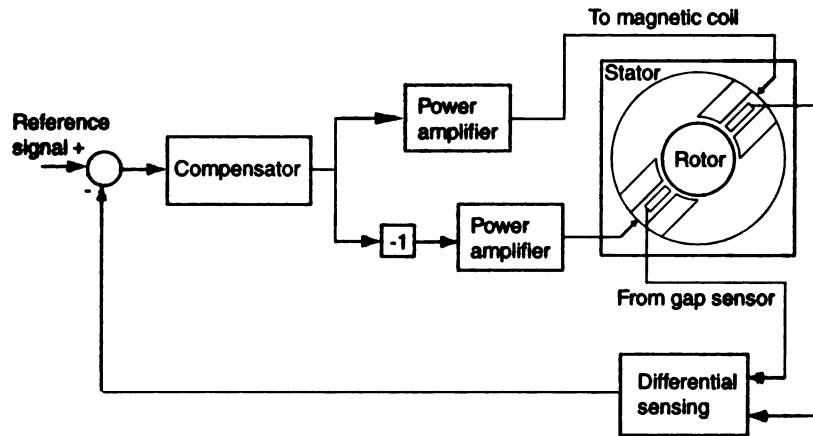


Figure 2.1. Diagram of a typical active magnetic bearing system

Now consider the magnetically levitated rigid rotor in Figure 2.2. The rotor has two degrees-of-freedom along the  $x$  and  $y$  axes; the displacements along these axes are measured by non-contact gap sensors. The dynamics of the rotor along these axes, which are both inclined at  $45^\circ$  with the horizontal, are decoupled but similar. Along the  $x$  axis, one may write

$$m \ddot{x} = F - m \bar{g} + f_u, \quad \bar{g} \triangleq g/\sqrt{2} \quad (2.1)$$

where  $m$  is the mass of the rotor,  $x$  is the position of rotor geometric center,  $F$  is the magnetic force,  $f_u$  is the unbalance force, and  $g$  is the acceleration due to gravity.

Figure 2

The magnetic field

where  $k$  is the  
currents in the  
linearizing Eq.

where  $f_c$  is the  
of the magnetic

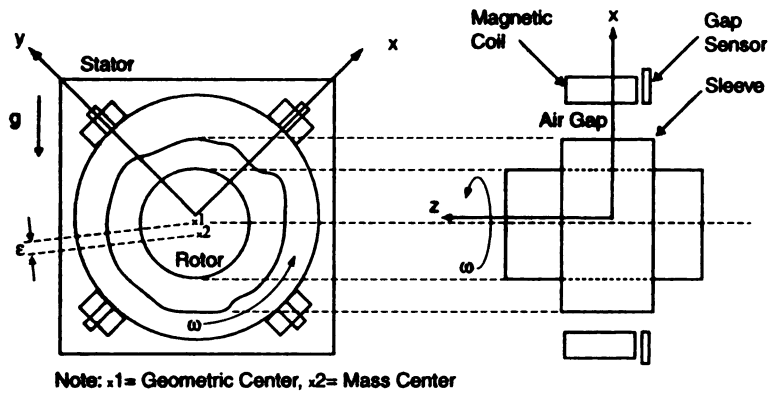


Figure 2.2. Single-DOF model of magnetic bearing with rotor schematic

The magnetic force can be expressed as

$$F = k \left[ \left( \frac{i_{10} + I}{l - x} \right)^2 - \left( \frac{i_{20} - I}{l + x} \right)^2 \right] \quad (2.2)$$

where  $k$  is the magnetic force constant,  $l$  is the nominal air gap,  $i_{10}$ ,  $i_{20}$  are the bias currents in the top and bottom electromagnets, and  $I$  is the control current. By linearizing Eq.(2.2) about  $x = 0$ ,  $I = 0$ , Eq.(2.1) can be written as

$$m \ddot{x} = K_s x + f_c + f_u \quad (2.3)$$

$$f_c \triangleq K_c I \quad (2.4)$$

$$K_s \triangleq 2k (i_{10}^2 + i_{20}^2) / l^3 \quad (2.5)$$

$$K_c \triangleq 2k (i_{10} + i_{20}) / l^2 \quad (2.6)$$

where  $f_c$  is the control force,  $K_s$  and  $K_c$  are the magnetic stiffness and actuator gain of the magnetic bearing respectively. The unbalance force due to mass eccentricity

can be mod

where  $p =$

angular spee

## 2.3 St

Ignoring the

be written a

It can be se

The plant h

To stabl

used as the

where  $K_p >$

closed-loop

$G_c$

In the pres

the origin

degraded a

can be modeled as

$$f_u = m \omega^2 \varepsilon \cos(\omega t + \theta_u) = m \omega^2 [p \sin(\omega t) + q \cos(\omega t)] \quad (2.7)$$

where  $p = -\varepsilon \sin(\theta_u)$  ,  $q = \varepsilon \cos(\theta_u)$  ,  $\theta_u$  is the phase of unbalance,  $\omega$  is the rotor angular speed, and  $\varepsilon$  is the eccentricity of the rotor.

## 2.3 Standard PD Controller

Ignoring the external disturbances in Eq.(2.3), the transfer function of the plant can be written as

$$\frac{X(s)}{I(s)} = \frac{K_c}{ms^2 - K_s} \quad (2.8)$$

It can be seen that without a closed-loop controller the linearized system is unstable. The plant has eigenvalues at  $\pm \sqrt{\frac{K_s}{m}}$ .

To stabilize the rotor, a proportional-derivative (PD) controller  $G_c(s)$  is commonly used as the compensator shown in Figure 2.1.

$$G_c(s) = K_p \left( 1 + \frac{K_d}{K_p} s \right) \quad (2.9)$$

where  $K_p > 0$  is the proportional gain and  $K_d > 0$  is the derivative gain. The stable closed-loop system can be described by

$$G_{cl}(s) = \frac{(K_p + K_d s)K_c}{ms^2 + K_d K_c s + (K_p K_c - K_s)} \quad \text{where } K_p > \frac{K_s}{K_c} \quad (2.10)$$

In the presence of the unbalance, the rotor geometric center will fluctuate around the origin if this standard PD controller is used. The rotor performance is further degraded as the sensor signal contains periodic disturbance due to sensor runout.

## 2.4 Sen

The true locati  
with sensor ru

where,  $d$ , the

In the above

$a, b, i = 1, 2$

## 2.5 Off

In this section

This method

compensation

balance comp

which has to

to be spun a

rotor using a

$E_0 = A_0$ , we

magnitude of

## 2.4 Sensor Runout (SRO) Disturbance

The true location of the rotor's geometric center is not available for a magnetic bearing with sensor runout. Instead, the gap sensors provide the signal  $x_s$ .

$$x_s = x + d \quad (2.11)$$

where,  $d$ , the sensor runout disturbance, can be expressed by the Fourier series

$$d \triangleq a_0 + \sum_{i=1}^n [a_i \sin(i\omega t) + b_i \cos(i\omega t)] = \mathbf{Y}^T \phi \quad (2.12)$$

$$\mathbf{Y} \triangleq [1 \quad \sin(\omega t) \quad \cos(\omega t) \quad \dots \quad \sin(n\omega t) \quad \cos(n\omega t)]^T \quad (2.13)$$

$$\phi \triangleq [a_0 \quad a_1 \quad b_1 \quad \dots \quad a_n \quad b_n]^T \quad (2.14)$$

In the above expression,  $n$  is the number of harmonics,  $a_0$  is the DC component, and  $a_i, b_i, i = 1, 2, \dots, n$ , are the harmonic Fourier coefficients.

## 2.5 Off-line SRO Identification

In this section we present a method for manual off-line identification of sensor runout. This method will be used to verify the accuracy of the on-line adaptive sensor runout compensation scheme (ASRC) in Chapter 3 and the combined sensor runout and unbalance compensation scheme (SRUC) in Chapter 5. Off-line SRO identification, which has to be performed separately for each axis of the bearing, requires the rotor to be spun at low speed to avoid the effects of unbalance. We will first levitate the rotor using a PD controller, as shown in Figure 2.3. Using a DSP to generate function  $E_0 = A_0$ , we close the feedback loop using the signal  $(x_s - E_0)$ . We then adjust the magnitude of  $A_0$  such that  $(x_s - E_0)$  has a zero mean. Once this is accomplished, we

will have ident

Next, we g

angular positi

phase with the

$r_1 - E_0 - E_1$

order harmon

Having id

second harmo

Eventually, w

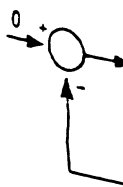
$E =$

This signal c

circuit, to re

we plot  $E_s$  t

significant v



will have identified the DC component of SRO.

Next, we generate the signal  $E_1 = A_1 \sin(\theta_o + \theta_1)$ , where  $\theta_o \triangleq \omega t$  is the rotor angular position obtained from the shaft encoder. We select  $\theta_1$  such that  $E_1$  is in phase with the first harmonic of  $(x_s - E_0)$ . We then change the feedback signal to  $x_s - E_0 - E_1$  and adjust  $A_1$  by trial and error such that  $(x_s - E_0 - E_1)$  has no first order harmonics.

Having identified the first harmonic of SRO, we then sequentially identify the second harmonic  $E_2 = A_2 \sin(2\theta_o + \theta_2)$  and higher order terms in the same manner. Eventually, we will have the complete SRO signal

$$E = (E_0 + E_1 + E_2) = A_0 + A_1 \sin(\theta_o + \theta_1) + A_2 \sin(2\theta_o + \theta_2) \quad (2.15)$$

This signal can be subtracted from the sensor signal  $x_s$ , preferably using an analog circuit, to recover the position of the geometric center,  $E_s = x$ . In our experiments, we plot  $E_s$  to verify rotor stabilization about the geometric center in the presence of significant unbalance.

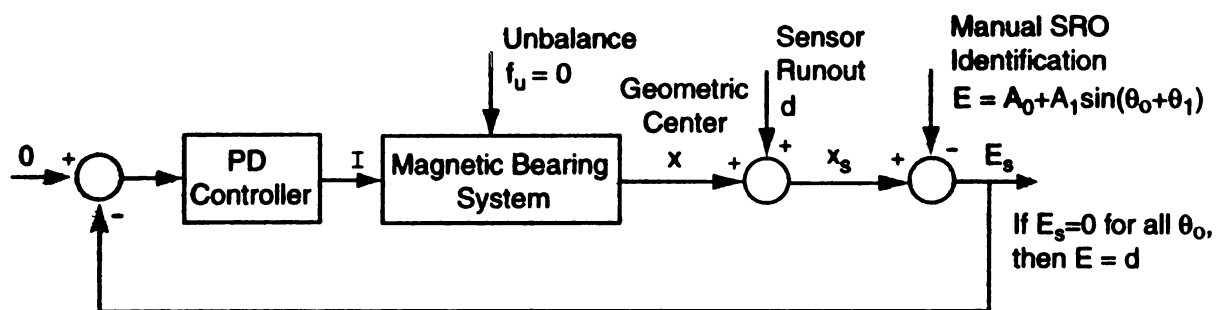
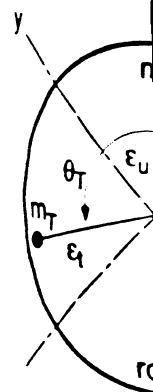


Figure 2.3. Off-line SRO identification

## 2.6 Unb

In this section  
by our adaptiv  
the initial unb  
unbalance usin  
mass, we can v  
a vector sum o  
is explained wi



$m$  = initial

$m_T$  = trial v

## 2.7 Def

In the develop  
be used repea

## 2.6 Unbalance Verification Using a Trial Mass

In this section we outline the procedure for verification of rotor unbalance estimated by our adaptive algorithm. Let  $\epsilon_U, \theta_U$  be the estimated magnitude and phase of the initial unbalance. We will add a trial mass  $m_T$  to the rotor and re-estimate the unbalance using our algorithm. If  $\epsilon_T, \theta_T$  are the magnitude and phase of the trial mass, we can verify the efficacy of our algorithm if the new unbalance vector  $\epsilon_R, \theta_R$  is a vector sum of the initial unbalance and the unbalance due to the trial mass. This is explained with the help of Figure 2.4.

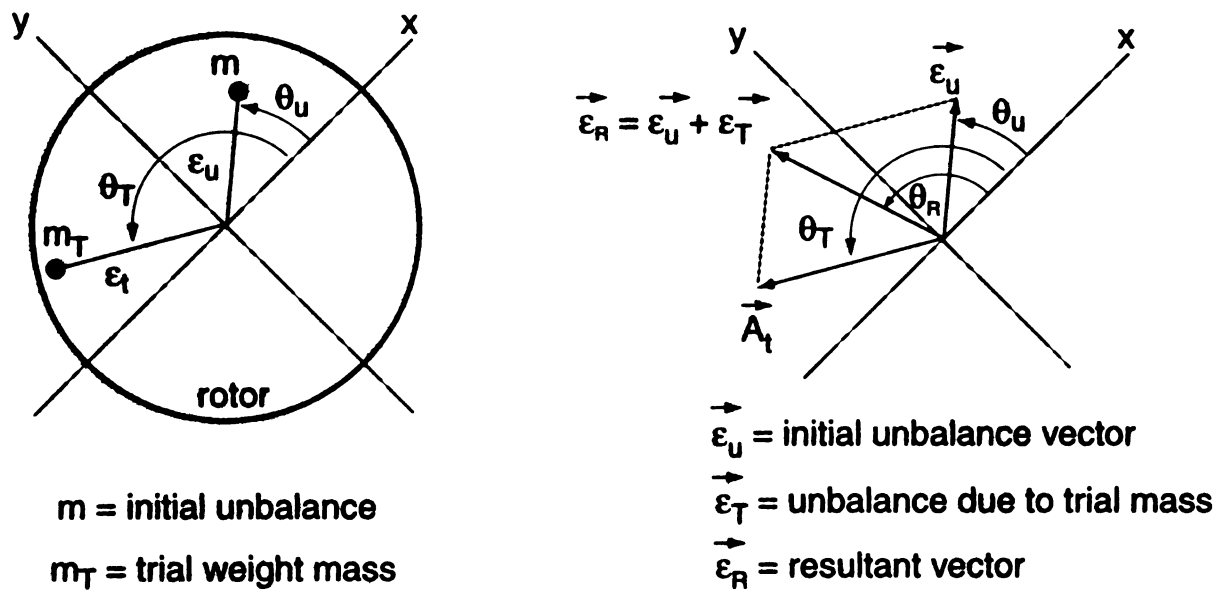


Figure 2.4. Unbalance verification using a trial mass

## 2.7 Definition of Most Commonly Used Terms

In the development of our adaptive algorithms, there are several variables that will be used repeatedly. We introduce the variables here to avoid repeating the same

definition in 11

We define

where

is the estimate

is the estimate

$\hat{b}_i$  are estimate

(2.16).  $\bar{x}$  can a

where,  $\tilde{d}$ , the

relation

The paramet

where  $\tilde{O}_n \triangleq$

$a_1 - \hat{a}_1$ ,  $\tilde{b}_1$

definition in next chapters.

We define the estimated geometric position or position error as

$$\bar{x} \triangleq x_s - \hat{d} \quad (2.16)$$

where

$$\hat{d} \triangleq \hat{a}_0 + \sum_{i=1}^n \left[ \hat{a}_i \sin(i\omega t) + \hat{b}_i \cos(i\omega t) \right] = \mathbf{Y}^T \hat{\phi} \quad (2.17)$$

is the estimated SRO disturbance,

$$\hat{\phi} \triangleq [\hat{a}_0 \quad \hat{a}_1 \quad \hat{b}_1 \quad \dots \quad \hat{a}_n \quad \hat{b}_n]^T \quad (2.18)$$

is the estimated parameter vector of the SRO,  $\hat{a}_0$  is the estimated value of  $a_0$ , and  $\hat{a}_i$ ,  $\hat{b}_i$  are estimated values of  $a_i$ ,  $b_i$ , respectively, for  $i = 1, 2, \dots, n$ . Using Eqs.(2.11) and (2.16),  $\bar{x}$  can also be expressed as

$$\bar{x} = x + \tilde{d} \quad (2.19)$$

where,  $\tilde{d}$ , the error in the estimate of sensor runout disturbance, is given by the relation

$$\tilde{d} \triangleq (d - \hat{d}) = \mathbf{Y}^T \tilde{\phi} \quad (2.20)$$

The parameter error vector  $\tilde{\phi}$  is defined as

$$\tilde{\phi} \triangleq \phi - \hat{\phi} = \begin{pmatrix} \tilde{a}_0 \\ \tilde{\phi}_\alpha \\ \tilde{\phi}_\beta \end{pmatrix} \quad (2.21)$$

where  $\tilde{\phi}_\alpha \triangleq [\tilde{a}_1 \quad \tilde{b}_1]^T$ ,  $\tilde{\phi}_\beta \triangleq [\tilde{a}_2 \quad \tilde{b}_2 \quad \dots \quad \tilde{a}_n \quad \tilde{b}_n]^T$ ,  $\tilde{a}_0 \triangleq (a_0 - \hat{a}_0)$ , and  $\tilde{a}_i \triangleq (a_i - \hat{a}_i)$ ,  $\tilde{b}_i \triangleq (b_i - \hat{b}_i)$ ,  $i = 1, 2, \dots, n$ .

Other mos  
position error

where  $\lambda$  is a p

and the adapt

where  $\gamma_i, i =$

that  $0 < \Delta$

Other most commonly used terms include the weighted sum of the estimated position error and the estimated velocity error

$$\bar{e} \triangleq \dot{\bar{x}} + \lambda \bar{x} \quad (2.22)$$

where  $\lambda$  is a positive constant, the regressor vector

$$\mathbf{Y}_m \triangleq K_s \mathbf{Y} - m \ddot{\mathbf{Y}}, \quad \mathbf{Y}_m \in \mathfrak{R}^{(2n+1)} \quad (2.23)$$

and the adaptation gain for SRO components

$$\Gamma \triangleq \text{diag}(\gamma_0, \gamma_1, \gamma_1, \dots, \gamma_n, \gamma_n), \quad \Gamma \in \mathfrak{R}^{(2n+1) \times (2n+1)} \quad (2.24)$$

where  $\gamma_i$ ,  $i = 0, 1, 2, \dots, n$  are positive constants. These constants are chosen such that  $0 < \Delta < 1$  where  $\Delta$  is a dimensionless parameter defined by

$$\Delta \triangleq \mathbf{Y}^T \Gamma \mathbf{Y}_m = \sum_{i=0}^n \gamma_i (K_s + m(i\omega)^2) \quad (2.25)$$

## CHAPTER

### Adaptive

### (ASRC)

#### 3.1 Introduction

In this section  
in the single d  
absence of ma  
is designed to  
stability and  
the uncertain  
estimated pa  
then verified

#### 3.2 C

Assuming  
becomes

## CHAPTER 3

# Adaptive Sensor Runout Compensation (ASRC)

### 3.1 Introduction

In this section we present an adaptive algorithm to reject the effect of sensor runout in the single degree of freedom magnetic bearing model presented in Chapter 2. In the absence of mass unbalance, the adaptive sensor runout compensation (ASRC) scheme is designed to stabilize the geometric center of the rotor to the origin. The proof of stability and parameter convergence is provided. The robustness of the algorithm to the uncertainties in plant parameters is evaluated and the convergence rate of the estimated parameters is approximated through averaging analysis. The algorithm is then verified through simulations and experiments.

### 3.2 Choice of Adaptive Controller

Assuming the unbalance force,  $f_u$  is negligible, the equation of motion in Eq.(2.3) becomes

$$m \ddot{x} = K_s x + K_c I \quad (3.1)$$

For estimation  
metric center.

along with the

where  $K_1$  and

$\lambda$  are defined

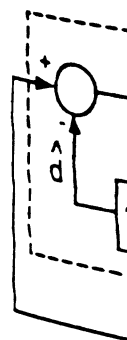
$c$  is a positive

derivative of

shown in Fig

origin in the

are provided



Fig

For estimation and cancellation of sensor runout, and stabilization of the rotor geometric center, we propose the control action

$$I = -\frac{1}{K_c} (K_s \bar{x} + m\lambda \dot{\bar{x}} + c\bar{e}) \quad (3.2)$$

along with the adaptation law

$$\dot{\hat{\phi}} = \Gamma \mathbf{Y}_m \bar{e} \quad (3.3)$$

where  $K_s$  and  $K_c$  are defined in Eqs.(2.5) and (2.6),  $\bar{x}$  is defined in Eq.(2.16),  $\bar{e}$  and  $\lambda$  are defined in Eq.(2.22),  $\Gamma$  is defined in Eq.(2.24),  $\mathbf{Y}_m$  is defined in Eq.(2.23), and  $c$  is a positive constant. The derivative term  $\dot{\bar{x}}$  is assumed available by taking the derivative of the measured signal  $\bar{x}$ . The block diagram of the closed-loop system is shown in Figure 3.1. The controller can stabilize the rotor geometric center to the origin in the presence of sensor runout. The stability proofs and convergence analysis are provided in the next section.

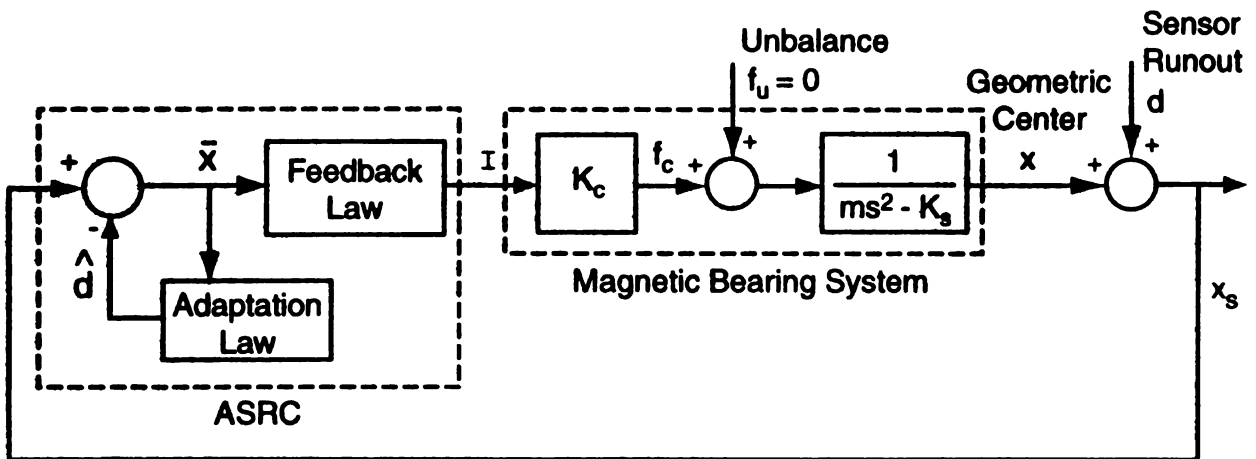


Figure 3.1. Block diagram of magnetic bearing system with ASRC

### 3.3 Pr

From the def

Substituting  
scribed by

Using the rel  
above equatio

The term  $\tilde{d}$  ca

and substitut

knowing the  
dynamics can

### 3.3 Proof of Stability and Parameter Convergence

From the definition of  $\mathbf{Y}$  and  $\mathbf{Y}_m$  in Eqs.(2.13) and (2.23), we can establish

$$\dot{\mathbf{Y}}^T \Gamma \mathbf{Y}_m = 0, \quad \mathbf{Y}^T \Gamma \dot{\mathbf{Y}}_m = 0 \quad (3.4)$$

Substituting Eq.(3.2) into Eq.(3.1), the dynamics of the controlled rotor can be described by

$$m \ddot{x} = -K_s \tilde{d} - m \lambda \dot{x} - c \bar{e} \quad (3.5)$$

Using the relation  $\ddot{x} = \ddot{\tilde{d}} + \lambda \dot{x}$  from Eq.(2.19), and  $\dot{e} = \ddot{x} + \lambda \dot{x}$  from Eq.(2.22), the above equation can be rewritten as

$$m \dot{e} = m \ddot{\tilde{d}} - K_s \tilde{d} - c \bar{e} \quad (3.6)$$

The term  $\ddot{\tilde{d}}$  can be derived from Eq.(2.20)

$$\begin{aligned} \ddot{\tilde{d}} &= \ddot{\mathbf{Y}}^T \tilde{\phi} + 2\dot{\mathbf{Y}}^T \dot{\tilde{\phi}} + \mathbf{Y}^T \ddot{\tilde{\phi}} \\ &= \ddot{\mathbf{Y}}^T \tilde{\phi} + \Delta \dot{e} \end{aligned} \quad (3.7)$$

and substituted in Eq.(3.6) to obtain

$$m(1 - \Delta) \dot{e} = -\mathbf{Y}_m^T \tilde{\phi} - c \bar{e} \quad (3.8)$$

knowing the relations in Eqs.(2.25), (3.3) and (3.4). Thus, the closed loop system dynamics can now be described by

$$\dot{\tilde{x}} = -\lambda \tilde{x} + \bar{e} \quad (3.9a)$$

$$\dot{e} = -\frac{1}{m(1 - \Delta)} \left( \mathbf{Y}_m^T \tilde{\phi} + c \bar{e} \right) \quad (3.9b)$$

The following

**Theorem 3.1**

system.  $(\bar{e}, \bar{o})$

**Proof:** Fr

$(0,0)$ . Therefo

is asymptotica

function

The derivative

Using Eqs.(3.

Since  $V$  i

$(\bar{e}, \bar{o}) \equiv (0,0)$

lemma [13], t

differentiating

that  $\dot{\bar{e}}$  is unif

lemma [13], t

from Eq.(3.9)

$$\dot{\tilde{\phi}} = \Gamma \mathbf{Y}_m \bar{e} \quad (3.9c)$$

The following observations can now be made with respect to the closed-loop system.

**Theorem 3.1** *Consider the sub-system described by Eqs.(3.9b) and (3.9c). For this system,  $(\bar{e}, \tilde{\phi}) \equiv (0, 0)$  is an asymptotically stable equilibrium.*

**Proof:** From Eqs.(3.9b) and (3.9c) first notice that  $(\bar{e}, \tilde{\phi}) = (0, 0)$  implies  $(\dot{\bar{e}}, \dot{\tilde{\phi}}) = (0, 0)$ . Therefore,  $(\bar{e}, \tilde{\phi}) \equiv (0, 0)$  is an equilibrium point. To show that this equilibrium is asymptotically stable, we define the continuously differentiable, positive definite function

$$V(\bar{e}, \tilde{\phi}) = \frac{1}{2}m(1 - \Delta)\bar{e}^2 + \frac{1}{2}\tilde{\phi}^T\Gamma^{-1}\tilde{\phi}, \quad 0 < \Delta < 1 \quad (3.10)$$

The derivative of  $V$  can be computed as

$$\dot{V} = m(1 - \Delta)\bar{e}\dot{\bar{e}} + \tilde{\phi}^T\Gamma^{-1}\dot{\tilde{\phi}} \quad (3.11)$$

Using Eqs.(3.9b) and (3.9c), we obtain

$$\dot{V} = -c\bar{e}^2 \leq 0 \quad (3.12)$$

Since  $V$  is positive definite and  $\dot{V}$  is negative semi-definite, we conclude that  $(\bar{e}, \tilde{\phi}) \equiv (0, 0)$  is stable. In addition, since  $\dot{V}$  is uniformly continuous, we use Barbalat's lemma [13] to deduce  $\dot{V} \rightarrow 0$  as  $t \rightarrow \infty$ . This implies  $\bar{e} \rightarrow 0$  as  $t \rightarrow \infty$ . By differentiating Eq.(3.9b), we can show that  $\ddot{\bar{e}} = \ddot{\bar{e}}(t, \tilde{\phi}, \bar{e})$  is bounded. This implies that  $\dot{\bar{e}}$  is uniformly continuous. Since  $\bar{e} \rightarrow 0$  as  $t \rightarrow \infty$ , we once again use Barbalat's lemma [13] to deduce  $\dot{\bar{e}} \rightarrow 0$  as  $t \rightarrow \infty$ . Knowing  $\bar{e}, \dot{\bar{e}} \rightarrow 0$  as  $t \rightarrow \infty$ , we can conclude from Eq.(3.9b)

$$\mathbf{Y}_m^T \tilde{\phi} \rightarrow 0 \quad (3.13)$$

Furtherm

that

where  $\mathbf{I}$  is the

exciting (PE

This implies

we can now a

concludes our

**Lemma 3.1**

*an asymptotic*

**Proof:**

form

where  $z_1 \triangleq \bar{x}$

We know from

the sub-system

equilibrium p

(3.9c). Using

that  $(\bar{x}, \bar{e}, \bar{o}) \equiv$

**Theorem 3.2**

*closed loop sy*

**Proof:**

Furthermore, we can show that there exist positive constants  $\alpha_1$ ,  $\alpha_2$ , and  $T_o$ , such that

$$\alpha_2 \mathbf{I} \geq \int_t^{t+T_o} \mathbf{Y}_m \mathbf{Y}_m^T d\tau \geq \alpha_1 \mathbf{I} \quad (3.14)$$

where  $\mathbf{I}$  is the identity matrix,  $\mathbf{I} \in \mathfrak{R}^{(2n+1)(2n+1)}$ . Therefore  $\mathbf{Y}_m$  is a persistently exciting (PE) signal [13]. The proof of the PE condition is provided in Appendix B.1. This implies from Eq.(3.13) that  $\tilde{\phi} \rightarrow 0$ , as  $t \rightarrow \infty$ . Knowing  $\bar{e}, \tilde{\phi} \rightarrow 0$ , as  $t \rightarrow \infty$ , we can now assert that  $(\bar{e}, \tilde{\phi}) \equiv (0, 0)$  is an asymptotically stable equilibrium. This concludes our proof.

**Lemma 3.1** *The origin of the closed-loop system in Eq.(3.9),  $(\bar{x}, \bar{e}, \tilde{\phi}) \equiv (0, 0, 0)$ , is an asymptotically stable equilibrium point.*

**Proof:** The closed loop system in Eq.(3.9) is an interconnected system of the form

$$\dot{z}_1 = f_1(t, z_1, \mathbf{z}_2) \quad (3.15a)$$

$$\dot{\mathbf{z}}_2 = \mathbf{f}_2(t, \mathbf{z}_2) \quad (3.15b)$$

where  $z_1 \triangleq \bar{x}$ , and  $\mathbf{z}_2 \triangleq (\bar{e} \quad \tilde{\phi}^T)^T$  are the state variables of the two sub-systems. We know from Theorem 3.1 that  $\mathbf{z}_2 = 0$  is an asymptotically stable equilibrium of the sub-system in Eq.(3.15b). Also,  $\dot{z}_1 = f_2(t, z_1, 0)$  has an asymptotically stable equilibrium point at  $z_1 = 0$ . This can be readily established from Eqs.(3.15b) and (3.9c). Using the asymptotic stability theorem for cascaded systems [13], we conclude that  $(\bar{x}, \bar{e}, \tilde{\phi}) \equiv (0, 0, 0)$ , is an asymptotically stable equilibrium.

**Theorem 3.2** *The coordinate  $(x, \dot{x}, \tilde{\phi}) \equiv (0, 0, 0)$  is a stable equilibrium point for the closed loop system defined by Eqs.(2.3), (3.2), and (3.3).*

**Proof:** : Using Eqs.(2.19), (2.20), (3.2), (3.3), and (2.25), we can show that at

$(r, i, \tilde{o}) \equiv (0$

Also, at  $(r, i, \tilde{o})$

(3.2), and (3.3)

an equilibrium

now be deduced

1. The e

rium.

2. The t

when

bound

3. The

Theor

stabilizati

sensor run

$(x, \dot{x}, \tilde{\phi}) \equiv (0, 0, 0)$ , we have

$$\tilde{d} = \mathbf{Y}^T \tilde{\phi} = 0, \quad \bar{x} = x + \tilde{d} = 0,$$

$$\dot{\tilde{d}} = (\dot{\mathbf{Y}}^T \tilde{\phi} + \mathbf{Y}^T \dot{\tilde{\phi}}) = \mathbf{Y}^T \Gamma \mathbf{Y}_m \bar{e} = \Delta \bar{e} = \Delta(\dot{x} + \lambda \bar{x}) = \Delta \dot{x}$$

Also, at  $(x, \dot{x}, \tilde{\phi}) \equiv (0, 0, 0)$ ,  $\dot{\tilde{d}} = (\dot{x} - \lambda \bar{x}) = \dot{x} = 0$ , since  $0 < \Delta < 1$ . From Eqs.(2.3), (3.2), and (3.3), it follows that  $(\dot{x}, \ddot{x}, \dot{\tilde{\phi}}) = (0, 0, 0)$ . Therefore,  $(x, \dot{x}, \tilde{\phi}) \equiv (0, 0, 0)$  is an equilibrium point. The fact that  $(x, \dot{x}, \tilde{\phi}) \equiv (0, 0, 0)$  is asymptotically stable can now be deduced from:

1. The equilibrium point  $(\bar{x}, \bar{e}, \tilde{\phi}) \equiv (0, 0, 0)$  is an asymptotically stable equilibrium. This fact follows from Lemma 3.1,
2. The transformation matrix  $\mathbf{P}$  that maps  $(\bar{x}, \bar{e}, \tilde{\phi})$  to  $(x, \dot{x}, \tilde{\phi})$

$$\begin{pmatrix} x \\ \dot{x} \\ \tilde{\phi} \end{pmatrix} = \begin{pmatrix} & & \\ & \mathbf{P} & \\ & & \end{pmatrix} \begin{pmatrix} \bar{x} \\ \bar{e} \\ \tilde{\phi} \end{pmatrix} \quad (3.16)$$

$$\mathbf{P} \triangleq \begin{pmatrix} 1 & 0 & -\mathbf{Y}^T \\ -\lambda & (1 - \Delta) & -\dot{\mathbf{Y}}^T \\ 0 & 0 & \mathbf{E} \end{pmatrix} \quad (3.17)$$

where  $\mathbf{E} \in \mathfrak{R}^{(2n+1) \times (2n+1)}$  is the identity matrix, is well defined and upper bounded, and

3. The inverse transformation  $\mathbf{P}^{-1}$  exists, and  $\|\mathbf{P}^{-1}\|$  is also upper bounded.

Theorem 3.2 establishes that the adaptive controller proposed herein guarantees stabilization of the rotor geometric center through identification and cancellation of sensor runout disturbance.

### 3.4 Ro

In this section

tion in plant

tion of rotor

of exact kno

To this end,

modify our c

where

Substitutio

form

Using E

plified as f

Using the

### 3.4 Robustness to Parameter Uncertainties

In this section we establish that the ASRC scheme is robust to uncertainties or variation in plant parameters. Specifically, we shall show that ASRC guarantees stabilization of rotor geometric center and exact cancellation of sensor runout in the absence of exact knowledge of rotor mass,  $m$ ; magnetic stiffness,  $K_s$ ; and actuator gain,  $K_c$ . To this end, we estimate the values of these parameters to be  $\bar{m}$ ,  $\bar{K}_s$ , and  $\bar{K}_c$  and modify our control action and adaptation law in Eqs.(3.2) and (3.3), as follows:

$$I = -\frac{1}{\bar{K}_c} (\bar{K}_s \bar{x} + \bar{m} \lambda \dot{\bar{x}} + c \bar{e}) \quad (3.18)$$

$$\dot{\tilde{\phi}} = \Gamma \bar{Y}_m \bar{e} \quad (3.19)$$

where

$$\bar{Y}_m \triangleq \bar{K}_s \mathbf{Y} - \bar{m} \ddot{\mathbf{Y}} \quad (3.20)$$

Substitution of Eq.(3.18) in Eq.(3.1) indicates that the closed-loop system takes the form

$$m \ddot{\bar{x}} + \frac{K_c}{\bar{K}_c} (\bar{m} \lambda + c) \dot{\bar{x}} + \left[ \frac{K_c}{\bar{K}_c} (\bar{K}_s + c \lambda) - K_s \right] \bar{x} = m \ddot{\bar{d}} - K_s \tilde{d} \quad (3.21)$$

Using Eqs.(2.20), (2.23) and (3.19), the right hand side of Eq.(3.21) can be simplified as follows:

$$m \ddot{\bar{d}} - K_s \tilde{d} = m \left( \ddot{\mathbf{Y}}^T \tilde{\phi} + 2 \dot{\mathbf{Y}}^T \dot{\tilde{\phi}} + \mathbf{Y}^T \ddot{\tilde{\phi}} \right) - K_s \mathbf{Y}^T \tilde{\phi} \quad (3.22)$$

$$= -\mathbf{Y}_m^T \tilde{\phi} + m \left[ 2 \dot{\mathbf{Y}}^T \Gamma \bar{Y}_m \bar{e} + \mathbf{Y}^T \Gamma \left( \dot{\bar{Y}}_m \bar{e} + \bar{Y}_m \dot{\bar{e}} \right) \right] \quad (3.23)$$

Using the identities  $\dot{\mathbf{Y}}^T \Gamma \bar{Y}_m = 0$  and  $\mathbf{Y}^T \Gamma \dot{\bar{Y}}_m = 0$ , we get

$$m \ddot{\bar{d}} - K_s \tilde{d} = -\mathbf{Y}_m^T \tilde{\phi} + m \bar{\Delta} \dot{\bar{e}} \quad (3.24)$$

Substituting

where  $M, C$

The cl  
the adapta  
which is a f  
can be ma

Figure 3.2  
parameter

$$\bar{\Delta} \triangleq \mathbf{Y}^T \Gamma \bar{\mathbf{Y}}_m = \sum_{i=0}^n \gamma_i (\bar{K}_s + \bar{m} i^2 \omega^2) \quad (3.25)$$

Substituting Eq.(3.24) into Eq.(3.21), we get the closed-loop system dynamics

$$M \ddot{\bar{x}} + C \dot{\bar{x}} + K \bar{x} = -\mathbf{Y}_m^T \tilde{\phi} \quad (3.26)$$

where  $M$ ,  $C$  and  $K$  are defined as follows:

$$M \triangleq m(1 - \bar{\Delta}) \quad (3.27a)$$

$$C \triangleq \frac{K_c}{\bar{K}_c} (\bar{m} \lambda + c) - m \lambda \bar{\Delta} \quad (3.27b)$$

$$K \triangleq \left[ \frac{K_c}{\bar{K}_c} (\bar{K}_s + c \lambda) - K_s \right] \quad (3.27c)$$

The closed loop system, described by the dynamics of the rotor in Eq.(3.26) and the adaptation law in Eq.(3.19) is represented by the block diagram in Figure 3.2, which is a feedback inter-connection of two linear systems. The following observations can be made regarding these linear systems.

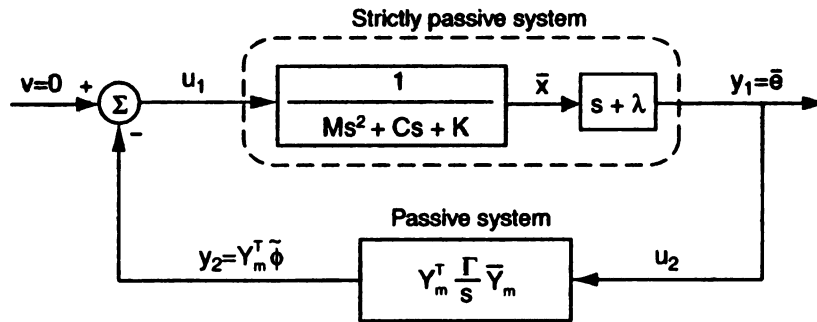


Figure 3.2. Block diagram of closed-loop system in the presence of uncertain plant parameters

Lemma 3.2

transfer func

is strictly po

**Proof:**

$G(j\omega)$

Therefore,

reference [

Lemma 3

**Proof**

Using th

for  $\epsilon = 0$

$$\int_0^{\epsilon} y$$

**Lemma 3.2** *The linear system in the forward path in Figure 3.2, defined by the transfer function*

$$G(s) = \frac{s + \lambda}{Ms^2 + Cs + K} \quad (3.28)$$

*is strictly passive if  $M, C, K > 0$ , and  $C - \lambda M > 0$ .*

**Proof:** If  $M, C, K > 0$ ,  $G(s)$  is Hurwitz. Furthermore, if  $C - \lambda M > 0$ , we have

$$G(j\omega) + G(-j\omega) > 0, \quad G(\infty) = 0, \quad \lim_{\omega \rightarrow \infty} \omega^2 [G(j\omega) + G(-j\omega)] > 0$$

Therefore,  $G(s)$  is strictly positive real (SPR) according to lemma D.4 obtained from reference [13, 18]; thus,  $G(s)$  is strictly passive.

**Lemma 3.3** *The linear system in the feedback path of Figure 3.2 is passive.*

**Proof:** The adaptation law in Eq.(3.19) can be written as

$$\dot{\tilde{a}}_0 = \gamma_0 \bar{K}_s \bar{e} \quad (3.29a)$$

$$\dot{\tilde{a}}_i = \gamma_i [\bar{K}_s + \bar{m}i^2\omega^2] \sin(i\omega t) \bar{e} \quad (3.29b)$$

$$\dot{\tilde{b}}_i = \gamma_i [\bar{K}_s + \bar{m}i^2\omega^2] \cos(i\omega t) \bar{e}, \quad i = 1, 2, \dots, n \quad (3.29c)$$

Using these relations, and defining

$$\rho_i = \frac{K_s + mi^2\omega^2}{\gamma_i(\bar{K}_s + \bar{m}i^2\omega^2)} \quad (3.30)$$

for  $i = 0, 1, 2, \dots, n$ , we can express the net energy flow into the system as

$$\begin{aligned} \int_0^t y_2 u_2 dt &= \int_0^t \mathbf{Y}_m^T \tilde{\phi} \bar{e} dt \\ &= K_s \int_0^t \tilde{a}_0 \bar{e} dt + \sum_{i=1}^n (K_s + mi^2\omega^2) \int_0^t [\tilde{a}_i \sin(i\omega t) \bar{e} + \tilde{b}_i \cos(i\omega t) \bar{e}] dt \\ &= \rho_0 \int_0^t \tilde{a}_0 \dot{\tilde{a}}_0 dt + \sum_{i=1}^n \rho_i \int_0^t [\tilde{a}_i \dot{\tilde{a}}_i + \tilde{b}_i \dot{\tilde{b}}_i] dt \end{aligned}$$

where  $W_i^0$

$W_i^0$

From Eq. (3.1)

We now

**Theorem 3.1**

in Eqs. (3.1)

(0,0,0) of

rotor mass

adaptation

**Proof**

( $i = 0$ )

Lemmas 3.1

interconn

theorem

stable, a

Now,

need to

Eqs. (2.3)

from:

1. Th

2. Th

$$\begin{aligned}
&= \frac{\rho_0}{2} [\tilde{a}_0^2(t) - \tilde{a}_0^2(0)] + \sum_{i=1}^n \frac{\rho_i}{2} [\tilde{a}_i^2(t) + \tilde{b}_i^2(t) - \tilde{a}_i^2(0) - \tilde{b}_i^2(0)] \\
&= W[\tilde{\phi}(t)] - W[\tilde{\phi}(0)]
\end{aligned} \tag{3.31}$$

where  $W[\tilde{\phi}(t)]$  is a positive definite energy storage function given by the relation

$$W[\tilde{\phi}(t)] \triangleq \frac{1}{2} \tilde{\phi}^T \mathbf{M} \tilde{\phi}, \quad \mathbf{M} \triangleq \text{diag} (\rho_0, \rho_1, \rho_1, \rho_2, \rho_2, \dots, \dots, \rho_n, \rho_n)$$

From Eq.(3.31) we claim passivity [13, 18].

We now present our final result with the help of the following theorem.

**Theorem 3.3** *Asymptotic stability and robustness* *The control and adaptation laws in Eqs.(3.18) and (3.19) guarantee asymptotic stability of the equilibrium  $(x, \dot{x}, \tilde{\phi}) \equiv (0, 0, 0)$  of the magnetic bearing system in Eq.(2.3) in the presence of uncertainty in rotor mass,  $m$ ; magnetic stiffness,  $K_s$ ; and actuator gain,  $K_c$ , provided the error and adaptation gains are chosen to satisfy  $M, C, K > 0$ , and  $C - \lambda M > 0$ .*

**Proof:** Through proper choice of the error gains  $(c, \lambda)$ , and adaptation gains  $(\gamma_i, i = 0, 1, 2, \dots, n)$ , we can easily guarantee  $M, C, K > 0$  and  $C - \lambda M > 0$ . Using Lemmas 3.2 and 3.3, we can then conclude that the closed-loop system is a feedback interconnection of a strictly passive system and a passive system. Using the passivity theorem from the appendix of [18], we claim  $(\bar{x}, \dot{\bar{x}}, \tilde{\phi}) \equiv (0, 0, 0)$  is globally uniformly stable, and  $\bar{x}, \dot{\bar{x}} \rightarrow 0$  as  $t \rightarrow \infty$ .

Now, to show  $(x, \dot{x}, \tilde{\phi}) \equiv (0, 0, 0)$  is an asymptotically stable equilibrium, we first need to show that  $(x, \dot{x}, \tilde{\phi}) \equiv (0, 0, 0)$  is an equilibrium. This can be verified using Eqs.(2.3), (2.20), (3.18), and (3.19). The fact that  $(x, \dot{x}, \tilde{\phi}) \equiv (0, 0, 0)$  is stable follows from:

1. The equilibrium point  $(\bar{x}, \dot{\bar{x}}, \tilde{\phi}) \equiv (0, 0, 0)$  is globally uniformly stable.
2. The transformation matrix  $\mathbf{P}(t)$  that maps  $(\bar{x}, \dot{\bar{x}}, \tilde{\phi})$  to  $(x, \dot{x}, \tilde{\phi})$  is well defined

and

3. The in

Finally, we

Figure 3.2 w

in Figure 3.3

exciting, as

$Y^T \tilde{\phi} = 0$ . A

by simply sh

### 3.5 Co

The method

qualitative b

tem obtaine

method for

small para

periodic or

of the time

The ob

imated para

averaging a

ence of unc

the conver

to obtain t

known.

The er

and  $\| \mathbf{P} \|$  is upper bounded.

3. The inverse transformation  $\mathbf{P}^{-1}$  exists, and  $\| \mathbf{P}^{-1} \|$  is also upper bounded.

Finally, we prove  $(x, \dot{x}, \tilde{\phi}) \rightarrow (0, 0, 0)$  as  $t \rightarrow \infty$ . Since  $\bar{x}, \dot{\bar{x}} \rightarrow 0$ ,  $\bar{e} \rightarrow 0$ . Also, from Figure 3.2 we claim  $u_1 = y_2 \rightarrow 0$ . This is true since the mass-spring-damper system in Figure 3.2 cannot have zero output for nonzero input. Since  $\mathbf{Y}_m^T$  is persistently exciting, as discussed in the proof of Theorem 3.1,  $y_2 = 0$  implies  $\tilde{\phi} = 0$ , and  $\tilde{d} = \mathbf{Y}^T \tilde{\phi} = 0$ . Also,  $\dot{\tilde{d}} = (\dot{\mathbf{Y}}^T \tilde{\phi} + \mathbf{Y}^T \dot{\tilde{\phi}}) = \mathbf{Y}^T \dot{\tilde{\phi}} = \mathbf{Y}^T \Gamma \mathbf{Y}_m \bar{e} = 0$ . We conclude the proof by simply showing  $x \triangleq (\bar{x} - \tilde{d}) \rightarrow 0$  and  $\dot{x} \triangleq (\dot{\bar{x}} - \dot{\tilde{d}}) \rightarrow 0$ .

### 3.5 Convergence Rate Analysis Using Averaging

The method of averaging is an asymptotic method, which permits the analysis of qualitative behavior of time-varying systems through a time-invariant (averaged) system obtained by time-averaging of the system. This method has become the general method for the analysis of nonlinear ordinary differential equations (ODEs) with a small parameter [38], including the determination of the existence and stability of periodic or almost periodic solutions as well as the analysis of the transient behavior of the time-varying system.

The objective of this section is to approximate the convergence rate of the estimated parameters as represented by time constants. We first apply the two-time scale averaging analysis given in reference [32] to the proposed adaptive system in the presence of uncertainties in the plant parameters. We determine the variables that affect the convergence rate of the estimated parameters. These results are finally reduced to obtain the time constants of estimated parameters when the plant parameters are known.

The error signal in Figure 3.2 can be seen as the result of signal  $(-\mathbf{Y}_m^T \tilde{\phi})$  being

passed thro

where  $G(s)$

Eq.(3.32) to

To appl

adaptation

is sufficient

and convex

assumption

scale of th

approxima

where  $T =$

a symmetr

where  $R, C$

passed through an SPR transfer function  $G(s)$ .

$$\bar{e} = -G[\mathbf{Y}_m^T \tilde{\phi}] \triangleq -\bar{G}(\mathbf{Y}_m^T) \cdot [\tilde{\phi}] \quad (3.32)$$

where  $G(s)$  is defined by Eq.(3.28). Note that  $\bar{G}(\mathbf{Y}_m^T)$  is a signal vector. Substituting Eq.(3.32) to the adaptation law in Eq.(3.19) we obtain

$$\dot{\tilde{\phi}} = -\Gamma \bar{\mathbf{Y}}_m [\bar{G}(\mathbf{Y}_m^T) \tilde{\phi}] \quad (3.33)$$

To apply the averaging method, we need to treat the above equation as a slow adaptation process. For this purpose we must assume that the adaptation gain  $\Gamma$  is sufficiently small and the true values of parameter  $\phi$  belongs to a given compact and convex set for which the frozen ( $\Gamma = 0$ ) closed-loop system is stable. Using this assumption, we can separate the slow time scale of adaptation from the fast time scale of the other signals. By applying the averaging method given in [32], we can approximate the original system in Eq.(3.33) by using an averaged system such as

$$\begin{aligned} \dot{\tilde{\phi}}_{av} &= -\Gamma \left[ \frac{1}{T} \int_{t_0}^{t_0+T} \bar{\mathbf{Y}}_m \bar{G}(\mathbf{Y}_m^T) \tilde{\phi} dt \right] \\ &= -\Gamma \mathbf{R}(0) \tilde{\phi}_{av} \end{aligned} \quad (3.34)$$

where  $T = \frac{2\pi}{\omega}$ ,  $\tilde{\phi}_{av}$  is the averaged estimated error vector,  $\tilde{\phi}_{av} \in \Re^{(2n+1)}$ , and  $\mathbf{R}(0)$  is a symmetric positive-definite cross correlation matrix provided that  $\bar{\Delta} < 1$  and  $c > 0$ .

$$\mathbf{R}(0) = \text{diag}(R_0, R_1, R_1, R_2, R_2, \dots, R_n, R_n) \quad (3.35)$$

where  $\mathbf{R}(0) \in \Re^{(2n+1)(2n+1)}$ , and its components are

$$R_0 = K_s \bar{K}_s G(j\omega = 0), \quad (3.36)$$

for  $i = 1, 2, \dots$

the derivative

here, however

of each component

by a set of

averaging the

transition matrix

stable with

particular

exponential

ultimately

Known

$\tau_0 =$

$\tau_1 =$

No

So

we can

ing

$$R_i = \frac{[K_s + m(i\omega)^2] [\bar{K}_s + \bar{m}(i\omega)^2]}{2} \mathbf{Re}\{G(j(i\omega))\} \quad (3.37)$$

for  $i = 1, 2, \dots, n$ . It can be observed that  $R_0, R_i > 0$  if  $G(s)$  is SPR. The details of the derivation of the correlation matrix is given in Appendix C. It should be noted here, however, that both  $\mathbf{R}(0)$  and  $\mathbf{\Gamma}$  are square diagonal matrices; thus, the dynamics of each component in  $\tilde{\phi}_{av}$  is decoupled, exponentially stable, and can be represented by a set of simple first-order dynamics with time constants shown in Table 3.1. The averaging theorem in Sastry and Bodson [32] proved that, as long as the cross correlation matrix  $\mathbf{R}(0)$  exists and  $\mathbf{\Gamma}$  is sufficiently small, the original system is exponentially stable within a finite ball  $\mathbf{B}_h$  if the averaged system is exponentially stable. In this particular case the equilibrium point  $\tilde{\phi} = 0$  for the system in Eq.(3.33) is locally, exponentially stable. Therefore, we can conclude that the estimated parameters  $\hat{\phi}$  ultimately converge to the true values  $\phi$  exponentially fast.

Table 3.1. Time constants of the averaged system

Known plant parameters	Uncertain plant parameters
$\tau_0 = \frac{c}{\gamma_0 K_s^2}$	$\tau_0 = \frac{K}{\gamma_0 [\bar{K}_s K_s \lambda]}$
$\tau_i = \frac{2[m(1 - \Delta)(i\omega) + c]}{\gamma_i [K_s + m(i\omega)^2]^2}$	$\tau_i = \frac{2[M(i\omega)^2 + C(i\omega) + K]}{\gamma_i [\bar{K}_s + \bar{m}(i\omega)^2] [K_s + m(i\omega)^2] [(i\omega) + \lambda]}$

Note:  $i = 1, 2, \dots, n$

Several observations can be made regarding the results shown in Table 3.1. First, we can easily derive the time constants for the known plant parameters case by removing the bar signs and knowing that instead of going through the filter in Eq.(3.28),

the signal (

as it can be

$R_0, R_1 > 0$

time consta

in both cas

angular spe

numerical

## 3.6 S

### 3.6.1

Simulation

ness of th

model of

real situa

determin

paramete

performe

we can

nonline

by usin

A.9. N

the sta

Th

the signal  $(-\mathbf{Y}_m^T \tilde{\phi})$  passes through

$$G(s) = \frac{1}{m(1 - \Delta)s + c} \quad (3.38)$$

as it can be obtained from Eq.(3.8). The above transfer function is also SPR. Thus,  $R_0, R_i > 0$ . It can also be concluded that if the plant parameters are known, the time constants are independent of the gain  $\lambda$ . Furthermore, we can observe that in both cases the time constant of the DC component is not affected by the rotor angular speed  $\omega$ , while the time constants of higher harmonics are subject to  $\omega$ . The numerical results of the time constants are presented in the next section.

## 3.6 Simulation Results

### 3.6.1 Known Plant Parameters Case

Simulations are performed using Matlab/Simulink<sup>TM</sup> to demonstrate the effectiveness of the ASRC algorithm. Though the controller was designed using a linearized model of the plant, we use the nonlinear plant model in Eq.(2.1) to simulate the real situation. The bearing parameters were assumed to be known. These values, determined in our experimental hardware, can be referenced from Table A.3. Other parameters used in simulations are shown in Table 3.2. The SRO compensation was performed up to the third harmonics. For the magnitude of SRO given in Table 3.2, we can assume that the effect of SRO to the system will not introduce significant nonlinear dynamics at steady state, even without adaptation. This can be evaluated by using the resulting magnetic force as function of  $I$  and  $x$  shown in Figures A.7 to A.9. Note that using Eq.(2.25),  $\Delta$  is found to be 0.235, which is relatively far from the stability limit of 1.

The simulation results are shown in Figures 3.3 through 3.5. These figures indicate

that estim.

geometric d

adaptation

Using

estimated

The dynam

in Figure

third har

quite well

The ef

eters can

that we c

that estimation of runout is successfully completed within 0.3 second, and the rotor geometric center is effectively stabilized to the origin. The transient-currents during adaptation are within a reasonable range as seen in Figure 3.5.

Table 3.2. Parameters for ASRC simulation

Angular speed: $\omega = 2\pi \times 20$ rad/s
Sensor runout: $a_0 = 10 \mu\text{m}$ $a_1 = 67.615 \mu\text{m}; b_1 = 18.117 \mu\text{m};$ $a_2 = 7.071 \mu\text{m}; b_2 = 7.071 \mu\text{m};$ $a_i = b_i = 0$ for $i \geq 3$
Error gains: $\lambda = 400 \text{ s}^{-1}; c = 1200 \text{ kg/s}$
Adaptation gain matrix: $\Gamma = \text{diag}(1, 2, 2, 1, 1, 0.5, 0.5) \times 10^{-7} \text{ m/N}$
Plant initial conditions: $x(t = 0) = -0.1 \times 10^{-3} \text{ m}; \dot{x}(t = 0) = 0$
Initial conditions of estimated parameters: $\hat{a}_i(t = 0) = 0; \hat{b}_i(t = 0) = 0$ for $i = 0, 1, 2,$ and $3$

Using the averaging method explained in section 3.5, the time constants of the estimated parameters are  $\tau_0 = 0.064 \text{ s}$ ,  $\tau_1 = 0.065 \text{ s}$ ,  $\tau_2 = 0.097 \text{ s}$ , and  $\tau_3 = 0.13 \text{ s}$ . The dynamics of the averaged system are compared to the original dynamics as shown in Figure 3.6. In this figure without loss of generality, we omit to show results in the third harmonic components. It can be concluded that the averaged dynamics are quite well matched with the dynamics of the original systems.

The effect of changing angular speed to the convergence rate of estimated parameters can be explained using the results shown in Figure 3.7. The results suggest that we can choose adaptation gains such that all estimated parameters converge at

the same rate

the convergence

convergence

### 3.6.2 U

To demonstr

ulation resul

estimation o

actuator gai

in Table A.

gular veloci

be verified

otic stabil

3.8 through

the sensor

addition, t

Table 3.3.

100% in t

Vari
------

IC
----

the same rate for a given operating rotor speed  $\omega$ . We can also notice that at low  $\omega$  the convergence rates are relatively sensitive to the change of  $\omega$ . It is clear that the convergence rate of the higher harmonics are more sensitive to the change of  $\omega$ .

### 3.6.2 Uncertain Plant Parameters Case

To demonstrate robustness of the ASRC to parameter uncertainties, we present simulation results using the nonlinear model of our magnetic bearing; assuming over-estimation of the uncertain parameters, namely, rotor mass, magnetic stiffness, and actuator gain by 100%. The nominal parameter values were assumed to be the ones in Table A.3. The Fourier coefficients of sensor runout, rotor initial conditions, angular velocity, error gains, and adaptation gains were chosen as in Table 3.2. It can be verified from the calculation results in Table 3.3 that the conditions for asymptotic stability in theorem 3.3 are always satisfied. The simulation results in Figures 3.8 through 3.10 show that the ASRC remains stable and able to correctly identify the sensor runout despite of the quite large over-estimation in plant parameters. In addition, the coil currents are still within a reasonable range as seen in Figure 3.10.

Table 3.3. Numerical values of variables assuming  $m, c, K_s, K_c$  are over-estimated by 100% in the actual case

Variable	Nominal value	Actual value due to 100 % over-estimation of parameters	Unit
$\bar{\Delta}$	0.24	0.47	—
M	1.86	1.29	(kg)
C	$1.94 \times 10^3$	$1.12 \times 10^3$	(kg/s)
K	$4.8 \times 10^5$	$2.4 \times 10^5$	(N/m)
$(C - \lambda M)$	$1.2 \times 10^3$	$0.6 \times 10^3$	(kg/s)

1

$\hat{\alpha}_0$  ( $\mu\text{m}$ )

$\hat{\alpha}_1$  ( $\mu\text{m}$ )

$\hat{\alpha}_2$  ( $\mu\text{m}$ )

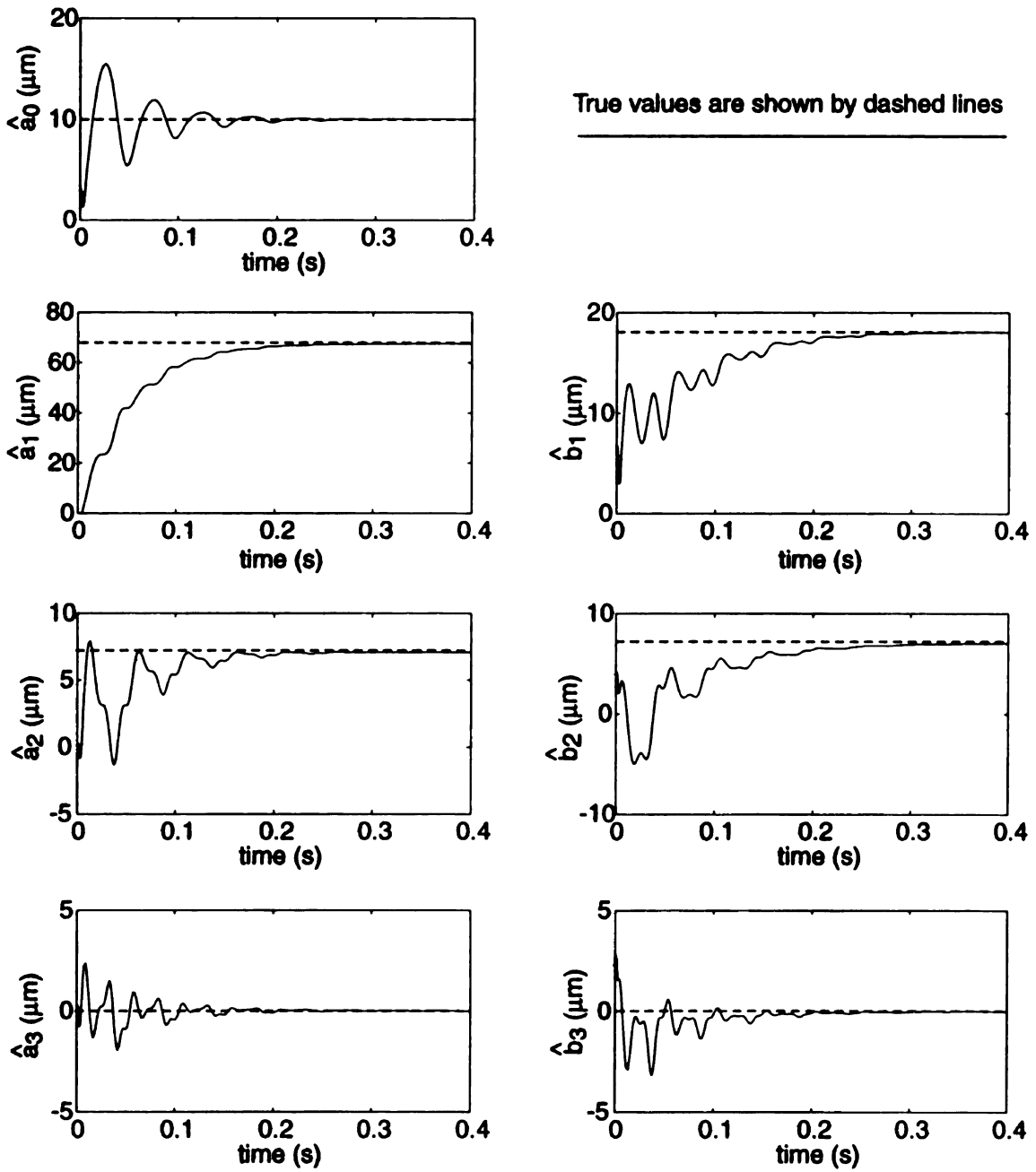


Figure 3.3. Estimated parameters of sensor runout

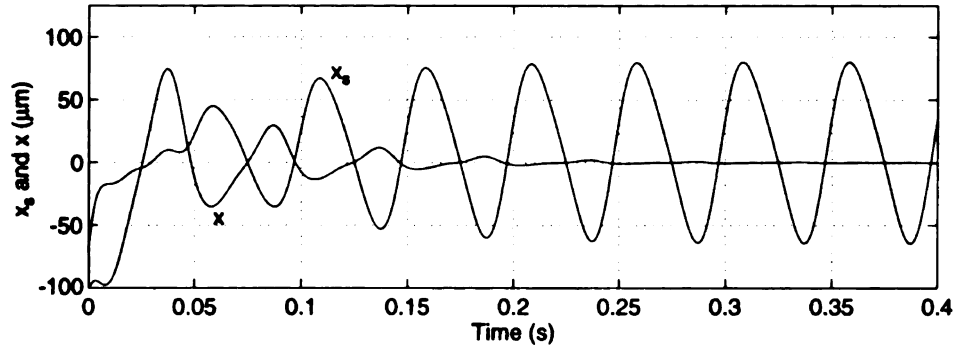


Figure 3.4. Stabilization of rotor geometric center using ASRC

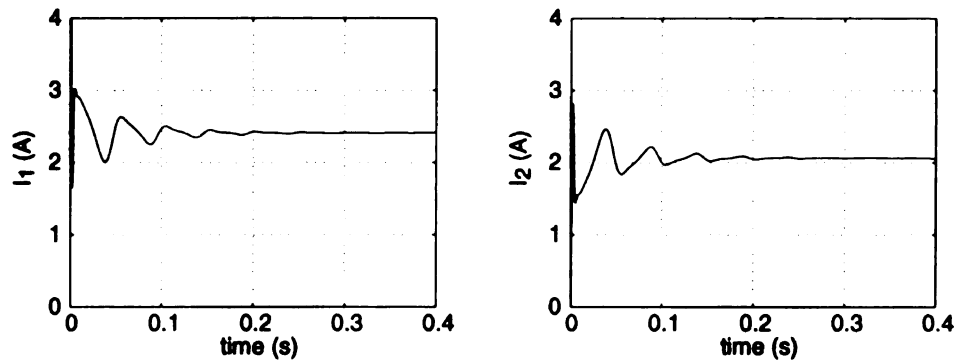


Figure 3.5. Transients of currents of ASRC

$\mu$  (m)

$\mu$  (m)

$\mu$  (m)

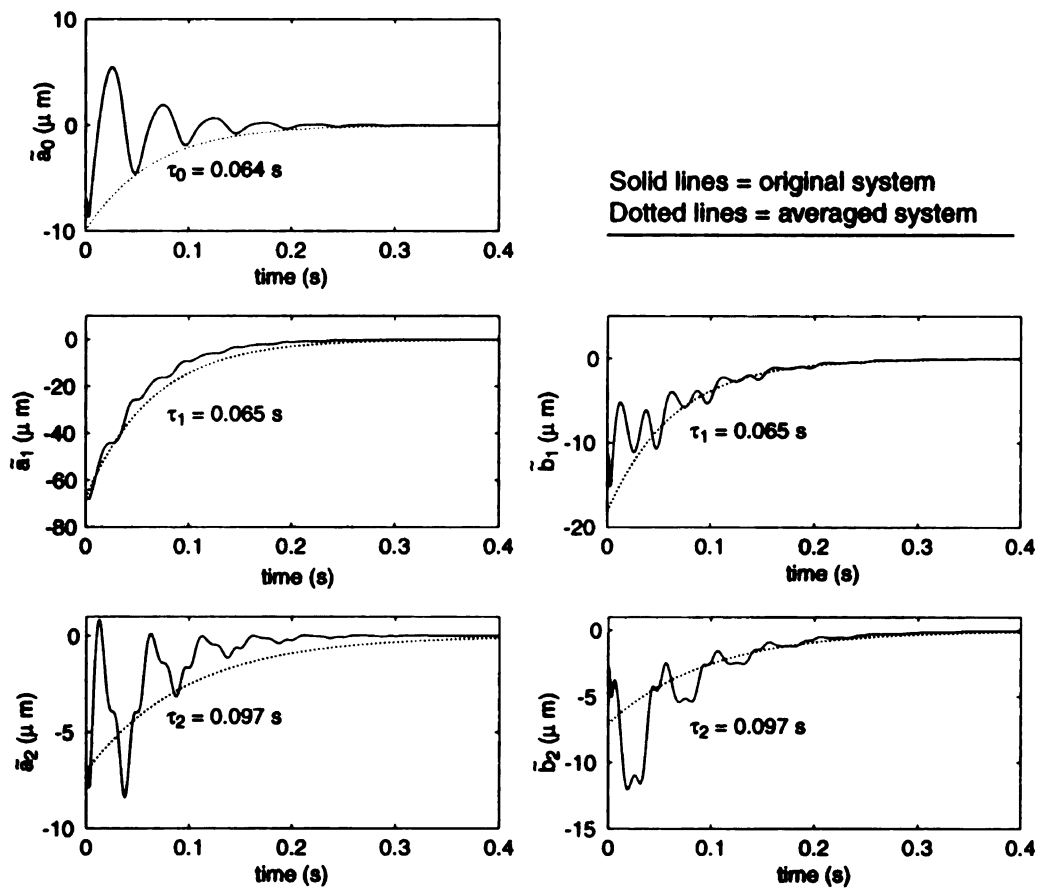


Figure 3.6. Averaged approximation of ASRC

A comp  
that the cl  
gence rate  
results usi  
transient  
to about 3  
shown in

### 3.7 E

To experi  
adaptatio  
environme

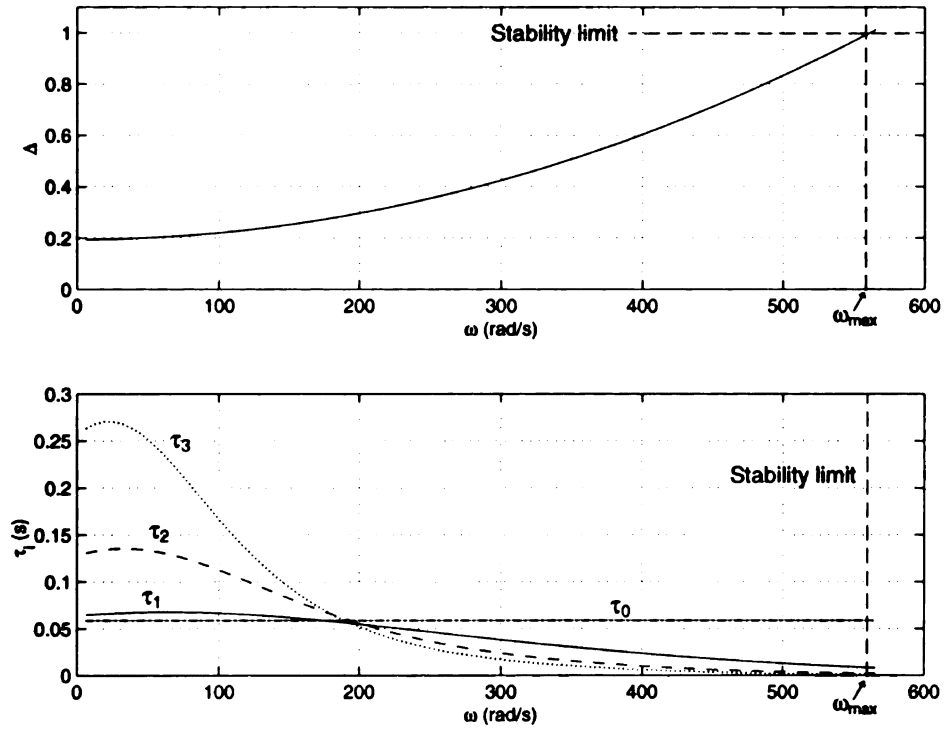


Figure 3.7. Time constants of estimated parameters in ASRC

A comparison of Figures 3.3 through 3.5 and Figures 3.8 through 3.10 indicates that the closed-loop system with 100% over-estimated parameters has a faster convergence rate than the closed-loop system with known parameters. The approximation results using the averaging analysis as shown in Figure 3.11 also confirm this faster transient performance. However, the stability limit  $\omega_{max}$  of the ASRC has reduced to about 350 rad/s as seen in Figure 3.12. Previously,  $\omega_{max}$  was about 560 rad/s as shown in Figure 3.7.

### 3.7 Experimental Procedure

To experimentally verify the effectiveness of the ASRC, the control action and the adaptation law in Eqs.(3.18) and (3.19) were implemented in the Matlab/Simulink<sup>TM</sup> environment and downloaded to a Digital Signal Processor (DSP) board manufactured

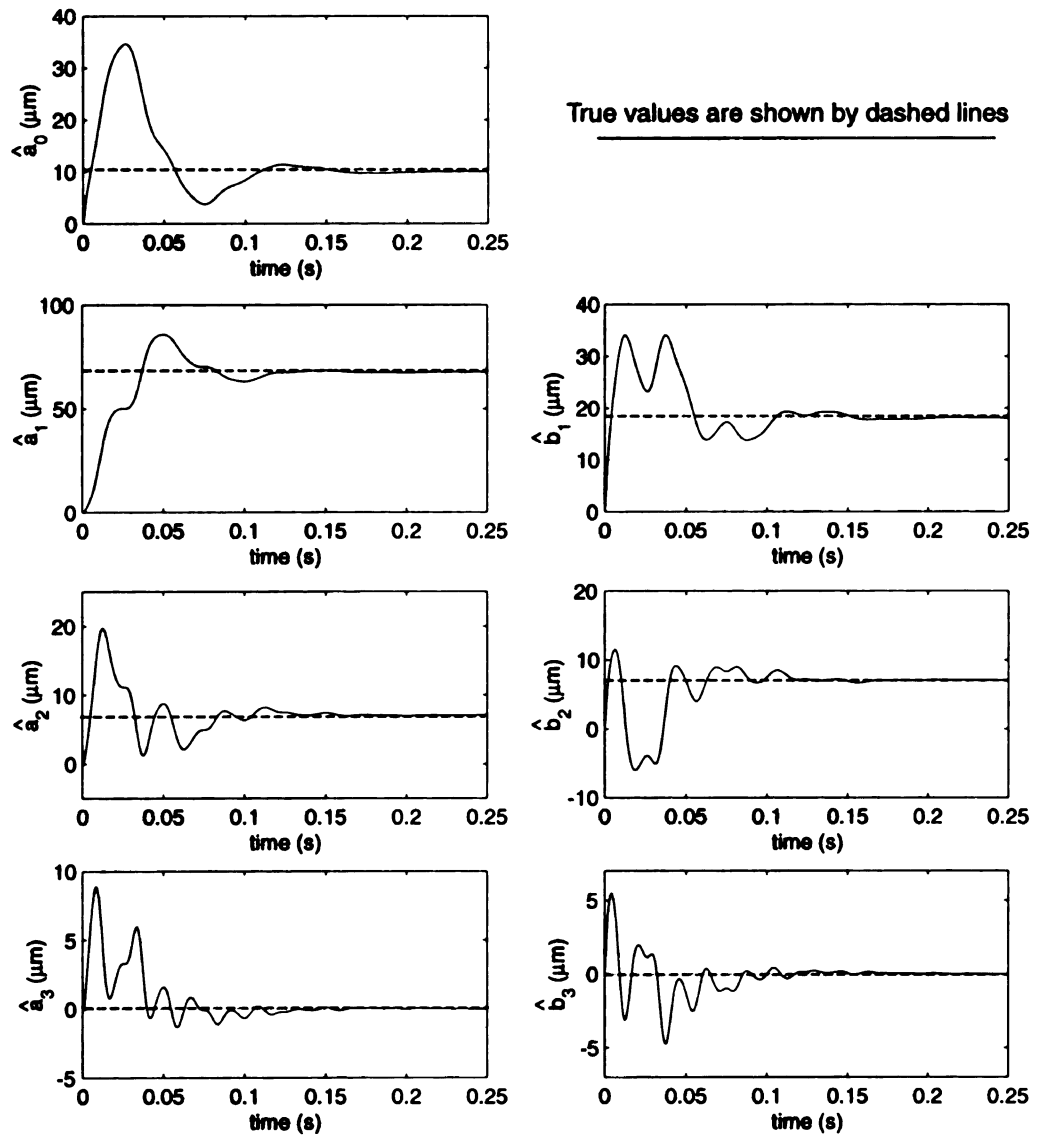


Figure 3.8. Sensor runout estimation in uncertain plant

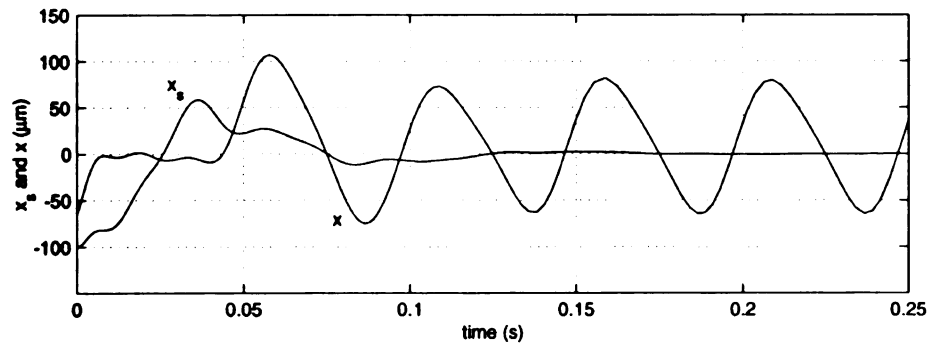


Figure 3.9. Stabilization of rotor geometric center using ASRC in uncertain plant

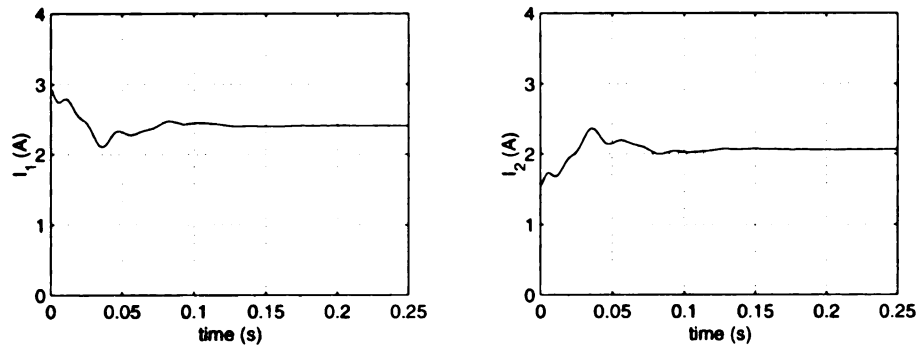


Figure 3.10. Transients of currents of ASRC in uncertain plant

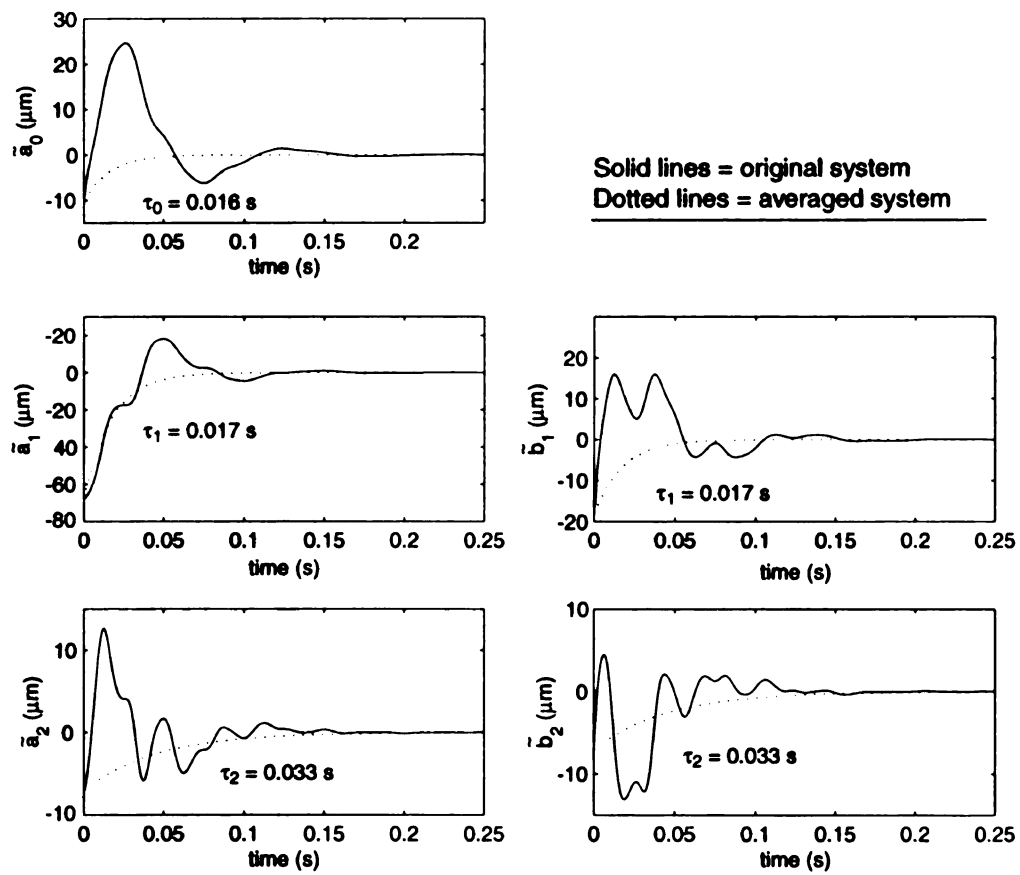


Figure 3.11. Averaged approximation of ASRC in uncertain plant

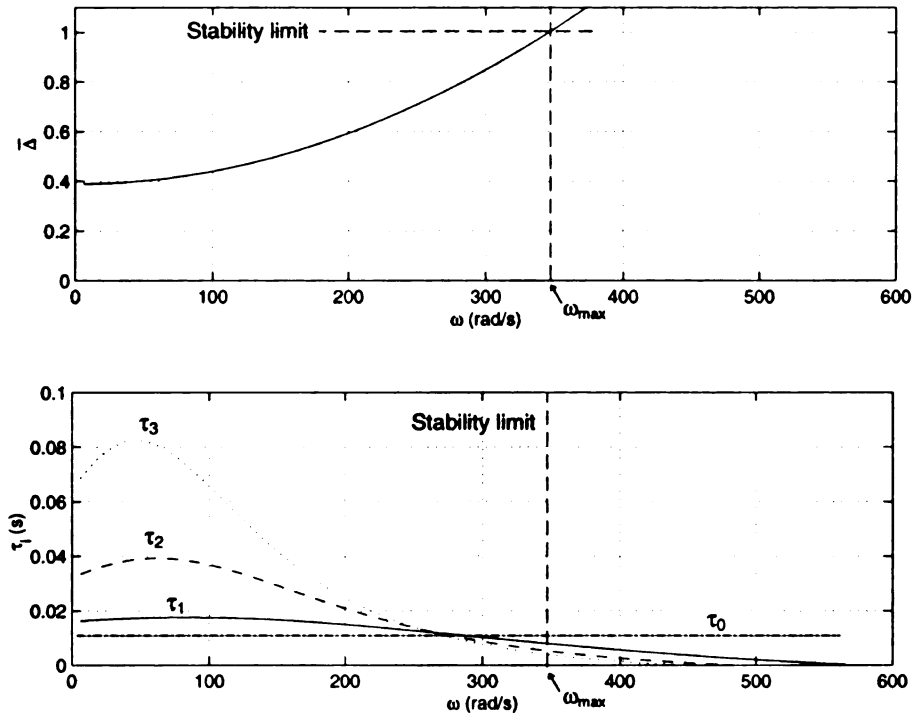


Figure 3.12. Time constants of estimated parameters in uncertain plant

by DSpace. The DSP board, sampling approximately at 13 KHz, was used to control the rotor along both bearing axes, independently. The specifications of the DSP are presented in Appendix A.4. The sensor runout estimation was performed up to the second harmonics. Under this computation load, the DSP allowed us to store ten signals in real time. For the  $x$  axis we stored the estimated position,  $\bar{x}$ ; current,  $I_x$ ; and the DC component and estimated Fourier coefficients of the first harmonic:  $\bar{a}_{0x}$ ,  $\bar{a}_{1x}$ ,  $\bar{b}_{1x}$ . The estimated coefficients of the second harmonic were found to be negligible but could not be stored due to DSP limitations. The sensor signal,  $x_s$ , was regenerated from stored data  $\bar{x}$ ,  $\bar{a}_{0x}$ ,  $\bar{a}_{1x}$ , and  $\bar{b}_{1x}$ , using Eq.(2.16). Since the second harmonic coefficients were used in the computation of  $\bar{x}$ , regeneration of  $x_s$  from  $\bar{x}$  in the absence of these coefficients may lack some accuracy at relatively very low order. Our choice of acquiring signals for the  $y$  axis was exactly the same as that for the  $x$  axis.

The schematic of the bearing-rotor rig used for the experiment is shown in Figures A.1. and A.2. The rotor is arranged such that there are node points between a sensor-actuator pair for the mode shape closest to the controller bandwidth. In this case, we avoid the non-collocation effect of sensor and actuator in the lowest flexible mode as suggested by Figure A.4 and Table 7.2. The calculation of the modes shape was performed using the finite element analysis software from ROMAC, program MODAL with the input shown in Appendix A.1. The critical speed map of the rotor, obtained using program CRTSP\_2 of ROMAC, is shown in Figure A.5

The electromagnets were driven by switching power amplifiers, a product of Advanced Motion Control, operating with 1.6 KHz bandwidth. The Bode plot of the power amplifiers is shown in Figure A.10. To ensure negligible effects due to unbalance, the rotor was well balanced and spun at the relatively low rpm of 1200. This speed is 20 times less than the first critical speed of the rotor, and guarantees negligible effects due to flexibility, which was not considered in our model. We used analog PD controllers shown in Appendix A.3 to stabilize the rotor in bearing B. Thus, only bearing A is the interest of our study, controlled by the DSP. The error and adaptations gains of the adaptive controller were chosen as  $\lambda = 400 \text{ s}^{-1}$ ,  $c = 1200 \text{ kg/s}$ , and  $\Gamma = \text{diag}(1.0, 1.7, 1.7, 1.5, 1.5) \times 10^{-7} \text{ m/N}$ .

In controller implementation, the derivative of the estimated position signal,  $\dot{\hat{x}}$ , was numerically computed by passing the signal  $\hat{x}$  through the transfer function  $2500s/(s + 2500)$ . This eliminates potential problems arising from infiltration of wide-band noise into the sensor signal.

### 3.8 Experimental Results

We **f**irst present experimental results based on our best knowledge of the values of the **p**lant parameters  $m$ ,  $K_s$ , and  $K_c$  as provided in Table A.3. Therefore, in this case

v  
E  
t  
i  
E  
s  
E  
v  
c  
r  
u  
e  
t  
c  
E  
  
E  
s

we can assume that the control action and adaptation law are in accordance with Eqs.(3.2) and (3.3).

The trajectory of the rotor's estimated geometric center  $(\bar{x}, \bar{y})$  and regenerated trajectory of the geometric center provided by the position sensors  $(x_s, y_s)$  are shown in Figure 3.13. These trajectories indicate that while the sensors continue to provide geometric center positions corrupt with runout disturbance, their estimated values are stabilized to the origin with ASRC. It is seen from Figure 3.14 that the estimation of Fourier coefficients of runout is completed in 0.3 seconds. In the same time, sinusoidal variation in the control currents vanish in Figure 3.15. These zero steady-state control currents imply stabilization of rotor geometric center to the origin in the absence of mass unbalance. Indeed, we can verify from Eq.(3.1) that the rotor would become unstable if this was not the case. We ensured negligible mass unbalance effects in our experiments through rotor balancing and by spinning the rotor at low rpm. Knowing that the rotor geometric center has stabilized to the origin, runout disturbance was obtained from the Fourier coefficients in Figure 3.14. The trajectories of  $x_s, y_s$  in Figure 3.13 also provide this information.

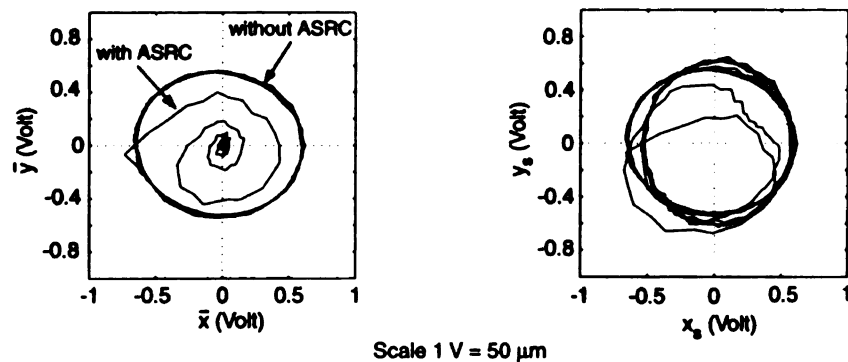


**Figure 3.13.** Trajectory of estimated rotor geometric center and regenerated sensor signals

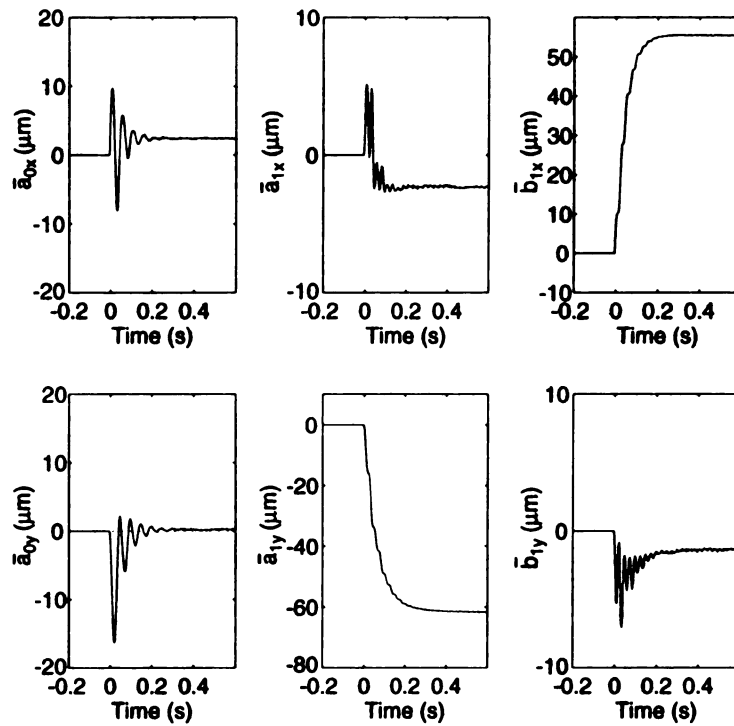


Figure 3.14. Trajectory of estimated Fourier coefficients of sensor runout

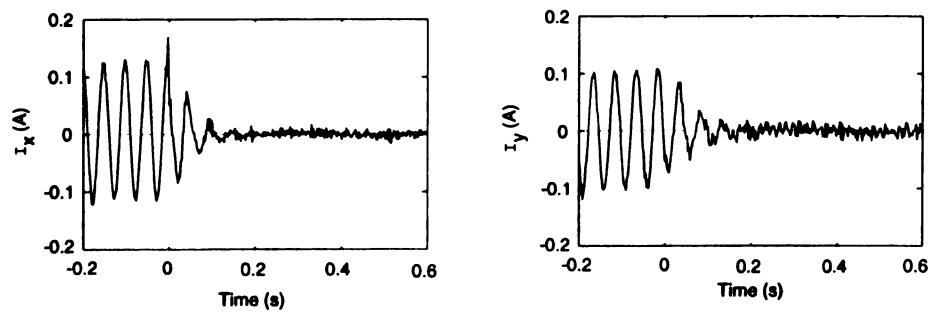


Figure 3.15. Trajectory of control currents

To demonstrate the robustness of ASRC to parameter uncertainty, we used control and adaptation laws in Eqs.(3.18) and (3.19). The parameter values  $\bar{m}$ ,  $\bar{K}_s$ , and  $\bar{K}_c$  in the control law were chosen to be 25% larger than the values of  $m$ ,  $K_s$ , and  $K_c$  provided in Table A.3. The results obtained from our experiments are shown in Figures 3.16 to 3.18. These results indicate that runout is eliminated and the rotor geometric center is successfully stabilized to the origin despite error in the model used to construct the controller.

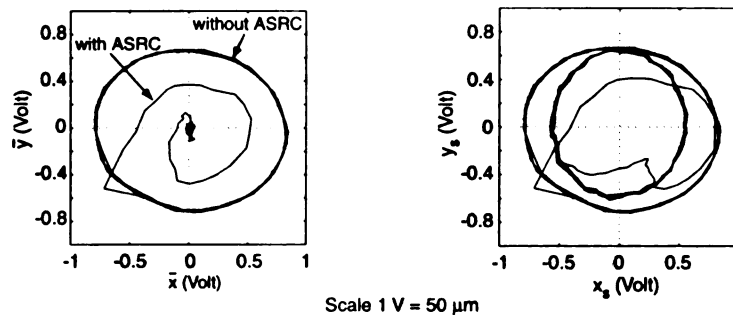


Figure 3.16. Trajectory of estimated rotor geometric center and regenerated sensor signals

### 3.9 Summary and Remarks

This chapter presents a simple, yet robust, algorithm for adaptive compensation of sensor runout in active magnetic bearings. The algorithm is based on a rigid rotor model with no mass unbalance and assumes the angular speed of the rotor to be known and constant. Using powerful tools such as Lyapunov stability, persistence of excitation, and passivity, the algorithm is shown to guarantee perfect cancellation of runout harmonics and stabilization of the rotor geometric center. Through modeling, estimation, and cancellation of the DC component of runout, the algorithm generates

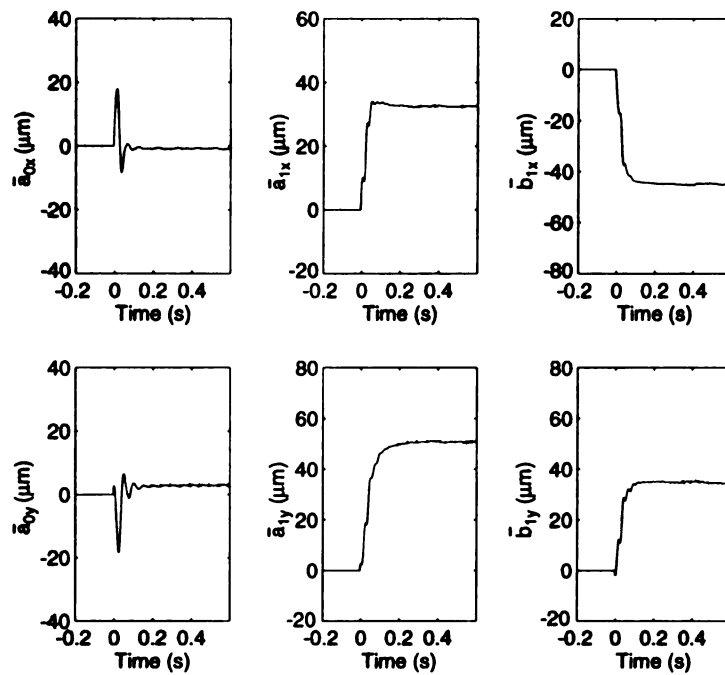


Figure 3.17. Trajectory of estimated Fourier coefficients of sensor runout

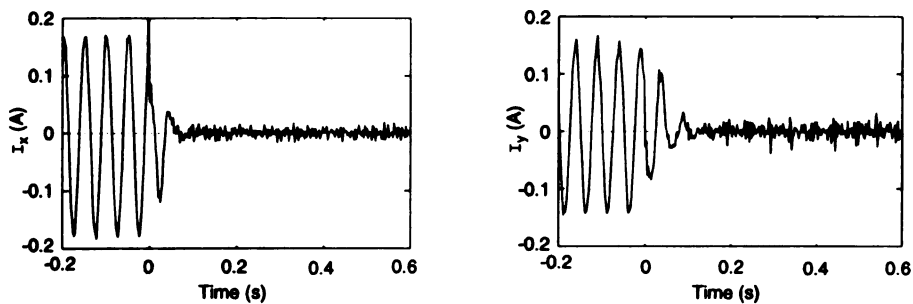


Figure 3.18. Trajectory of control currents

the eq

algorit

mass. n

The

the aver

gence ra

during

ASRC t

method

values ex

The e

well as e

geometric

modeled

compensa

about its

center in t

the equivalent action of integral feedback for elimination of steady state errors. The algorithm is robust to significant variation in plant parameters that include rotor mass, magnetic stiffness, and actuator gain.

The effect of controller gains to the system performance has been evaluated using the averaging method. This approximation method successfully predicts the convergence rate of estimated parameters. Thus, the averaging method can be very useful during control design, in particular during the selection of controller gains of the ASRC to achieve an optimum performance. Furthermore, by using the averaging method we can claim that the estimated parameters ultimately converge to the true values exponentially fast.

The effectiveness of our algorithm is validated through numerical simulations, as well as experiments. We present experimental data that confirm stabilization of the geometric center of a rotor with negligible mass unbalance effects, even when the modeled plant parameters are quite different. Our algorithm can also be used for compensation of mass unbalance, but in such applications the rotor will be stabilized about its inertial center. The problem of rotor stabilization about the geometric center in the presence of both unbalance and rounout will be addressed in Chapter 5.

CH

Sim

Unb

Mult

4.1

In this ch

componen

model des

can indivi

lation resu

4.2 C

The equati

# CHAPTER 4

## Simultaneous Sensor Runout and Unbalance Compensation (SRUC) Using Multiple Speeds

### 4.1 Introduction

In this chapter we present a technique to compensate the effect of the first harmonic components of sensor runout and the unbalance in the single DOF magnetic bearing model described in Chapter 2. Using the technique in this chapter, theoretically, we can individually identify the harmonics components of the two disturbances. Simulation results are presented and implementation issues are also discussed.

### 4.2 Controller Design

The equation of motion, in this case, as given in Eq.(2.3) is

$$m \ddot{x} = K_s x + f_c + f_u \quad (4.1)$$

The

where

The

the

Wi

candid

where

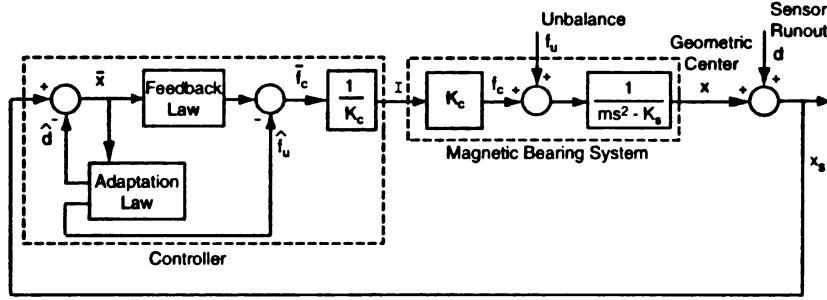


Figure 4.1. Block diagram of SRO and unbalance compensation framework

The estimate of the unbalance force can be written as

$$\hat{f}_u \triangleq \mathbf{Y}_u^T \hat{\phi}_u \quad (4.2)$$

where

$$\mathbf{Y}_u^T \triangleq m\omega^2 [\sin(\omega t) \quad \cos(\omega t)], \quad \hat{\phi}_u \triangleq [\hat{p} \quad \hat{q}]^T \quad (4.3)$$

The terms  $\hat{p}$  and  $\hat{q}$  are estimates of Fourier coefficients  $p$  and  $q$  respectively. We define the errors in the estimation as  $\tilde{p} = p - \hat{p}$ ,  $\tilde{q} = q - \hat{q}$  and

$$\tilde{\phi}_u \triangleq [\tilde{p} \quad \tilde{q}] \quad (4.4)$$

With the objective of converging  $x$  to zero, we propose the Lyapunov function candidate

$$V = \frac{1}{2} \left[ (1 - \Delta)m\bar{e}^2 + \tilde{\phi}^T \Gamma^{-1} \tilde{\phi} + \tilde{\phi}_u^T \Gamma_u^{-1} \tilde{\phi}_u \right] \quad (4.5)$$

$$\Gamma_u \triangleq \text{diag}(\gamma_p, \gamma_q), \quad \Gamma_u \in \mathfrak{R}^{2 \times 2} \quad (4.6)$$

where  $\gamma_p$  and  $\gamma_q$  are positive constants.

In  
starts  
and (2

Further

is chosen

Substitut  
dynamics

Using the  
above equa

From the re

In this Multiple Speeds approach, the top and bottom bias currents  $i_{10}$ ,  $i_{20}$  are constants. Thus, the term  $\Delta$  in Eq.(2.25) is constant. From the definition of Eqs.(2.13) and (2.23), we can establish

$$\dot{\mathbf{Y}}^T \Gamma \mathbf{Y}_m = 0, \quad \text{and} \quad \mathbf{Y}^T \Gamma \dot{\mathbf{Y}}_m = 0 \quad (4.7)$$

Further, the control force

$$f_c = - [K_s \bar{x} + m \lambda \dot{\bar{x}} + c \bar{e} + m \omega^2 [\hat{p} \sin(\omega t) + \hat{q} \cos(\omega t)]] \quad (4.8)$$

is chosen along with the adaptation laws

$$\dot{\tilde{\phi}} = \Gamma \mathbf{Y}_m \bar{e} \quad (4.9)$$

$$\dot{\tilde{\phi}}_u = -\Gamma_u \mathbf{Y}_u \bar{e} \quad (4.10)$$

Substituting Eq.(4.8) into Eq.(4.1) and using Eqs.(2.20) and (4.4), the closed-loop dynamics can be described by

$$m \ddot{x} = -K_s \mathbf{Y}^T \tilde{\phi} - m \lambda \dot{\bar{x}} - c \bar{e} + \mathbf{Y}_u^T \tilde{\phi}_u \quad (4.11)$$

Using the relations  $\ddot{\bar{x}} = \ddot{x} + \ddot{\bar{d}}$  from Eq.(2.16), and  $\dot{\bar{e}} = \dot{\bar{x}} + \lambda \dot{\bar{x}}$  from Eq.(2.22), the above equation can be rewritten as

$$m \dot{\bar{e}} = m \ddot{\bar{d}} - K_s \mathbf{Y}^T \tilde{\phi} - c \bar{e} + \mathbf{Y}_u^T \tilde{\phi}_u \quad (4.12)$$

From the relations in Eqs.(2.20), (2.25), (4.7) and (4.9), we can write

$$\ddot{\bar{d}} = \ddot{\mathbf{Y}}^T \tilde{\phi} + 2\dot{\mathbf{Y}}^T \dot{\tilde{\phi}} + \mathbf{Y}^T \ddot{\tilde{\phi}} \quad (4.13)$$

and E

The de

Utilizin

definite

$V \rightarrow 0$  a

$\Rightarrow \epsilon$  is u

where

Due to th

the first

higher ha

$$= \ddot{\mathbf{Y}}^T \tilde{\phi} + \Delta \dot{\bar{e}} \quad (4.14)$$

and Eq.(4.12) becomes

$$m(1 - \Delta)\dot{\bar{e}} = -\mathbf{Y}_m^T \tilde{\phi} - c\bar{e} + \mathbf{Y}_u^T \tilde{\phi}_u \quad (4.15)$$

The derivative of the Lyapunov function in Eq.(4.5) is

$$\dot{V} = m(1 - \Delta)\dot{\bar{e}}\bar{e} + \tilde{\phi}^T \Gamma^{-1} \dot{\tilde{\phi}} + \tilde{\phi}_u^T \Gamma_u^{-1} \dot{\tilde{\phi}}_u \quad (4.16)$$

Utilizing Eqs.(4.9), (4.10) and (4.15), we obtain  $\dot{V} = -c\bar{e}^2 \leq 0$ . Since  $V$  is positive definite and  $\dot{V}$  is negative semi-definite, by Barbalat's lemma we can conclude that  $\dot{V} \rightarrow 0$  and  $\bar{e} \rightarrow 0$ . Taking the derivative of Eq.(4.15), we can show that  $\ddot{\bar{e}}$  is bounded,  $\Rightarrow \dot{\bar{e}}$  is uniformly continuous,  $\Rightarrow \dot{\bar{e}} \rightarrow 0$ . Therefore, from Eq.(4.15)

$$\mathbf{Y}_{mu}^T \begin{pmatrix} \tilde{\phi} \\ \tilde{\phi}_u \end{pmatrix} \rightarrow 0 \quad \text{as } t \rightarrow \infty \quad (4.17)$$

where

$$\mathbf{Y}_{mu}^T \triangleq [\mathbf{Y}_m^T \quad -\mathbf{Y}_u^T] \quad (4.18)$$

Due to the orthogonality of components, we can separate  $\mathbf{Y}_m$  into  $\mathbf{Y}_\alpha$ , which contains the first harmonic components only, and  $\mathbf{Y}_E$ , which contains the DC, second and higher harmonic components. Thus, the following conditions also hold:

$$\mathbf{Y}_u^T \tilde{\phi}_u - \mathbf{Y}_\alpha^T \tilde{\phi}_\alpha \rightarrow 0 \quad (4.19)$$

$$\mathbf{Y}_E^T \tilde{\phi}_E \rightarrow 0 \quad (4.20)$$

where

It can

where  $I$

(13) as s

Therefo

and  $\hat{b}_1$  fo

On t

sistently

$\tilde{o}_0$  and  $\tilde{o}$

This con

where

where

$$\mathbf{Y}_\alpha^T \triangleq (K_s + m\omega^2) (\sin(\omega t) \quad \cos(\omega t))^T \quad (4.21)$$

$$\mathbf{Y}_E^T \triangleq (K_s \quad \mathbf{Y}_\beta^T) \quad (4.22)$$

$$\mathbf{Y}_\beta \triangleq \begin{pmatrix} (K_s + m(2\omega)^2) \sin(2\omega t) \\ (K_s + m(2\omega)^2) \cos(2\omega t) \\ \vdots \\ (K_s + m(n\omega)^2) \sin(n\omega t) \\ (K_s + m(n\omega)^2) \cos(n\omega t) \end{pmatrix} \quad (4.23)$$

$$\tilde{\phi}_E \triangleq (\tilde{a}_0 \quad \tilde{\phi}_\beta^T)^T \quad (4.24)$$

It can be shown that there exist positive constants  $\alpha_1$ ,  $\alpha_2$ , and  $T_o$ , such that

$$\alpha_2 \mathbf{I} \geq \int_t^{t+T_o} \mathbf{Y}_E \mathbf{Y}_E^T d\tau \geq \alpha_1 \mathbf{I} \quad (4.25)$$

where  $\mathbf{I}_{2n-1}$  is a  $2n-1$  identity matrix. Therefore,  $\mathbf{Y}_E$  is a persistently exciting signal [13] as shown in Appendix C.2. This implies from Eq.(4.20) that  $\tilde{\phi}_E \rightarrow 0$  as  $t \rightarrow \infty$ . Therefore, using the definitions in Eqs.(2.14) and (4.24), we can conclude that  $\hat{a}_0$ ,  $\hat{a}_i$ , and  $\hat{b}_i$  for  $i = 2, \dots, n$  converge to their true values.

On the other hand, in Eq.(4.19) the signal vector  $\mathbf{Y}_{\alpha u} \triangleq (\mathbf{Y}_\alpha \quad \mathbf{Y}_u)^T$  is not persistently exciting in the subspace of  $R^4$ . This implies that the estimated parameters  $\tilde{\phi}_\alpha$  and  $\tilde{\phi}_u$ , instead of converging to zero, converge to a plane in the parameters' space. This condition can be alternatively described by

$$\tilde{a}_1 = \mu \tilde{p} \quad \text{and} \quad \tilde{b}_1 = \mu \tilde{q} \quad (4.26)$$

where

$$\mu(\omega) \triangleq \frac{m\omega^2}{K_s + m\omega^2} \quad (4.27)$$

the  
tions  
are t

where  
matrix  
Wi  
becom

Since  $V$   
can con  
that  $\bar{\epsilon}$ .  
we can  
converge  
 $Y_E$  whic  
before it  
the cond  
 $\Rightarrow \hat{\sigma}_E \rightarrow$   
true value

By operating at two different angular speeds, two values of  $\mu$  can be obtained; and the four unknowns  $a_1$ ,  $b_1$ ,  $p$ , and  $q$  can be determined by solving four algebraic equations given by the expressions in Eq.(4.26). The results of this algebraic calculation are then used to update the adaptation laws to

$$\dot{\hat{\phi}}_\alpha = \Gamma_\alpha \mathbf{Y}_\alpha \bar{e} + \eta_\alpha (\phi_\alpha - \hat{\phi}_\alpha) \quad (4.28a)$$

$$\dot{\hat{\phi}}_E = \Gamma_E \mathbf{Y}_E \bar{e} \quad (4.28b)$$

$$\dot{\hat{\phi}}_u = -\Gamma_u \mathbf{Y}_u \bar{e} + \eta_u (\phi_u - \hat{\phi}_u) \quad (4.28c)$$

where  $\Gamma_\alpha \in \mathfrak{R}^{2 \times 2}$ ,  $\Gamma_E \in \mathfrak{R}^{(2n-1) \times (2n-1)}$ ,  $\eta_\alpha \in \mathfrak{R}^{2 \times 2}$ , and  $\eta_u \in \mathfrak{R}^{2 \times 2}$  are positive definite matrices.

With the new adaptation laws in Eq.(4.28), the Lyapunov derivative in Eq.(4.16) becomes

$$\dot{V} = -c\bar{e}^2 - \tilde{\phi}_\alpha^T \eta_\alpha \tilde{\phi}_\alpha - \tilde{\phi}_u^T \eta_u \tilde{\phi}_u \leq 0 \quad (4.29)$$

Since  $V$  is positive definite and  $\dot{V}$  is negative semi-definite, by Barbalat's lemma we can conclude that  $\dot{V} \rightarrow 0$  and  $\bar{e} \rightarrow 0$ . Taking the derivative of Eq.(4.15), we can show that  $\bar{e}$ ,  $\tilde{\phi}_\alpha$ , and  $\tilde{\phi}_u$  converge to zero as  $t \rightarrow \infty$ . Therefore, using Eqs.(2.14) and (4.4) we can show that  $\hat{a}_1$ ,  $\hat{b}_1$ ,  $\hat{p}$ , and  $\hat{q}$  converge to their true values. Furthermore, the convergence of  $\tilde{\phi}_E$  to zero depends on the persistent excitation of the signal vector  $\mathbf{Y}_E$  which can be claimed using the same arguments as before. From Eq.(4.15), as before it implies that  $\ddot{\bar{e}}$  is bounded,  $\Rightarrow \dot{\bar{e}}$  is uniformly continuous,  $\Rightarrow \bar{e} \rightarrow 0$ . Therefore, the condition in Eq.(4.20) still holds and the signal vector  $\mathbf{Y}_E$  is persistently exciting  $\Rightarrow \tilde{\phi}_E \rightarrow 0$  as  $t \rightarrow \infty$ , which implies that  $\hat{a}_0$ ,  $\hat{a}_i$ , and  $\hat{b}_i$  for  $i = 2, \dots, n$  converge to their true values. In summary, all estimated parameters will converge to zero as  $t \rightarrow \infty$ .

### 4.3 Simulation Results

A numerical simulation of the Multiple Speeds approach was performed using the parameters shown in Table 4.1. Though the controller was designed using a linearized model of the plant, we used the nonlinear plant model in Eqs.(2.1) and (2.2) to simulate the real situation. In the simulation, the SRO identification was arranged to

Table 4.1. Parameters for Simulation

Gains:	$\lambda = 400 s^{-1}, \quad c = 1200 kg/s$ $\Gamma = \text{diag}(1.4, 3, 3, 3, 3) \times 10^{-7} m/N$ $\Gamma_u = \text{diag}(3, 3) \times 10^{-5} m/N$
ICs:	$x(t = 0) = -100 \mu m/s$ $\dot{x}(t = 0) = 0$ $\hat{\phi}(t = 0) = \mathbf{0}, \quad \hat{\phi}_u(t = 0) = \mathbf{0}$
SRO:	$a_0 = 2.5 \mu m$ $a_1 = 18.35 \mu m, \quad b_1 = 4.92 \mu m$ $a_2 = 1.77 \mu m, \quad b_2 = 1.77 \mu m$
Unbalance:	$p = 86.6 \mu m, \quad q = 50.0 \mu m$

adapt up to the second harmonic. The bearing parameters were assumed to be the ones in our experimental hardware listed in Table A.3. In this approach  $i_{10} = i_{10}^*$ ,  $i_{20} = i_{20}^*$ ,  $K_c = K_c^*$ , and  $K_s = K_s^*$ . The rotor angular speed was initially set to 1500 rpm and then increased linearly at  $t = 0.4 s$  to 2100 rpm within 0.2 s. The angular speed was held constant after  $t = 0.6 s$ . After computation of the true values of  $a_1$ ,  $b_1$ ,  $p$ , and  $q$  had been accomplished, the adaptation law was switched from using Eqs.(4.9) and (4.10) to Eq.(4.28) at  $t = 1 s$ . We used  $\Gamma_\alpha = \text{diag}(3, 3) \times 10^{-7} m/N$ ,  $\Gamma_E = \text{diag}(1.4, 3, 3) \times 10^{-7} m/N$ ,  $\eta_\alpha = \text{diag}(10, 10) s^{-1}$ , and  $\eta_u = \text{diag}(10, 10) s^{-1}$ .

It can be observed in Figures 4.2 and 4.3 that  $\hat{a}_1$ ,  $\hat{b}_1$ ,  $\hat{p}$ , and  $\hat{q}$  reach different steady states values for each angular speed while the DC and second harmonics components

of SRO,  $\hat{a}_0$ ,  $\hat{a}_2$ ,  $\hat{b}_2$  converge to their true values within 0.2 s for each speed. After  $t = 1.5$  s, all estimated parameters have converged to the true values. At this time, as shown in Figure 4.2 the rotor is stabilized to the origin. Unmodeled effects due to angular speed acceleration can be seen  $t$  between 0.4 s and 0.6 s. We avoid further discussion on this topic but advice to change the angular speed slowly.

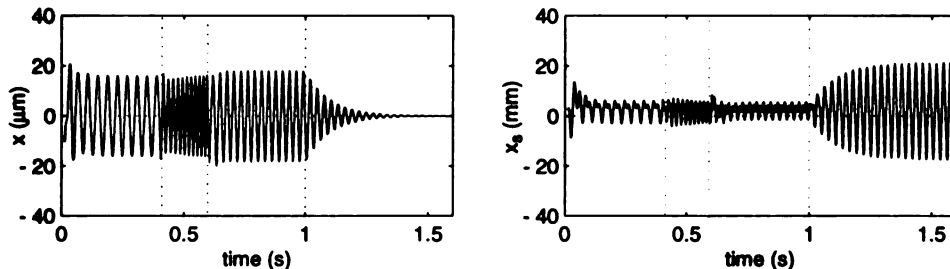


Figure 4.2. Geometric center  $x$  and sensor signal with runout  $x_s$ ,

## 4.4 Practical Implementation Issues

In implementation, the Multiple Speeds approach suffers several major drawbacks. First, the results of the algebraic calculation is very sensitive to the value of  $\mu$ . Uncertainty in  $m$ ,  $K_s$ , and  $\omega$  may easily yield to a large calculation error. Secondly, the approach practically requires two far away operating speeds in order to decouple the four algebraic equations. Third, the controller was derived using the Lyapunov method by assuming a constant angular speed. Thus, the stability during the changing angular speed is not guaranteed. Moreover, in many applications changing the angular speed may not be desirable.

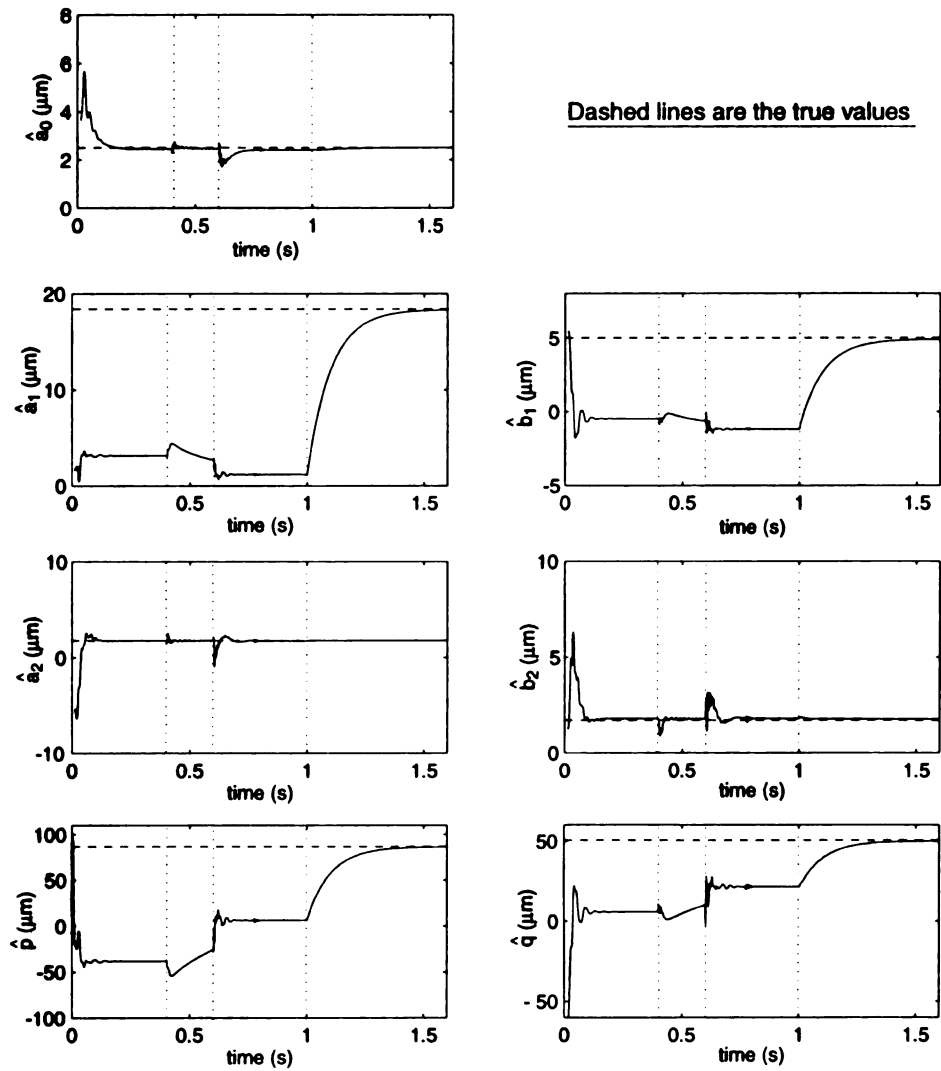


Figure 4.3. Estimated Fourier coefficients

## 4.5 Summary and Remarks

We have presented the technique that can be used to identify the synchronous disturbance of sensor runout and unbalance. The technique requires the rotor to be spun at two different angular speeds because only partial convergence of the estimated parameters is achieved in Eq.(4.17). In the adaptive control, this problem is attributed to the lack of "sufficient richness" [31], which means that the regressor vector does not contain enough frequencies for the parameter error to converge to zero. In the partial convergence condition, estimated parameters may drift even with small external disturbance [31]. It is generally known [25, 31, 36] that for linear systems,  $r$  sinusoids or frequencies in the regressor vector provides for the convergent estimation of  $(2r + 1)$  parameters. It can be observed that the regressor vector in Eq.(4.17) has  $r = n$  frequencies while the number of parameters to be estimated is  $(2n + 3)$ . This observation suggests that additional perturbations with frequencies other than the frequencies already contained in the regressor vector will facilitate convergence of the parameters.

# CHAPTER 5

## Simultaneous Sensor Runout and Unbalance Compensation (SRUC) via Bias Current Excitation (BCE)

### 5.1 Introduction

In this section we present a new algorithm for rotor stabilization about its geometric center in the presence of both unbalance and sensor runout. The new algorithm effectively compensates the effects of both unbalance and runout at constant rotor speed and is based on the adaptive control framework presented in Chapter 4. The control framework is recognized to have a unique feature that allows us to directly perturb the parameter in the regressor vector to create a persistently exciting condition. This is achieved through variation of the bias currents in opposing electromagnetic coils in a manner that does not alter the equilibrium condition of the rotor. The method of bias current excitation is discussed in section 5.2. The mathematical foundation of the adaptive algorithm is laid in section 5.3 and robustness of the algorithm is investigated in section 5.4. Simulation results are presented in sections 5.5 and 5.6, and experimental results are presented and discussed in section 5.7, 5.8 and 5.9. Section 5.10 provides a summary of the main contribution and concluding remarks.

Cons

With  
intenc  
that d

In Eq.  
the to

and its

where

## 5.2 Adaptive Control with Bias Current Excitation

Consider the magnetic bearing model shown in Eqs.(2.1) and (2.2)

$$m \ddot{x} = F - m \bar{g} + f_u, \quad \bar{g} \triangleq g/\sqrt{2} \quad (5.1)$$

$$F = k \left[ \left( \frac{i_{10} + I}{l - x} \right)^2 - \left( \frac{i_{20} - I}{l + x} \right)^2 \right] \quad (5.2)$$

Without changing the angular speed, in order to generate persistence excitation, we intend to perturb the top and bottom bias currents  $i_{10}$  and  $i_{20}$  by  $\delta_1$  and  $\delta_2$  in manner that does not alter the equilibrium condition of the rotor:

$$i_{10} = i_{10}^* + \delta_1, \quad i_{20} = i_{20}^* + \delta_2 \quad (5.3)$$

In Eq.(5.3)  $i_{10}^*$  and  $i_{20}^*$  are constant currents in the top and bottom coils. Therefore, the total magnetic force shown Eq.(5.2) becomes

$$F(x, I, \delta_1, \delta_2) = k \left[ \left( \frac{i_{10}^* + \delta_1 + I}{l - x} \right)^2 - \left( \frac{i_{20}^* + \delta_2 - I}{l + x} \right)^2 \right] \quad (5.4)$$

and its linearization about  $x = 0$  and  $I = 0$  yields

$$F(x, I, \delta_1, \delta_2) \approx F(0, 0, \delta_1, \delta_2) + \left. \frac{\partial F}{\partial x} \right|_{\substack{x=0 \\ I=0}} x + \left. \frac{\partial F}{\partial I} \right|_{\substack{x=0 \\ I=0}} I \quad (5.5)$$

where

$$F(0, 0, \delta_1, \delta_2) = k \left[ \left( \frac{i_{10}^* + \delta_1}{l} \right)^2 - \left( \frac{i_{20}^* + \delta_2}{l} \right)^2 \right] \quad (5.6)$$

$$\left. \frac{\partial F}{\partial x} \right|_{\substack{x=0 \\ I=0}} = K_s(\delta_1, \delta_2) = \frac{2k}{l^3} [(i_{10}^* + \delta_1)^2 + (i_{20}^* + \delta_2)^2] \quad (5.7)$$

Ac

ab

wh

It ca

the

Furt

be ex

where

$$\left. \frac{\partial F}{\partial I} \right|_{\substack{i=0 \\ \dot{i}=0}} = K_c(\delta_1, \delta_2) = \frac{2k}{l^2} [i_{10}^* + \delta_1 + i_{20}^* + \delta_2] \quad (5.8)$$

Additionally, the bias force in Eq.(5.6) can also be approximated by linearization about  $\delta_1 = 0$  and  $\delta_2 = 0$ .

$$F(0, 0, \delta_1, \delta_2) \approx F(0) + \left. \frac{\partial F(0, 0, \delta_1, \delta_2)}{\partial \delta_1} \right|_{\substack{\delta_1=0 \\ \delta_2=0}} \delta_1 + \left. \frac{\partial F(0, 0, \delta_1, \delta_2)}{\partial \delta_2} \right|_{\substack{\delta_1=0 \\ \delta_2=0}} \delta_2 \quad (5.9)$$

where

$$F(0) = \frac{k}{l^2} (i_{10}^{*2} - i_{20}^{*2}) \quad (5.10)$$

$$\left. \frac{\partial F(0, 0, \delta_1, \delta_2)}{\partial \delta_1} \right|_{\substack{\delta_1=0 \\ \delta_2=0}} = \frac{2i_{10}^*}{l^2} \delta_1 \quad (5.11)$$

$$\left. \frac{\partial F(0, 0, \delta_1, \delta_2)}{\partial \delta_2} \right|_{\substack{\delta_1=0 \\ \delta_2=0}} = -\frac{2i_{20}^*}{l^2} \delta_2 \quad (5.12)$$

It can be seen that if we choose

$$\delta_2 = \frac{i_{10}^*}{i_{20}^*} \delta_1 \quad (5.13)$$

the effect of the bias current excitation to the bias force in Eq.(5.9) is negligible

$$F\left(0, 0, \delta_1, \delta_2 = \frac{i_{10}^*}{i_{20}^*} \delta_1\right) \approx F(0) \quad (5.14)$$

Furthermore, the open loop stiffness and the actuator gain in Eqs.(5.7) and (5.8) can be expressed as function of  $\delta_1$  only and approximated by

$$K_s(\delta_1) \approx K_s^* + \left. \frac{\partial K_s}{\partial \delta_1} \right|_{\delta_1=0} \delta_1 \quad (5.15)$$

$$K_c(\delta_1) \approx K_c^* + \left. \frac{\partial K_c}{\partial \delta_1} \right|_{\delta_1=0} \delta_1 \quad (5.16)$$

where

$$K_s^* \triangleq 2k (i_{10}^{*2} + i_{20}^{*2}) / l^3 \quad K_c^* \triangleq 2k (i_{10}^* + i_{20}^*) / l^2 \quad (5.17)$$

wh  
valu  
to l  
later  
In  
except

when

and f

Th

the bl

$$\left. \frac{\partial K_s}{\partial \delta_1} \right|_{\delta_1=0} = \frac{8ki_{i0}^*}{l^3} \quad (5.18)$$

$$\left. \frac{\partial K_c}{\partial \delta_1} \right|_{\delta_1=0} = \frac{2k}{l^2} \left( 1 + \frac{i_{i0}^*}{i_{20}^*} \right) \quad (5.19)$$

For simplicity, we may choose the excitation as

$$\delta_1 = A \sin(\omega_e t), \quad \omega_e \triangleq 2\pi f_e \quad (5.20)$$

where  $A$  is the amplitude of excitation,  $f_e$  is the frequency of the excitation. The value of  $A$  should be chosen such that the above linearization is valid;  $A$  at about 10 to 15 % of  $i_{i0}^*$  may be used. The effect of using several different values of  $A$  and  $f_e$  is later discussed in sections 5.2 and 5.3.

In summary we again obtain the same linearized model as in Eq.(2.3) with the exception that  $K_s$  and  $K_c$  are now time varying.

$$m \ddot{x} = K_s x + K_c I + f_u \quad (5.21)$$

where

$$K_s = K_s^* + \xi_s \sin(\omega_e t), \quad \xi_s \triangleq \frac{8ki_{i0}^*}{l^3} A \quad (5.22)$$

$$K_c = K_c^* + \xi_c \sin(\omega_e t), \quad \xi_c \triangleq \frac{2kA}{l^2} \left( 1 + \frac{i_{i0}^*}{i_{20}^*} \right) \quad (5.23)$$

and  $f_u$  is defined in Eq.(2.7).

The proposed framework of SRUC using bias current excitation is illustrated by the block diagram in Figure 5.1 in which we define the feedback law as

$$I = -\frac{1}{K_c} \left[ K_s \bar{x} + m\lambda \dot{\bar{x}} + (c + \frac{1}{2}m\dot{\Delta})\bar{e} + \mathbf{Y}_u^T \hat{\phi}_u \right] \quad (5.24)$$

and

when

lambda

when

The

vector

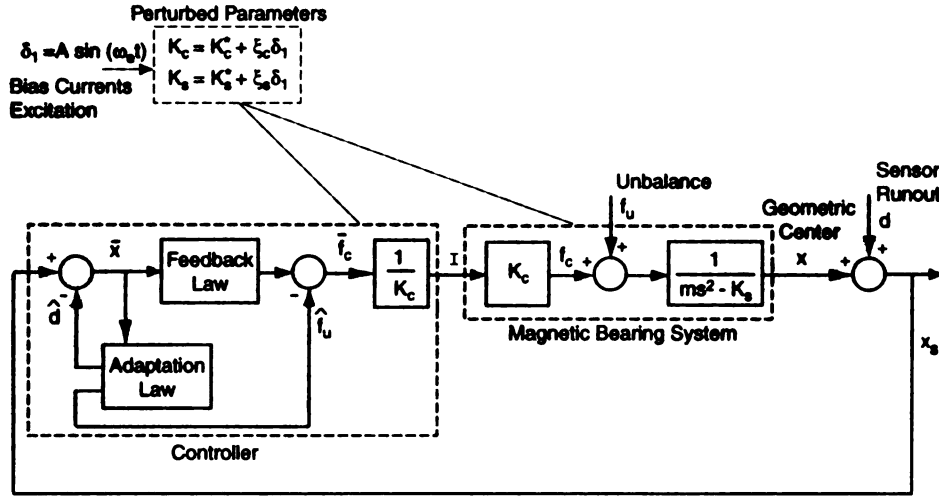


Figure 5.1. Block diagram of SRUC via bias current excitation

along with adaptation laws

$$\dot{\tilde{\phi}} = \Gamma Y_m \bar{e} \quad (5.25)$$

$$\dot{\tilde{\phi}}_u = -\Gamma_u Y_u \bar{e} \quad (5.26)$$

where  $\bar{x}$ ,  $\bar{e}$ ,  $\Gamma$  and  $Y_m$  are defined in Eqs.(2.16), (2.22), (2.24) and (2.23) respectively.

$\lambda$  and  $c$  are positive constants

$$\Gamma_u \triangleq \text{diag}(\gamma_p, \gamma_q), \quad \Gamma_u \in \mathfrak{R}^{2 \times 2} \quad (5.27)$$

where  $\gamma_p$  and  $\gamma_q$  are positive constants, and

$$Y_u^T \triangleq m\omega^2 [\sin(\omega t) \quad \cos(\omega t)], \quad \hat{\phi}_u \triangleq [\hat{p} \quad \hat{q}]^T \quad (5.28)$$

The terms  $\hat{p}$  and  $\hat{q}$  are estimates of Fourier coefficients  $p$  and  $q$ . The parameter error vector for the unbalance component can be written as

$$\tilde{\phi}_u \triangleq [\tilde{p} \quad \tilde{q}], \quad \tilde{p} \triangleq p - \hat{p}, \quad \tilde{q} \triangleq q - \hat{q} \quad (5.29)$$

5

T

st

va

Ec

by

Us

ab

Fro

The term  $\dot{\bar{x}}$  is obtained by taking the derivative of the measured signal  $\bar{x}$ . The term  $\dot{\Delta}$  can be derived from Eq.(2.25) knowing that  $\dot{\mathbf{Y}}^T \Gamma \mathbf{Y}_m = 0$ ,  $\dot{\mathbf{Y}}^T \Gamma \dot{\mathbf{Y}} = 0$ , and  $\dot{\mathbf{Y}}^T \Gamma \mathbf{Y}^{(3)} = 0$ .

$$\dot{\Delta} = \mathbf{Y}^T \Gamma \dot{\mathbf{Y}}_m = \dot{K}_s \sum_{i=0}^n \gamma_i \quad \text{where} \quad \dot{K}_s = \xi_s \omega_e \cos(\omega_e t) \quad (5.30)$$

It should be noticed that  $\gamma_i$  is the diagonal components of the adaptation gain  $\Gamma$ ; and the adaptation law in Eq.(5.25) has the regressor vector  $\mathbf{Y}_m$  that now varies according to  $K_s$ .

### 5.3 Proof of Stability and Parameter Convergence

The control and adaptation laws presented in Eqs.(5.24), (5.25), and (5.26) stabilizes the closed-loop system and converges all estimated parameters to their true values. This can be proven in the following manner. Substituting Eq.(5.24) into Eq.(5.21) and using Eq.(2.20), the dynamics of the controlled rotor can be described by

$$m \ddot{x} = -K_s \mathbf{Y}^T \tilde{\phi} - m \lambda \dot{x} - (c + \frac{1}{2} m \dot{\Delta}) \bar{e} + \mathbf{Y}_u^T \tilde{\phi}_u \quad (5.31)$$

Using the relations  $\ddot{\tilde{x}} = \ddot{x} + \ddot{d}$  from Eq.(2.16), and  $\dot{\tilde{e}} = \dot{\bar{e}} + \lambda \dot{x}$  from Eq.(2.22), the above equation can be rewritten as

$$m \dot{\tilde{e}} = m \ddot{d} - K_s \mathbf{Y}^T \tilde{\phi} - (c + \frac{1}{2} m \dot{\Delta}) \bar{e} + \mathbf{Y}_u^T \tilde{\phi}_u \quad (5.32)$$

From Eqs.(2.20) and (5.25), we can write

$$\ddot{d} = \ddot{\mathbf{Y}}^T \tilde{\phi} + 2 \dot{\mathbf{Y}}^T \dot{\tilde{\phi}} + \mathbf{Y}^T \ddot{\tilde{\phi}} \quad (5.33)$$

$$= \ddot{\mathbf{Y}}^T \tilde{\phi} + 2 \dot{\mathbf{Y}}^T \Gamma \mathbf{Y}_m \dot{\tilde{e}} + \mathbf{Y}^T \Gamma \dot{\mathbf{Y}}_m \bar{e} + \mathbf{Y}^T \Gamma \mathbf{Y}_m \dot{\tilde{e}} \quad (5.34)$$

w

F

l

cc

d

=

we

the

As sh

Knowing  $\dot{\mathbf{Y}}^T \Gamma \mathbf{Y}_m = 0$  and Eq.(2.25) the above equation becomes

$$\ddot{d} = \ddot{\mathbf{Y}}^T \tilde{\phi} + \dot{\Delta} \bar{e} + \Delta \dot{\bar{e}} \quad (5.35)$$

Utilizing Eqs.(2.23) and (5.35), we can express Eq.(5.32) as

$$m(1 - \Delta) \dot{\bar{e}} = -\mathbf{Y}_m^T \tilde{\phi} + \frac{1}{2} m \dot{\Delta} \bar{e} - c \bar{e} + \mathbf{Y}_u^T \tilde{\phi}_u \quad (5.36)$$

Using the Lyapunov function candidate

$$V = \frac{1}{2} \left[ (1 - \Delta) m \bar{e}^2 + \tilde{\phi}^T \Gamma^{-1} \tilde{\phi} + \tilde{\phi}_u^T \Gamma_u^{-1} \tilde{\phi}_u \right] \quad (5.37)$$

we obtain

$$\dot{V} = m(1 - \Delta) \dot{\bar{e}} \bar{e} - \frac{1}{2} m \dot{\Delta} \bar{e}^2 + \tilde{\phi}^T \Gamma^{-1} \dot{\tilde{\phi}} + \tilde{\phi}_u^T \Gamma_u^{-1} \dot{\tilde{\phi}}_u \quad (5.38)$$

From Eqs.(5.25), (5.26) and (5.36), we get  $\dot{V} = -c \bar{e}^2 \leq 0$ . Again, positive definite in  $V$  and negative semi-definite in  $\dot{V}$  imply  $\bar{e} \rightarrow 0$  as  $t \rightarrow \infty$ . Knowing  $\ddot{V}$  is uniformly continuous, from Barbalat's Lemma [13], we can claim that  $\dot{V} \rightarrow 0 \Rightarrow \bar{e} \rightarrow 0$ . Taking derivative of Eq.(5.36), we can show that  $\ddot{\bar{e}}$  is bounded  $\Rightarrow \dot{\bar{e}}$  is uniformly continuous  $\Rightarrow \dot{\bar{e}} \rightarrow 0$ . Therefore, similar to the conditions in Eqs.(4.19) and (4.20) except now we do not need to separate the components of  $\mathbf{Y}_m$ , from Eq.(5.36) we can argue that

$$\mathbf{Y}_{mu}^T \begin{pmatrix} \tilde{\phi} \\ \tilde{\phi}_u \end{pmatrix} \rightarrow 0 \quad \text{as } t \rightarrow \infty \quad (5.39)$$

where

$$\mathbf{Y}_{mu}^T \triangleq [\mathbf{Y}_m^T \quad -\mathbf{Y}_u^T] \quad (5.40)$$

As shown in Appendix B.3, if  $\omega_e \neq \omega$  then  $\mathbf{Y}_{mu}^T$  is a persistently exciting signal [13],

which can be verified from the condition

$$\alpha_2 \mathbf{I} \geq \int_t^{t+T_o} \mathbf{Y}_{mu} \mathbf{Y}_{mu}^T d\tau \geq \alpha_1 \mathbf{I} \quad (5.41)$$

where  $\alpha_1$ ,  $\alpha_2$ , and  $T_o$  are positive constants and  $\mathbf{I}$  is a  $2n+3$  identity matrix, we can conclude that  $\tilde{\phi} \rightarrow 0$  and  $\tilde{\phi}_u \rightarrow 0$ . Therefore  $\hat{a}_0$ ,  $\hat{a}_i$ , and  $\hat{b}_i$  for  $i = 1, \dots, n$  and  $\hat{p}$  and  $\hat{q}$  all converge to their true values.

From Eqs.(5.25), (5.26) and (5.36), the closed-loop dynamics can be written as

$$\dot{\bar{x}} = -\lambda \bar{x} + \bar{e} \quad (5.42a)$$

$$m(1 - \Delta)\dot{\bar{e}} = -\mathbf{Y}_m^T \tilde{\phi} + \frac{1}{2}m\Delta\dot{\bar{e}} - c\bar{e} + \mathbf{Y}_u^T \tilde{\phi}_u \quad (5.42b)$$

$$\dot{\tilde{\phi}} = \Gamma \mathbf{Y}_m \bar{e} \quad (5.42c)$$

$$\dot{\tilde{\phi}}_u = \Gamma_u \mathbf{Y}_u \bar{e} \quad (5.42d)$$

Thus, we can make the following observations.

**Lemma 5.1** *The origin of the closed-loop system in Eq.(5.42),  $(\bar{x}, \bar{e}, \tilde{\phi}, \tilde{\phi}_u) \equiv (0, 0, 0, 0)$ , is an asymptotically stable equilibrium point.*

**Proof:** The closed loop system in Eq.(5.42) is an interconnected system of the form

$$\dot{z}_1 = f_1(t, z_1, z_2) \quad (5.43a)$$

$$\dot{z}_2 = f_2(t, z_2) \quad (5.43b)$$

where  $z_1 \triangleq \bar{x}$ , and  $z_2 \triangleq (\bar{e} \quad \tilde{\phi}^T \quad \tilde{\phi}_u^T)^T$  are the state variables of the two sub-systems.

We know previously that  $z_2 = 0$  is an asymptotically stable equilibrium of the sub-system in Eq.(5.43b). Also,  $\dot{z}_1 = f_2(t, z_1, 0)$  has an asymptotically stable equilibrium point at  $z_1 = 0$ . This can be readily established from Eqs.(5.42b) and (5.43a). Us-

ing

(i.

Th

for

tha

Also

Eq.

fore.

(0.0

1.

2

ing the asymptotic stability theorem for cascaded systems [13], we conclude that  $(\bar{x}, \bar{e}, \tilde{\phi}, \tilde{\phi}_u) \equiv (0, 0, 0, 0)$ , is an asymptotically stable equilibrium.

**Theorem 5.1** *The coordinate  $(x, \dot{x}, \tilde{\phi}, \tilde{\phi}_u) \equiv (0, 0, 0, 0)$  is a stable equilibrium point for the closed loop system defined by Eqs.(5.21) through (5.26).*

**Proof:** : Using Eqs.(2.19), (2.20), (2.25), (5.42a) and (5.42b) , we can show that at  $(x, \dot{x}, \tilde{\phi}, \tilde{\phi}_u) \equiv (0, 0, 0, 0)$ , we have

$$\tilde{d} = \mathbf{Y}^T \tilde{\phi} = 0, \quad \bar{x} = x + \tilde{d} = 0,$$

$$\dot{\tilde{d}} = (\dot{\mathbf{Y}}^T \tilde{\phi} + \mathbf{Y}^T \dot{\tilde{\phi}}) = \mathbf{Y}^T \Gamma \mathbf{Y}_m \bar{e} = \Delta \bar{e} = \Delta(\dot{x} + \lambda \bar{x}) = \Delta \dot{x}$$

Also, at  $(x, \dot{x}, \tilde{\phi}, \tilde{\phi}_u) \equiv (0, 0, 0, 0)$ ,  $\dot{\tilde{d}} = (\dot{x} - \dot{x}) = \dot{x} = 0$ , since  $0 < \Delta < 1$ . From Eqs.(5.31), (5.42c), and (5.42d), it follows that  $(\dot{x}, \ddot{x}, \dot{\tilde{\phi}}, \dot{\tilde{\phi}}_u) = (0, 0, 0, 0)$ . Therefore,  $(x, \dot{x}, \tilde{\phi}, \tilde{\phi}_u) \equiv (0, 0, 0, 0)$  is an equilibrium point. The fact that  $(x, \dot{x}, \tilde{\phi}, \tilde{\phi}_u) \equiv (0, 0, 0, 0)$  is asymptotically stable can now be deduced from:

1. The equilibrium point  $(\bar{x}, \bar{e}, \tilde{\phi}, \tilde{\phi}_u) \equiv (0, 0, 0, 0)$  is an asymptotically stable equilibrium. This fact follows from Lemma 5.1,
2. The transformation matrix  $\mathbf{P}$  that maps  $(\bar{x}, \bar{e}, \tilde{\phi}, \tilde{\phi}_u)$  to  $(x, \dot{x}, \tilde{\phi}, \tilde{\phi}_u)$

$$\begin{pmatrix} x \\ \dot{x} \\ \tilde{\phi} \\ \tilde{\phi}_u \end{pmatrix} = \begin{pmatrix} \mathbf{P} \end{pmatrix} \begin{pmatrix} \bar{x} \\ \bar{e} \\ \tilde{\phi} \\ \tilde{\phi}_u \end{pmatrix} \quad (5.44)$$

$$\mathbf{P} \triangleq \begin{pmatrix} 1 & 0 & -\mathbf{Y}^T & 0 \\ -\lambda & (1 - \Delta) & -\dot{\mathbf{Y}}^T & 0 \\ 0 & 0 & \mathbf{E}_{2n+1} & 0 \\ 0 & 0 & 0 & \mathbf{E}_2 \end{pmatrix} \quad (5.45)$$

n

ce

id

**5.**

Th

K,

aly

Out

par

**5.4**

In i

m. v

assu

adap

where  $\mathbf{E}_{2n+1} \in \mathfrak{R}^{(2n+1) \times (2n+1)}$  and  $\mathbf{E}_2 \in \mathfrak{R}^{(2) \times (2)}$  are the identity matrices, is well defined and upper bounded, and

3. The inverse transformation  $\mathbf{P}^{-1}$  exists, and  $\|\mathbf{P}^{-1}\|$  is also upper bounded.

The above theorem establishes that our adaptive controller, in conjunction with sinusoidal excitation of the bias current, guarantees stabilization of the rotor geometric center in the presence of both SRO and unbalance. This achieved through individual identification and feedforward cancellation of both SRO and unbalance disturbances.

## 5.4 Robustness to Parameter Uncertainties

The effect of uncertainties in plant parameters namely mass  $m$ , open-loop stiffness  $K_s$ , and actuator gain  $K_c$ , to the performance of the SRUC-BCE algorithm is analyzed in this section by considering uncertainty in each parameter independently. Our particular interest is to evaluate the behavior of the rotor geometric center and parameter estimates.

### 5.4.1 Mass Uncertainty

In implementation, we used a mass value of  $\bar{m} \triangleq \rho_m + m$  instead of the nominal value  $m$ , where  $m$  is the nominal mass and  $\rho_m$  is the mass uncertainty. It is reasonable to assume that  $\rho_m$  is constant and  $|\rho_m| < m$ . The feedback law in Eq.(5.24) and the adaptation laws in Eqs.(5.25) and (5.26) become

$$I = -\frac{1}{K_c} \left[ K_s \bar{x} + \bar{m} \lambda \dot{\bar{x}} + (c + \frac{1}{2} \bar{m} \dot{\Delta}) \bar{e} + (1 + \frac{\rho_m}{m}) \mathbf{Y}_u^T \hat{\phi}_u \right] \quad (5.46)$$

$$\dot{\hat{\phi}} = \mathbf{\Gamma} \bar{\mathbf{Y}}_m \bar{e} \quad \dot{\hat{\phi}}_u = -(1 + \frac{\rho_m}{m}) \mathbf{\Gamma}_u \mathbf{Y}_u \bar{e} \quad (5.47)$$

$$\bar{\mathbf{Y}}_m \triangleq K_s \mathbf{Y} - \bar{m} \ddot{\mathbf{Y}} \quad (5.48)$$

Substituting Eqs.(2.19), (2.20) and (5.46) to Eq.(5.21) we obtain

$$m \ddot{\bar{x}} - m \ddot{\bar{d}} = -K_s \mathbf{Y}^T \tilde{\phi} - \bar{m} \lambda \dot{\bar{x}} - \left(c + \frac{1}{2} \bar{m} \dot{\Delta}\right) \bar{e} + \mathbf{Y}_u^T \tilde{\phi}_u - \frac{\rho_m}{m} \mathbf{Y}_u^T \hat{\phi}_u \quad (5.49)$$

From Eqs.(2.20) and (5.47), we can write

$$\begin{aligned} \ddot{\bar{d}} &= \ddot{\mathbf{Y}}^T \tilde{\phi} + 2\dot{\mathbf{Y}}^T \dot{\tilde{\phi}} + \mathbf{Y}^T \ddot{\tilde{\phi}} \\ &= \ddot{\mathbf{Y}}^T \tilde{\phi} + \dot{\Delta} \bar{e} + \bar{\Delta} \dot{\bar{e}} \end{aligned} \quad (5.50)$$

where

$$\bar{\Delta} \triangleq \mathbf{Y}^T \Gamma \bar{\mathbf{Y}}_m = \sum_{i=0}^n \gamma_i (K_s + \bar{m}(i\omega)^2) \quad (5.51)$$

$$\dot{\Delta} = \dot{\bar{\Delta}} = \dot{K}_s \sum_{i=0}^n \gamma_i \quad (5.52)$$

Therefore, in view of Eqs.(2.22), (5.48), and (5.50) we can rewrite the dynamics in Eq.(5.49) as a linear time-varying system with an input of  $u_1$

$$M(t) \ddot{\bar{x}} + C(t) \dot{\bar{x}} + K(t) \bar{x} = u_1(t) \quad (5.53)$$

where

$$u_1(t) \triangleq -\mathbf{Y}_m^T \tilde{\phi} + \mathbf{Y}_u^T \tilde{\phi}_u - \frac{\rho_m}{m} \mathbf{Y}_u^T \hat{\phi}_u \quad (5.54)$$

$$M(t) \triangleq m(1 - \bar{\Delta})$$

$$C(t) \triangleq c + \frac{1}{2} \bar{m} \dot{\Delta} + (\bar{m} - m \bar{\Delta}) \lambda - m \dot{\Delta}$$

$$K(t) \triangleq \left[ c + \left( \frac{1}{2} \bar{m} - m \right) \dot{\Delta} \right] \lambda$$

The left hand side of Eq.(5.53) can always be recast to a state space representation  $H_1(\mathbf{A}(t), \mathbf{B}(t), \mathbf{C}(t))$  shown in Eq.(D.6) such that its input  $u_1$  is defined by Eq.(5.54) and the output  $y_1 = \bar{e}$  knowing Eq.(2.22). The closed-loop system can be viewed as

a feedback configuration illustrated in Figure D.1. Notice that  $\mathbf{A}(t)$ ,  $\mathbf{B}(t)$ , and  $\mathbf{C}(t)$  are bounded since  $M(t)$ ,  $C(t)$ , and  $K(t)$  can be seen as having nominal parameters with the addition of relatively small periodic perturbations.

Using the adaptation laws in Eqs.(5.47) and (5.26) we can view the system in the feedback path  $H_2$  having  $u_2 = \bar{e}$  as the input and  $y_2 = \mathbf{Y}_m^T \tilde{\phi} - \mathbf{Y}_u^T \tilde{\phi}_u + \frac{\rho_m}{m} \mathbf{Y}_u^T \hat{\phi}_u$  as the output. For a sufficiently small  $\rho_m$  we can prove  $H_2$  is a passive system as shown by lemma D.2. in Appendix D. Assuming that  $H_1$  remains strictly passive and satisfies the conditions in definition D.3, the following observation can be made regarding the convergence of the estimated parameters.

1. As  $t \rightarrow \infty$ , by theorem D.1 we can claim that  $\bar{x}$ ,  $\dot{\bar{x}}$ ,  $\ddot{\bar{x}}$  and  $\bar{e}$  converges to zero.
2. From Eq.(5.53)

$$\begin{pmatrix} \bar{\mathbf{Y}}_m^T & -\mathbf{Y}_u^T \end{pmatrix} \begin{pmatrix} \tilde{\phi} \\ \phi_u - (1 + \frac{\rho_m}{m})\hat{\phi}_u \end{pmatrix} \rightarrow 0 \quad (5.55)$$

3. The persistence of excitation in the regressor vector yields

$$\begin{aligned} \tilde{\phi} &\rightarrow 0 \\ \phi_u - (1 + \frac{\rho_m}{m})\hat{\phi}_u &\rightarrow 0 \end{aligned}$$

Therefore the estimate parameters of the SRO converge to the true values while the estimate parameters of the unbalance  $\hat{\phi}_u \rightarrow \frac{m}{m + \rho_m} \phi_u$

4. Since  $\bar{x} \rightarrow 0$  and  $\tilde{\phi} \rightarrow 0$ , from Eqs.(2.19) and (2.20) we can argue that  $x \rightarrow 0$ .

In conclusion, the rotor geometric center is still stabilized to the origin despite of mass uncertainty. However, this conclusion is true only as long as  $H_1$  remains strictly passive. The passivity of  $H_1$  depends on the nominal plant parameters and the choice of controller gains besides the level of the uncertainty in the mass parameter.

Su

Fro

## 5.4.2 Magnetic Stiffness Uncertainty

The uncertainty in the open-loop stiffness parameter is studied by assuming that the controller uses the  $\bar{K}_s \triangleq \rho_s + K_s$  where  $\rho_s$  is the amount of the uncertainty. Due to the excitation on the bias currents, it is logical to assume that  $\rho_s$  is time varying and  $|\rho_s|_{max} < K_s$ . The feedback law in Eq.(5.24) and the adaptation law for the SRO in Eq.(5.25) become

$$I = -\frac{1}{K_c} \left[ \bar{K}_s \bar{x} + m\lambda \dot{\bar{x}} + \left(c + \frac{1}{2}m\dot{\bar{\Delta}}\right)\bar{e} + \mathbf{Y}_u^T \hat{\phi}_u \right] \quad (5.56)$$

$$\dot{\hat{\phi}} = \Gamma \bar{\mathbf{Y}}_m \bar{e}, \quad (5.57)$$

$$\bar{\mathbf{Y}}_m \triangleq \bar{K}_s \mathbf{Y} - m\ddot{\mathbf{Y}} \quad (5.58)$$

Note that the adaptation law due to the unbalance part is the same as in Eq.(5.26).

Since  $\dot{\rho}_s \neq 0$  we obtain the following.

$$\dot{\bar{\mathbf{Y}}}_m = \dot{\mathbf{Y}}_m + \dot{\rho}_s \mathbf{Y} + \rho_s \dot{\mathbf{Y}} \quad (5.59)$$

$$\bar{\Delta} = \mathbf{Y}^T \Gamma \bar{\mathbf{Y}}_m = \Delta + \rho_s \mathbf{Y}^T \Gamma \mathbf{Y} = \Delta + \rho_s \sum_{i=0}^n \gamma_i \quad (5.60)$$

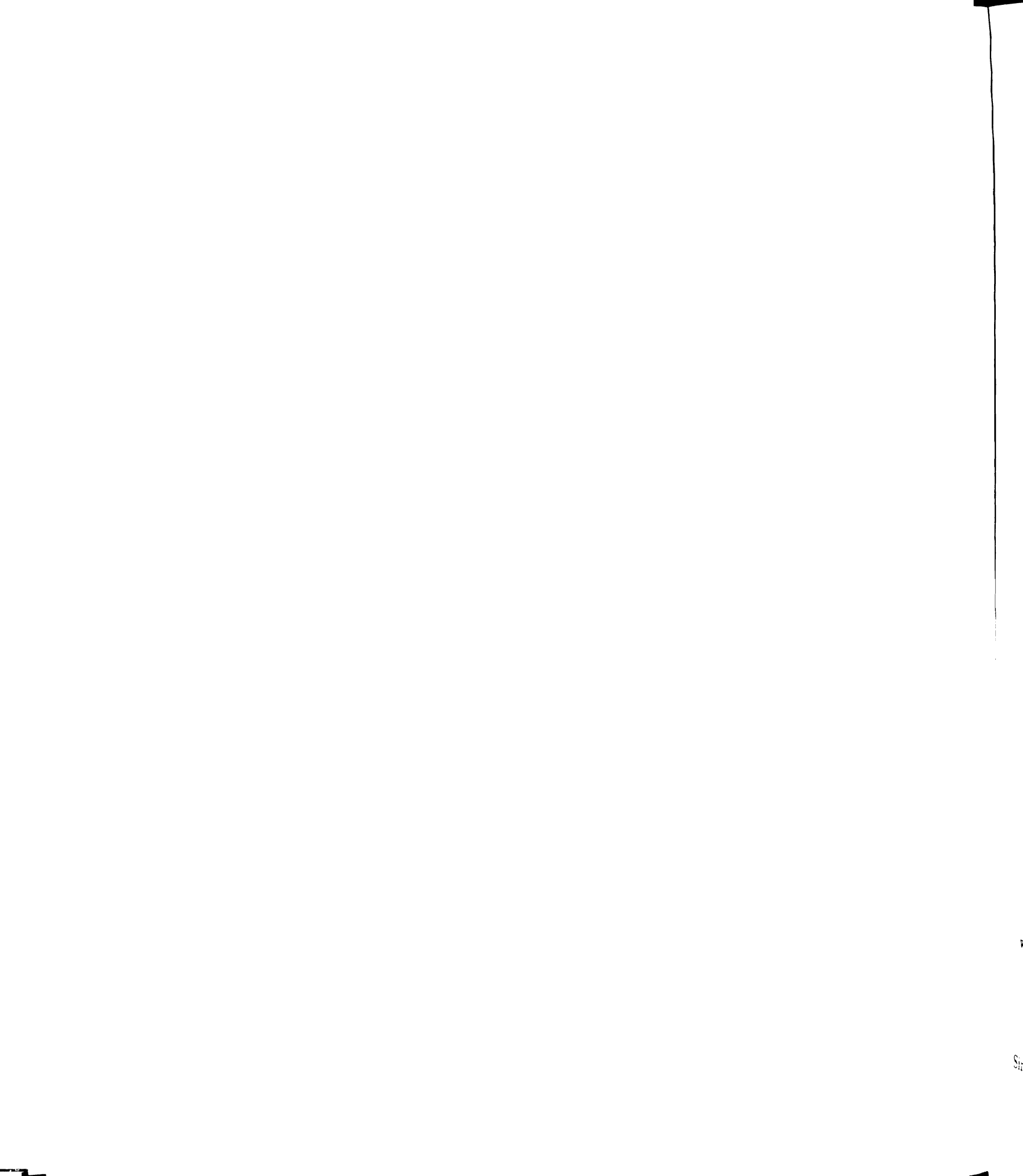
$$\dot{\bar{\Delta}} = \dot{\Delta} + \dot{\rho}_s \sum_{i=0}^n \gamma_i \quad (5.61)$$

Substituting Eqs.(2.20) and (5.56) to Eq.(5.21), we can write

$$m \ddot{x} = -K_s \mathbf{Y}^T \tilde{\phi} - m\lambda \dot{\tilde{x}} - \left(c + \frac{1}{2}m\dot{\bar{\Delta}}\right)\bar{e} + \mathbf{Y}_u^T \tilde{\phi}_u \quad (5.62)$$

From Eqs.(2.20) and (5.57), we can derive

$$\ddot{\tilde{d}} = \ddot{\mathbf{Y}}^T \tilde{\phi} + 2\dot{\mathbf{Y}}^T \dot{\tilde{\phi}} + \mathbf{Y}^T \ddot{\tilde{\phi}} \quad (5.63)$$



$$= \ddot{\mathbf{Y}}^T \tilde{\phi} + \dot{\Delta} \bar{e} + \bar{\Delta} \dot{e} \quad (5.64)$$

Using Eqs.(2.22), (5.48) and (5.50) we rewrite the dynamics in Eq.(5.62) to

$$M(t)\ddot{\bar{x}} + C(t)\dot{\bar{x}} + K(t)\bar{x} = u_1(t) \quad (5.65)$$

where

$$u_1(t) \triangleq -\mathbf{Y}_m^T \tilde{\phi} + \mathbf{Y}_u^T \tilde{\phi}_u \quad (5.66)$$

$$M(t) \triangleq m(1 - \bar{\Delta})$$

$$C(t) \triangleq c + \frac{1}{2}m\dot{\Delta} + m \left[ (1 - \bar{\Delta})\lambda - \dot{\Delta} \right]$$

$$K(t) \triangleq \left[ c + \frac{1}{2}m\dot{\Delta} - \dot{\Delta} \right] \lambda$$

Using similar procedures as in the previous section we can use the feedback configuration Figure D.1 in which  $H_1$  is the state space representation defined by the left-hand side terms in Eq.(5.65) having  $u_1$  shown in Eq.(5.66) as the input and  $\bar{e}$  as the output knowing Eq.(2.22). The system  $H_2$  has the input  $u_2 = \bar{e}$  and the output  $y_2 = \mathbf{Y}_m^T \tilde{\phi} - \mathbf{Y}_u^T \tilde{\phi}_u$ . As shown by lemma D.3 in Appendix D.2,  $H_2$  is passive for a sufficiently small  $\rho_s$ . Assuming the system  $H_1$  in the forward path remains strictly passive and satisfies the conditions in definition D.3, by theorem D.1 we can argue that

$$\bar{x}, \dot{\bar{x}}, \ddot{\bar{x}}, \bar{e} \rightarrow 0 \quad \text{as } t \rightarrow \infty$$

which implies

$$\begin{pmatrix} \bar{\mathbf{Y}}_m^T & -\mathbf{Y}_u^T \end{pmatrix} \begin{pmatrix} \tilde{\phi} \\ \tilde{\phi}_u \end{pmatrix} \rightarrow 0 \quad (5.67)$$

Since the regressor vector is PE,  $\tilde{\phi}, \tilde{\phi}_u \rightarrow 0$ . Therefore, all estimated parameters

converge to their true values and the rotor geometric center converges to the origin.

### 5.4.3 Actuator Gain Uncertainty

The controller uses  $\bar{K}_c \triangleq \rho_c + K_c$  where  $\rho_c$  is the amount of the uncertainty in the actuator gain. We assume that  $|\rho_c|_{max} < K_c$ . Due to the bias current excitation,  $\rho_c$  may vary at the frequency of the excitation. The feedback law in Eq.(5.24) becomes

$$I = -\frac{1}{\bar{K}_c} \left[ K_s \bar{x} + m\lambda \dot{\bar{x}} + (c + \frac{1}{2}m\dot{\Delta})\bar{e} + \mathbf{Y}_u^T \hat{\phi}_u \right] \quad (5.68)$$

and the adaptation laws shown in Eqs.(5.25) and (5.26) are still valid. Substituting Eq.(5.68) to Eq.(5.21) and using Eqs.(2.19), (2.20), (2.22) and (5.35) we obtain

$$M(t)\ddot{\bar{x}} + C(t)\dot{\bar{x}} + K(t)\bar{x} = u_1(t) \quad (5.69)$$

where

$$u_1(t) \triangleq -\mathbf{Y}_m^T \tilde{\phi} + \mathbf{Y}_u^T \tilde{\phi}_u + \frac{\rho_c}{\bar{K}_c} \mathbf{Y}_u^T \hat{\phi}_u \quad (5.70)$$

$$M(t) \triangleq m(1 - \Delta)$$

$$C(t) \triangleq \left(1 - \frac{\rho_c}{\bar{K}_c}\right) \left[ c + \frac{1}{2}m\dot{\Delta} + m\lambda \right] - m(\dot{\Delta} + \Delta\lambda)$$

$$K(t) \triangleq \lambda \left[ \left(1 - \frac{\rho_c}{\bar{K}_c}\right) \left( c + \frac{1}{2}m\dot{\Delta} \right) - m\dot{\Delta} \right] - \frac{\rho_c}{\bar{K}_c} K_s$$

Again, we can recast Eq.(5.69) such that the passivity argument can be used. In this case, the system  $H_2$  has the input  $u_2 = \bar{e}$  and the output  $y_2 = \mathbf{Y}_m^T \tilde{\phi} - \mathbf{Y}_u^T \tilde{\phi}_u - \frac{\rho_c}{\bar{K}_c} \mathbf{Y}_u^T \hat{\phi}_u$ . As before, we assume that  $H_1$  remains strictly passive. Knowing  $H_2$  is passive for a sufficiently small  $\rho_c$ , shown by lemma D.4 in Appendix D, by theorem D.1 we can argue that

$$\bar{x}, \dot{\bar{x}}, \ddot{\bar{x}}, \bar{e} \rightarrow 0 \quad \text{as } t \rightarrow \infty$$

which implies

$$\begin{pmatrix} \mathbf{Y}_m^T & -\mathbf{Y}_u^T \end{pmatrix} \begin{pmatrix} \phi - \hat{\phi} \\ \phi_u - (1 - \frac{\rho_c}{K_c})\hat{\phi}_u \end{pmatrix} \rightarrow 0 \quad (5.71)$$

Since the term  $\frac{\rho_c}{K_c}$  is function of time, the estimate parameter  $\hat{\phi}_u$  is perturbed. Since the harmonics of the unbalance are coupled with the first harmonics of the SRO, the estimate parameter  $\hat{\phi}$  is also perturbed and so is  $\tilde{d}$ . Knowing  $\bar{x} \rightarrow 0$ , from Eq.(2.19) we can conclude that uncertainty in actuator gain may cause a fluctuation in the rotor geometric center.

## 5.5 Simulation Results

Simulation results are presented in Figures 5.2, 5.3, and 5.4 to demonstrate the effectiveness of the SRUC-BCE when the plant parameters are known. As before, for simulation, we used the nonlinear plant model in Eqs.(2.1) and (2.2), parameters in Tables 4.1 and A.3, and the rotor angular speed of 1500 *rpm*. The SRO identification was performed for up to the second harmonic. In the simulation, we excite the bias currents at time interval  $5 < t < 35$  s using an amplitude of 0.2 A and frequency of 10 Hz. As seen in Figure 5.2, for  $t < 5$  s, the geometric center oscillates with constant amplitude due to sensor runout and unbalance. Without bias current excitation, Figure 5.3 indicates that for  $t < 5$  s the estimated parameters  $\hat{a}_1$ ,  $\hat{b}_1$ ,  $\hat{p}$ , and  $\hat{q}$  converge to arbitrary values while  $\hat{a}_0$ ,  $\hat{a}_2$ , and  $\hat{b}_2$  converge to the true values. After we turned on the bias current excitation, the parameters  $\hat{a}_1$ ,  $\hat{b}_1$ ,  $\hat{p}$ , and  $\hat{q}$  converge to the true values within 30 s, which results to the stabilization of the geometric center about the origin shown in Figure 5.2. During the excitation, in Figure 5.3 we can observe a diminishing slight fluctuation of the parameters  $\hat{a}_0$ ,  $\hat{a}_2$ , and  $\hat{b}_2$  about the true values. As shown in Figures 5.2 and 5.3, after all parameters have converge to the true values i.e.  $t > 35$ , turning off the excitation has a negligible effect. The geometric center

remains at the origin and the estimated parameters stay at the true values. Turning off the excitation at this time has an advantage of causing less effort in the power amplifier as indicated by Figure 5.4.

The effect of plant parameters uncertainties to the performance of the SRUC-BCE is illustrated in Figures 5.5 to 5.7 assuming that each parameter is over-estimated by 30 %. The strictly passivity condition discussed in section 5.4 is still satisfied knowing that the closed-loop system is still stable in the simulation results. As seen in Figure (5.5), the mass uncertainty does not affect the convergence of the geometric center to the origin. However, it should be noticed that parameters  $\hat{p}$  and  $\hat{q}$  do not converge to the true values. The simulation results in Figure 5.6 show that the convergence of parameters to the true values is not affected by the uncertainty in the magnetic stiffness. In Figure 5.7 we can observe that the uncertainty in the actuator gain cause a relatively small and steady fluctuation in the rotor geometric center. It can be seen that the parameters  $\hat{a}_1$ ,  $\hat{b}_1$ ,  $\hat{p}$ , and  $q$  do not converge to the true values while other estimate parameters converge to the true values.

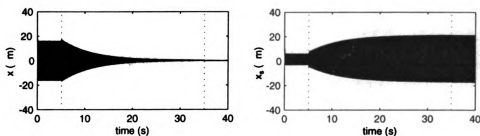


Figure 5.2. Geometric center  $x$  and sensor signal with runout  $x_s$

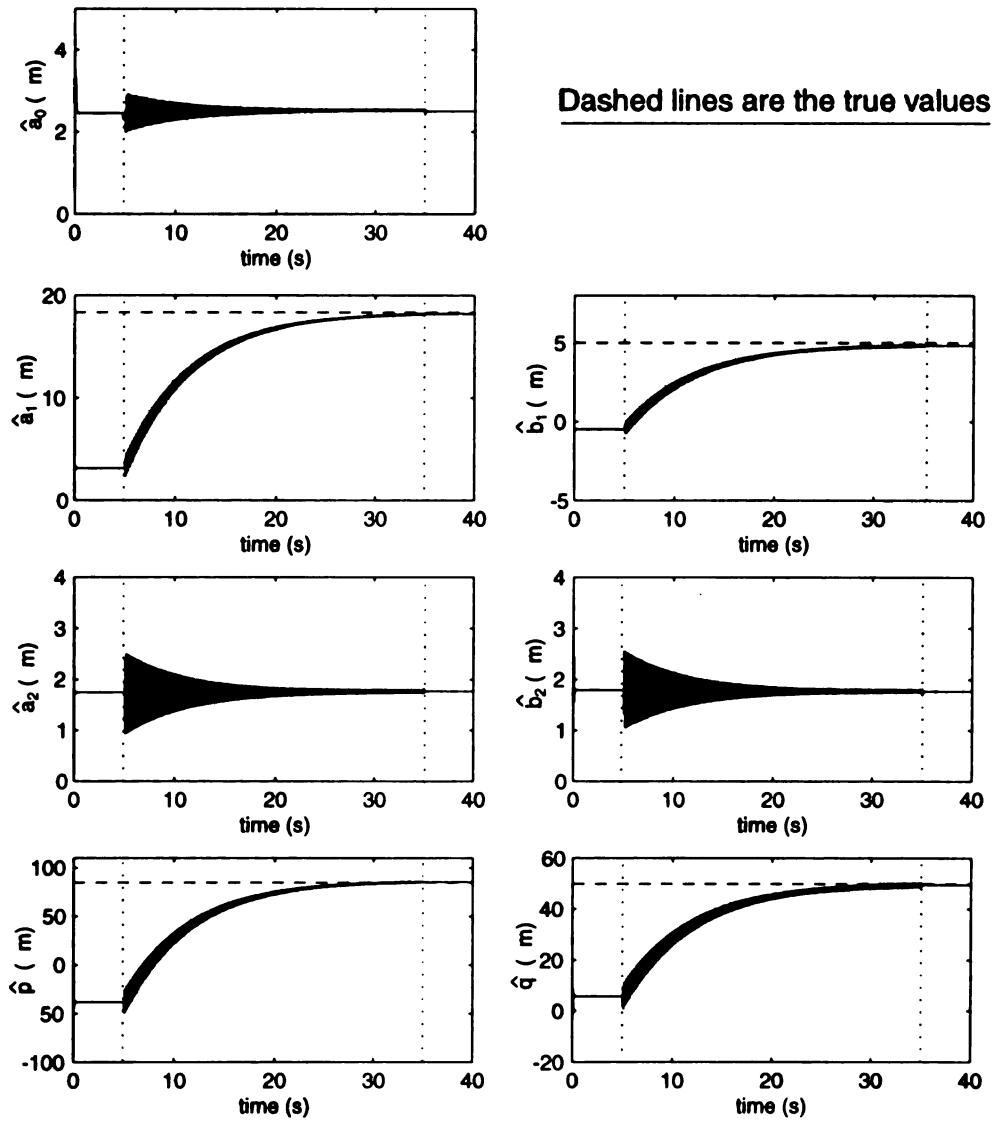


Figure 5.3. Estimated Fourier coefficients

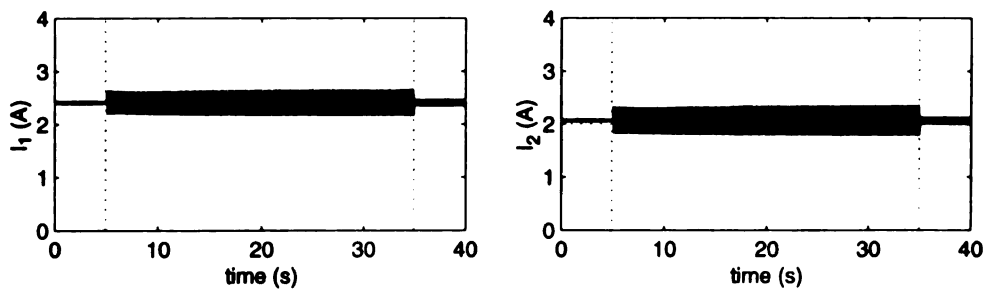


Figure 5.4. Top and bottom bias currents

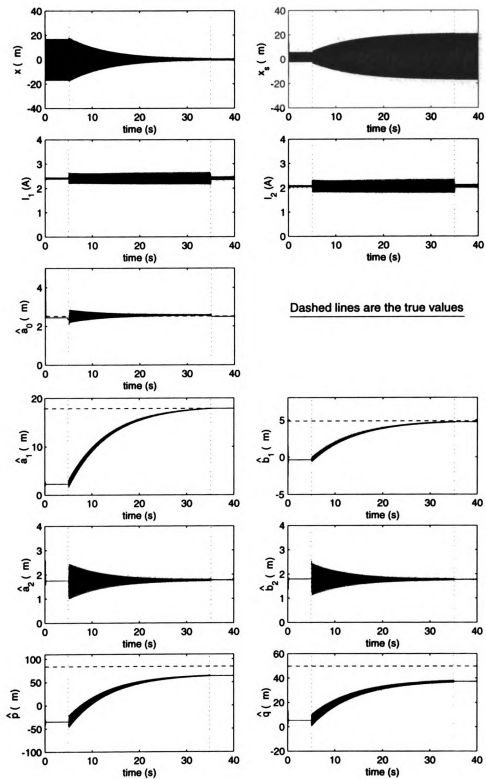


Figure 5.5. Effect of mass uncertainty to SRUC-BCE

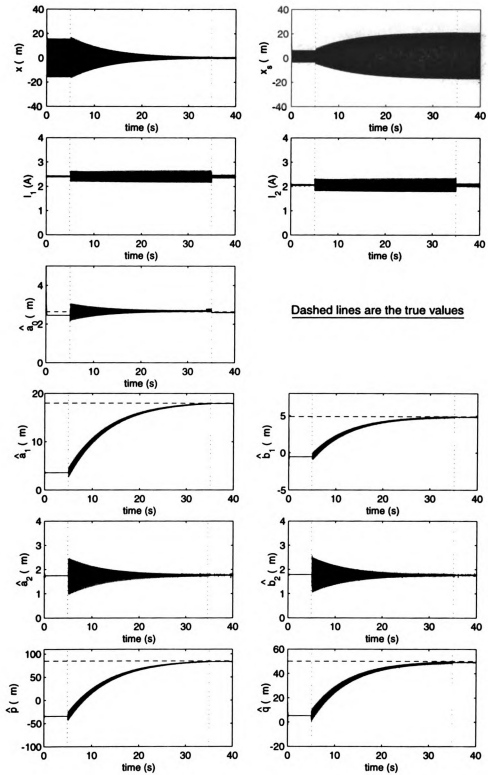


Figure 5.6. Effect of magnetic stiffness uncertainty to SRUC-BCE

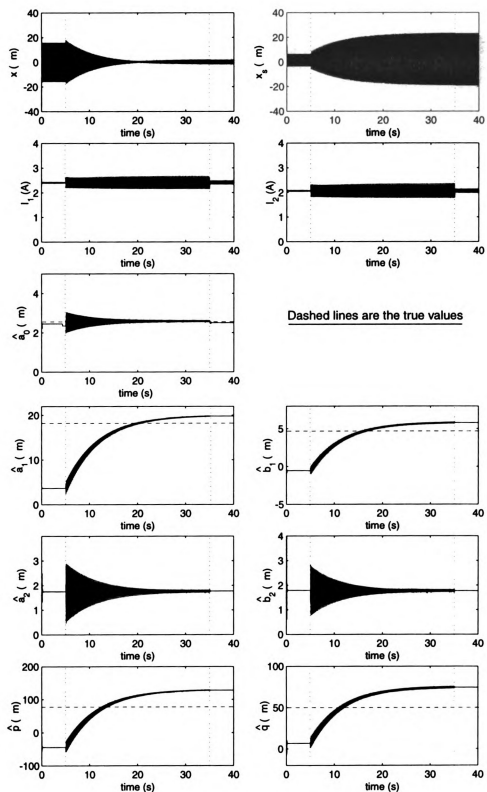


Figure 5.7. Effect of actuator gain uncertainty to SRUC-BCE

## 5.6 Simulation Studies of the Convergence Rate

To approximate the convergence rate of the SRUC via bias current excitation, we utilize the averaging method that has been useful in the ASRC system as seen in Chapter 3. The detail of derivation of the averaging method for the SRUC-BCE is provided in Appendix C.2. In simulation we used the parameters in Tables 4.1 and A.3, and the rotor angular speed of  $1500\text{ rpm}$ . As seen in Figures 5.8 and 5.9 it is clear that a higher amplitude of bias current excitation can result to faster convergence rate. The simulations shown in Figures 5.8 and 5.9 also indicate that the averaging method can accurately predict the convergence rate of the original system when the excitation frequency  $f_e$  is about one-half of the rotor frequency  $f$ . It was realized by simulations during our investigations that this occurrence is specific to the choice of adaptation gains.

We investigate the effect of the frequency of bias current excitation to the convergence rate using  $0 < f_e < f$ . It can be seen in Figure 5.10 that for the rotor frequency of  $f = 25\text{ Hz}$ , the convergence rate is highest when the frequency of the bias current excitation is about  $15\text{ Hz}$ . Therefore, there exists an optimum excitation frequency that can result to the fastest convergence rate. However, the analytical solution to the optimum frequency is still an open problem.

The effect of having more harmonics in the excitation can be investigated using the simulation results in Figure 5.11. It can be seen that having two harmonics in the excitation and imposing the same total excitation amplitude  $A = A_1 + A_2$  may decrease the convergence rate of the adaptation. Thus, excitation with one harmonic only, in this case, is preferable.

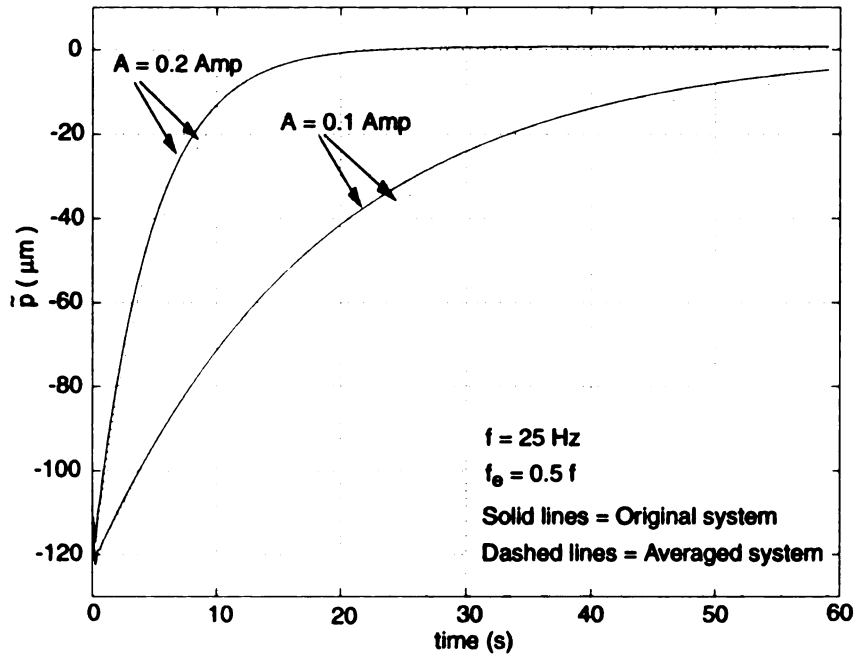


Figure 5.8. Effect of excitation amplitude;  $f_e = 0.5f$

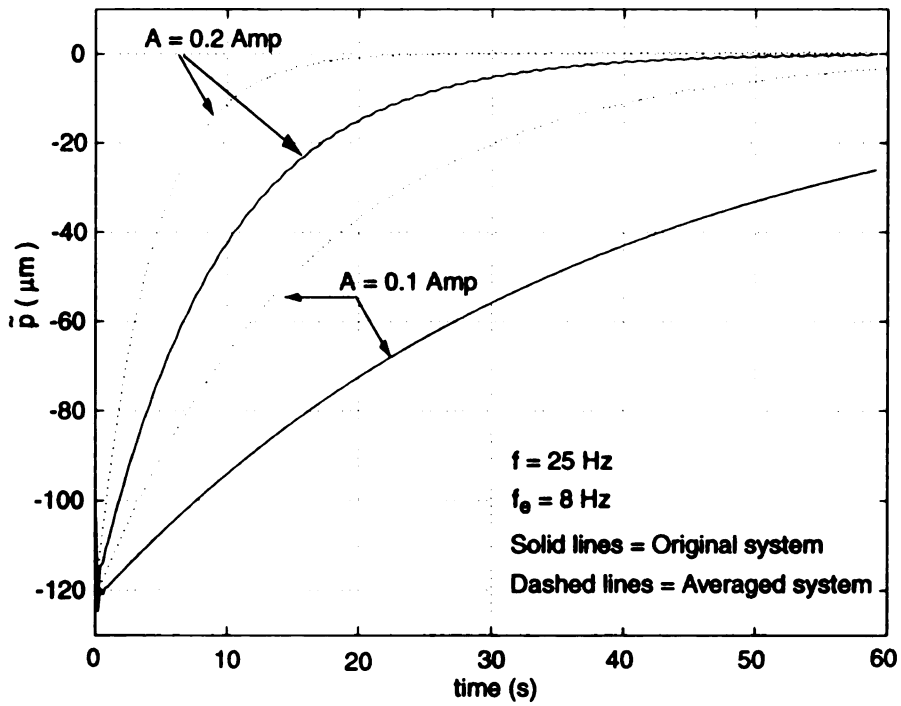


Figure 5.9. Effect of excitation amplitude when  $f_e \neq 0.5f$

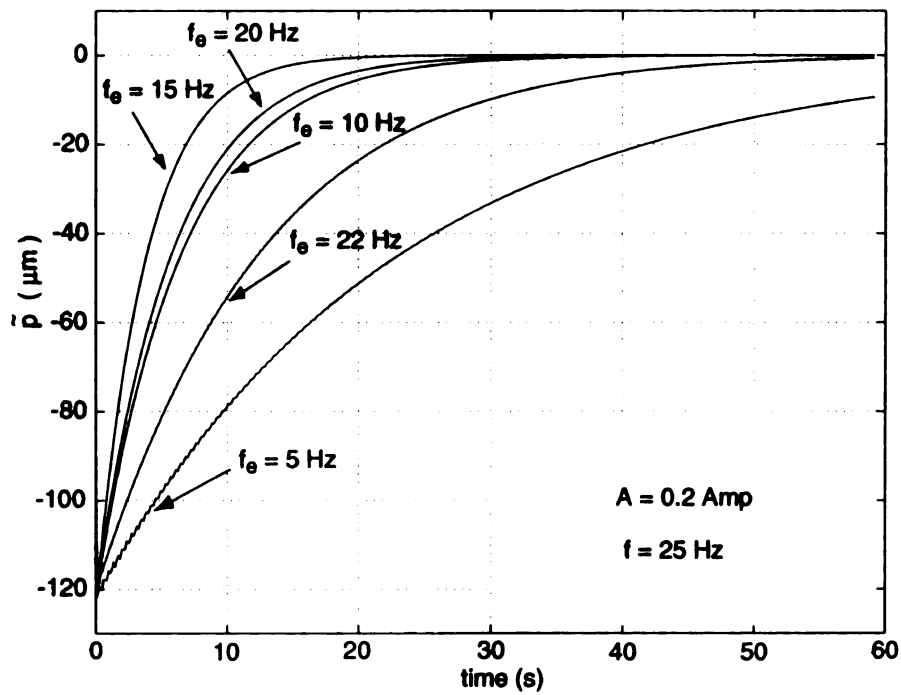


Figure 5.10. Effect of excitation frequency

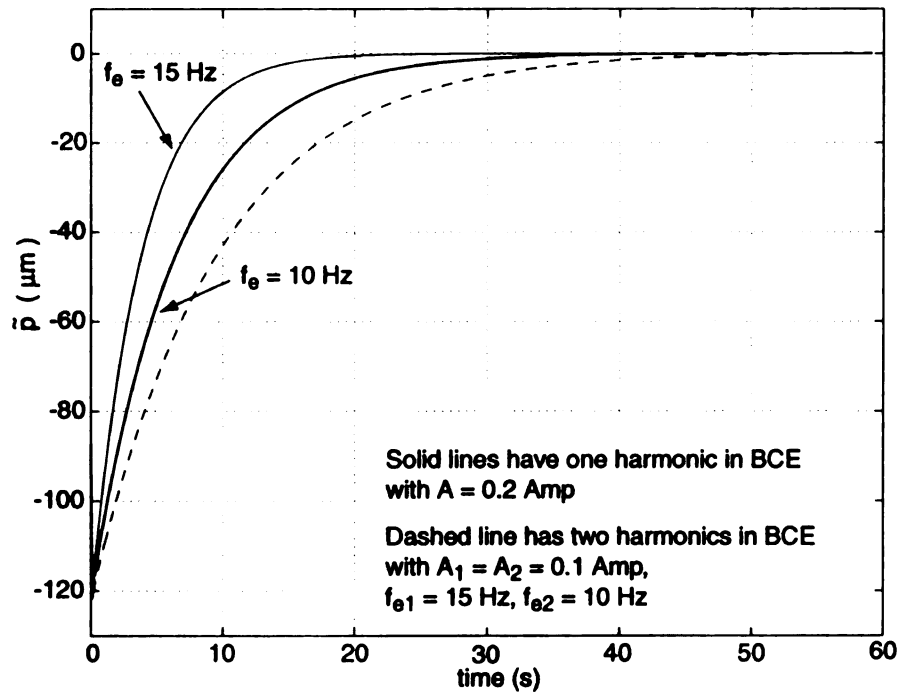


Figure 5.11. Effect the number of excitation harmonics

## 5.7 Experimental Procedure

We performed experiments to validate the efficacy of our algorithm on synchronous runout and unbalance compensation. The schematic of our test rig is shown in Figure A.1. We used a steel rotor, 43.2 cm in length and 2.5 cm in diameter, with a balance disk for adding trial masses for unbalance. As shown in Appendix A.2, the rotor was quite rigid with the first flexible mode frequency at approximately 438 Hz, which was six times higher than the bandwidth of the closed-loop system. At one end, the rotor was connected to an absolute encoder using a bellows-type torsionally rigid coupling. Without introducing significant radial forces on the rotor, the coupling accommodates lateral misalignments. The encoder output was used in generating the feed-forward terms in our adaptive algorithm. At the other end, our rotor was connected to a motor via a flexible rubber coupling. An optical speed sensor was used to provide feedback to an analog controller unit to maintain the speed of the rotor at a constant desired value.

The rotor was levitated using two bearings, A and B. Among them, both axes of bearing B were controlled using analog PD controllers shown in Appendix A.3. Although both axes of bearing A were computer-controlled, unbalance and runout was compensated in one of the axes. A PD controller was used to control the rotor along the other axis. The currents in the electromagnets of both bearings were driven by switching power amplifiers, operating with a bandwidth of 1.6 KHz. The physical parameters and operating conditions of bearing A are provided in Table A.3. The rotor mass enumerated in this table pertains to that of the whole rotor. We programmed our adaptive algorithm for synchronous runout and unbalance compensation in Matlab/Simulink<sup>TM</sup> environment and downloaded it to a Digital Signal Processor (DSP) board, manufactured by dSPACE<sup>TM</sup>. The sampling rate of the board was set at 13 KHz for on-line identification and control. A separate DSP board

sampling at 5 KHz, along with suitable analog circuits, was used for manual identification of runout. The manually identified runout was used to determine the position of the rotor geometric center from the sensor signal.

Before implementation of our algorithm, we levitated the rotor using a PD controller and manually identified runout following the procedures outlined in Section 2.5. Although the first harmonic of runout was significant, higher harmonics of runout were negligible. On the basis of these results, we set  $n = 1$  in our algorithm for estimation of runout.

We performed experiments with the balance disk at two different locations, shown in Figure A.1 . For each location, we implemented our algorithm three times. In the first experiment, Expt. 1, we did not introduce any unbalance but estimated the initial unbalance of the rotor. In line with our discussion in section 2.6, we added a trial mass in the second experiment, Expt. 2, and re-estimated unbalance. The third experiment, Expt. 3, was performed by introducing the trial mass at a different phase angle. Although a trial mass was added to the balance disk, unbalance was compensated only in bearing A. Since bearing B did not have unbalance compensation, we conducted two sets of experiments with the balance disk at two different locations to gain a high level of confidence in our results.

We performed our experiments at constant rotor speed of 1500 rpm (25 Hz). We used the control law in Eq.(5.24) and the adaptation laws in Eqs.(5.25) and (5.26) with the following choice of gains

$$\lambda = 400 \text{ s}^{-1}, \quad c = 1200 \text{ kg/s}, \quad \Gamma = \text{diag} (1.4, 3, 3, 3, 3) \times 10^{-7} \text{ m/N}$$

$$\Gamma_{\mathbf{u}} = \text{diag} (3, 3) \times 10^{-5} \text{ m/N}$$

The derivative term  $\dot{\hat{\mathbf{x}}}$  in the control law was numerically computed using the transfer function  $2500 s/(s + 2500)$ . This eliminates potential problems arising from infiltration of wideband noise into the sensor signal. During adaptation, the top bias

current was excited using  $\delta_1 = 0.2 \sin(20\pi t)$  Amperes. The excitation frequency was therefore less than half of the rotor frequency. After estimated parameters reached steady state, adaptation and bias current excitation were both discontinued.

In our algorithm, bias currents are excited concurrently with estimation. This eliminates drift in the estimated Fourier coefficients of unbalance and the first harmonics of runout in the absence of persistent excitation. Compared to standard implementation, our algorithm requires an extra D/A channel for every axis of implementation since both coils of each axis are excited independently.

## 5.8 Experimental Results

We first performed experiments with the balance disk located at rotor midspan. The results are provided in Tables 5.1 and 5.2. The first column of data in Tables 5.1 and 5.2 (Expt. 0) pertains to the manually identified values of sensor runout. This data includes the DC component and the first harmonics of runout only since second and higher harmonics were found to be negligible. The phase of the first harmonic was set to zero through encoder calibration. The second column of data (Expt. 1) corresponds to our experiment performed without a trial mass. This data includes the DC component and first harmonics of runout, and the harmonics of initial unbalance of the rotor.

The two columns, labeled Expt. 2 and Expts. 1, 2 in Table 5.1, of data pertain to our experiment with the addition of a trial mass of eccentricity  $\epsilon_T = 91.1 \mu m$ . The eccentricity value was computed from the mass of the trial weight, which was 10 gms, the radial distance of the trial weight, 4.45 cms, and the total mass of the rotor, which was 4.87 kgs, in the following manner:  $\epsilon_T = \{0.01/(4.87 + 0.01)\} \times 0.04445 = 91.1 \mu m$ . The phase of the trial weight was  $\theta_T = -56^\circ$ .

The Expt. 2 column provides experimentally obtained values of runout and unbal-

ance. The column marked Expt. 1, 2 provides computed values of unbalance solely due to the trial mass. The computed values were obtained in line with our discussion in section 2.6, as follows

$$\epsilon_T \angle \theta_T = (\epsilon_R \angle \theta_R - \epsilon_U \angle \theta_U) = (86.7 \angle -61.3^\circ - 12.9 \angle -91.8^\circ) = 75.9 \angle -56.4^\circ$$

The last two columns of data in Table 5.2 pertain to experimental results obtained with the same trial mass, located at the same radial distance, but at the new phase angle  $\theta_T = -146^\circ$ . Among these two columns, the left column provides Fourier coefficients of runout and unbalance obtained through experiments (Expt. 3). The right column provides computed values of unbalance solely due to the trial mass. This data was obtained as follows

$$\epsilon_T \angle \theta_T = (\epsilon_R \angle \theta_R - \epsilon_U \angle \theta_U) = (82.1 \angle -142.9^\circ - 12.9 \angle -91.8^\circ) = 74.7 \angle -150.6^\circ$$

The time history of the rotor geometric center position,  $x$ , and sensor signal,  $x_s$ , are provided in Figure 5.12 for one of the experiments, Expt. 2. The geometric center position was evaluated from the sensor signal through cancellation of manually identified runout. The time scale in Figure 5.12 is divided into three distinct regions: (a)  $t \leq 0$ , where runout and unbalance were not compensated, (b)  $0 \leq t \leq 300$ , where runout and unbalance were adaptively estimated and compensated, and (c)  $t \geq 300$ , where runout and unbalance were completely compensated and bias current excitation terminated.

Due to the relatively long duration of the experiment, we acquired data over the sub-intervals  $-0.2 \leq t \leq 0.3$ ,  $120.0 \leq t \leq 120.5$ , and  $299.6 \leq t \leq 300.2$ . The time trajectories of the estimated Fourier coefficients of runout and unbalance are shown in Figure 5.13, with final values of the coefficients shown with dashed lines. The sensor runout coefficients show larger fluctuations than those of unbalance. This can be primarily attributed to the difference in scale of the plots.

Table 5.1. Experimental results with the balance disk located at the rotor midspan:  
part (a)

Sensor runout and unbalance	manual SRO identification	initial unbalance	initial unbalance plus trial weight $\epsilon_T = 91.1$ $\theta_T = -56$	estimation of trial weight $\epsilon_T = 91.1$ $\theta_T = -56$
	Expt. 0	Expt. 1	Expt. 2	Expts. 1, 2
$\hat{a}_0$	0.0	-0.5	-0.1	-
$\hat{a}_1$	40.0	38.5	39.0	-
$\hat{b}_1$	0.0	-0.6	0.2	-
Mag., $A_1$	40.0	38.5	39.0	-
Phase, $\theta_1$	0.0	1.0	0.3	-
$\hat{p}$	-	12.9	76.1	-
$\hat{q}$	-	-0.4	41.6	-
Mag., $\epsilon_u$	-	12.9	86.7	75.9
Phase, $\theta_u$	-	-91.8	-61.3	-56.4

Note: units of measurement are  $\mu m$  and degrees

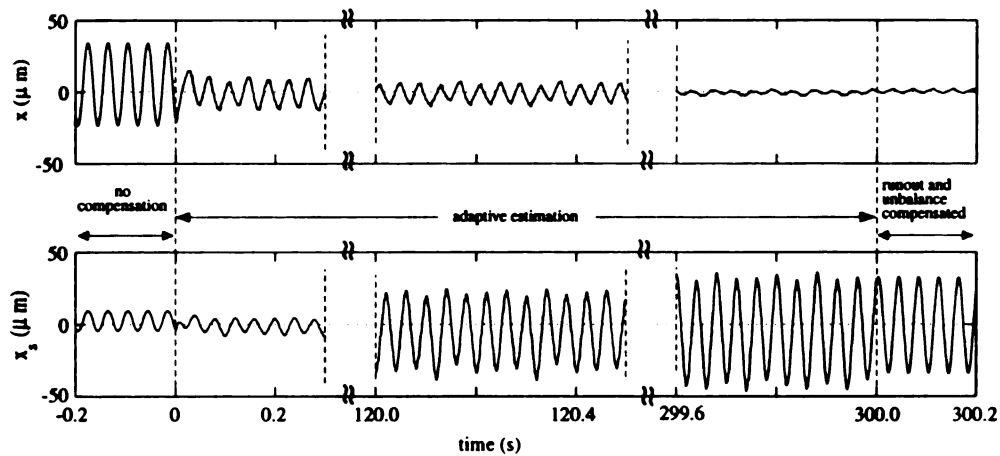


Figure 5.12. Time history of geometric center  $x$  and position sensor signal  $x_s$

Table 5.2. Experimental results with the balance disk located at the rotor midspan:  
part (b)

Sensor runout and unbalance	manual SRO identification Expt. 0	initial unbalance Expt. 1	initial unbalance plus trial weight $\epsilon_T = 91.1$ $\theta_T = -146$ Expt. 3	estimation of trial weight $\epsilon_T = 91.1$ $\theta_T = -146$ Expts. 1, 3
$\hat{a}_0$	0.0	-0.5	-4.4	-
$\hat{a}_1$	40.0	38.5	37.2	-
$\hat{b}_1$	0.0	-0.6	-0.3	-
Mag., $A_1$	40.0	38.5	37.2	-
Phase, $\theta_1$	0.0	1.0	-0.4	-
$\hat{p}$	-	12.9	49.5	-
$\hat{q}$	-	-0.4	-65.5	-
Mag., $\epsilon_u$	-	12.9	82.1	74.7
Phase, $\theta_u$	-	-91.8	-142.9	-150.6

Note: units of measurement are  $\mu m$  and degrees

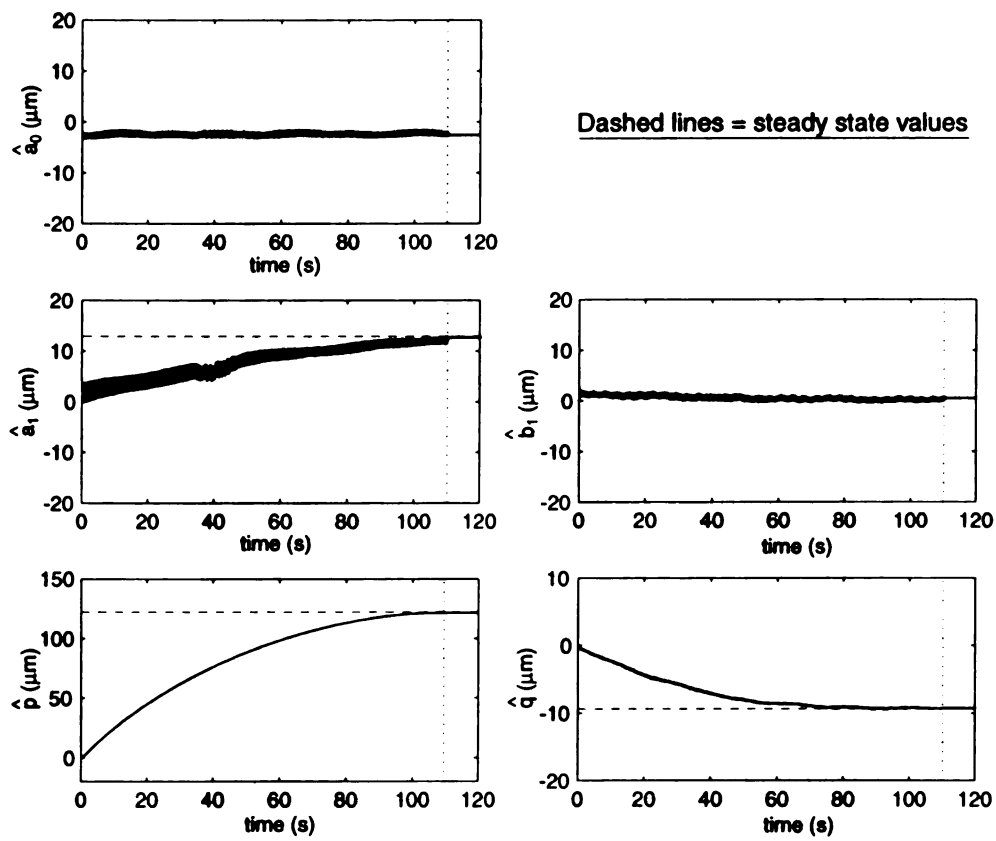


Figure 5.13. Time trace of estimated Fourier coefficients for Expt. 2 in Table 5.1

## 5.9 Interpretation of Experimental Results

First consider the Fourier coefficients of sensor runout presented in Tables 5.1 and 5.2. These values, identified by our algorithm, are very similar for Expts. 1, 2, and 3, performed with varying degrees of unbalance. Furthermore, the identified coefficients closely match the manually identified values of runout, Expt. 0. We can therefore claim that sensor runout has been correctly identified.

Next, investigate the estimated magnitude and phase of unbalance due to the trial mass alone, for the two cases in Tables 5.1 and 5.2. The estimated magnitudes,  $75.9 \mu m$  and  $74.7 \mu m$ , are similar and therefore consistent, and their respective phases,  $-56.4^\circ$  and  $-150.6^\circ$ , compare very well with the true values,  $-56^\circ$  and  $-146^\circ$ , respectively. The average value of the estimated magnitudes of unbalance,  $75.3 \mu m$ , is approximately 82% of the trial mass eccentricity of  $91.1 \mu m$ , added at rotor midspan. Other than this percentage factor, which will be discussed later, the above data indicates that our algorithm determines the phase of unbalance accurately and provides consistent estimates for eccentricity over repeated trials.

Now consider the plot of the rotor geometric center position,  $x$ , in Figure 5.12. Although this plot specifically pertains to Expt. 2, it is representative of the general behavior of the rotor geometric center with our algorithm. It can be seen from Figure 5.12 that the geometric center initially fluctuates about a nonzero mean value but this fluctuation is virtually eliminated with our algorithm. The stabilization of the rotor geometric center to the origin convinces us that both mass unbalance and sensor runout have been correctly estimated and compensated.

A second set of experiments were performed with the balance disk closer to Bearing B, as shown in Figure A.1. The results of these experiments, provided in Tables 5.3 and 5.4, are very consistent with the results in Tables 5.1 and 5.2. Specifically, the estimated values of sensor runout are very similar to the values in Table 5.1 and

5.2, and closely match the manually identified values. The magnitude of estimated unbalance is consistent over repeated trials and the phase of unbalance closely match the phase of the trial mass for both experiments. The plots of the rotor geometric center, not shown here due to their similarity with the plot in Figure 5.12, also indicate geometric center stabilization.

The ratio between the average magnitude of estimated unbalance and trial mass eccentricity is 0.51 for the experimental results in Table 3. Although this value is less than the 0.82 ratio obtained with the balance disk at rotor midspan, as one would expect, both values are higher than expected. An explanation of the higher values would require further analysis that takes into consideration: (a) characteristics of the support provided by Bearing B under PD control, in the absence of unbalance and runout compensation, (b) performance of our adaptive algorithm, formally developed for a single degree-of-freedom rotor with collocated sensor and actuator, in our experimental test-rig, and (c) additional stiffness and unbalance introduced by the couplers at the two ends of the rotor. It will however not be worthwhile pursuing such analysis since our adaptive algorithm will have to be extended to a complete rotor model before it can be implemented in any industrial rig. Our experimental results amply demonstrate the basic feasibility of our algorithm but significant work remains to be done before it can be adopted by commercial vendors.

We conclude this section with our comments on the time taken for synchronous disturbance compensation. It can be seen from Figures 5.2 and 5.12 that compensation in simulation requires a shorter time than compensation in experiments. This can be attributed to the fact that only one of the bearings in our experimental setup was compensating the disturbances. The other bearing, in the absence of unbalance and runout compensation, acted as a source of additional periodic disturbances. We expect the time to reduce significantly when both bearings compensate for disturbances, and amplitude and frequency of bias current excitation are chosen optimally.

The time taken for compensation in our experiments, nevertheless, should not be construed as significant. This time will be required during rotor spinup only. During steady state operation, adaptation and bias current excitation will be implemented for a few seconds periodically to account for possible drift in runout and unbalance. Depending upon the type of application, periodic implementation may occur few times every hour to once every few hours.

Table 5.3. Experimental results with the balance disk located closer to bearing B: part (a)

Sensor runout and unbalance	manual SRO identification Expt. 0	initial unbalance Expt. 1	initial unbalance plus trial weight $\epsilon_T = 91.1$ $\theta_T = -56$ Expt. 2	estimation of trial weight $\epsilon_T = 91.1$ $\theta_T = -50$ Expts. 1, 2
$\hat{a}_0$	0.0	-0.2	-1.3	-
$\hat{a}_1$	40.0	40.0	40.0	-
$\hat{b}_1$	0.0	-0.7	1.5	-
Mag., $A_1$	40.0	40.0	40.0	-
Phase, $\theta_1$	0.0	-1.0	2.1	-
$\hat{p}$	-	10.9	45.0	-
$\hat{q}$	-	4.1	36.8	-
Mag., $\epsilon_u$	-	11.6	58.2	47.3
Phase, $\theta_u$	-	-69.4	-50.7	-46.2

Note: units of measurement are  $\mu m$  and degrees

Table 5.4. Experimental results with the balance disk located closer to bearing B: part (b)

Sensor runout and unbalance	manual SRO identification Expt. 0	initial unbalance Expt. 1	initial unbalance plus trial weight $\epsilon_T = 91.1$ $\theta_T = -146$ Expt. 3	estimation of trial weight $\epsilon_T = 91.1$ $\theta_T = 40$ Expts. 1, 3
$\hat{a}_0$	0.0	-0.2	-1.1	-
$\hat{a}_1$	40.0	40.0	38.6	-
$\hat{b}_1$	0.0	-0.7	0.9	-
Mag., $A_1$	40.0	40.0	38.7	-
Phase, $\theta_1$	0.0	-1.0	1.4	-
$\hat{p}$	-	10.9	-21.2	-
$\hat{q}$	-	4.1	36.5	-
Mag., $\epsilon_u$	-	11.6	42.2	45.6
Phase, $\theta_u$	-	-69.4	30.2	44.7

Note: units of measurement are  $\mu m$  and degrees

## 5.10 Summary and Remarks

A new adaptive algorithm has been designed to identify the harmonic components of sensor runout and unbalance at constant rotor speed. The algorithm relies on persistency of excitation generated by methodical bias current excitation. The bias current excitation amplitude is small and carried out in a manner that does not alter the equilibrium condition of the rotor. The algorithm enables us to stabilize the rotor geometric center to the origin in the presence of simultaneous sensor runout and unbalance. After the geometric center has been stabilized to the origin, one may stop the bias current excitation without causing problems to the closed-loop system. If the harmonic components of the disturbances drift, the bias current excitation procedure may be invoked for a brief duration to identify the new values of the harmonics. Depending upon the application, bias current excitation may be invoked few times an hour to once every few hours. The efficacy of our algorithm was demonstrated both through simulations as well as experiments.

The effect of plant parameter uncertainties on the performance of the algorithm has been investigated. In general, as shown by simulations, the algorithm can withstand to small uncertainties in the plant parameters. It was observed that the strict passivity condition of  $H_1$  should be evaluated case by case. The passivity of  $H_1$  is important for ensuring closed-loop system stability and convergence of estimated parameters to their true values. Further investigation is needed to show the interaction between the nominal plant parameters and choice of gains in the algorithm to meet the strict passivity condition in  $H_1$ . Furthermore, it is realized that more work should be done to reduce the effect of the uncertainty in the actuator gain.

In Chapter 3, we had shown that the averaging method was a good analytical tool to predict the convergence rate of parameters in ASRC. Unfortunately, this method is not directly applicable to the SRUC algorithm and further research is required to

predict convergence rates of parameters. Our simulations show that the optimum adaptation speed can be achieved when the frequency of excitation is between 50 to 75 % of the rotor frequency. However, further studies are needed to understand the effect of nominal plant parameters and controller gains on the optimum frequency of excitation. Our simulation results also show that for a fixed total amplitude of bias current excitation, faster convergence is achieved with one harmonic of excitation rather than multiple harmonics. This should however be verified analytically.

# CHAPTER 6

## Extension to MIMO Systems

### 6.1 Introduction

In this section we investigate the effectiveness of ASRC and SRUC-BCE algorithms in MIMO magnetic bearing systems. By assuming the gyroscopic effect to the system to be negligible, we decouple the 4-DOF MIMO system into two identical 2-DOF systems. We then analyze the 2-DOF dynamics of the rotor being controlled by the MIMO versions of the adaptive algorithms. The stability analysis of the 2-DOF systems is provided. The convergence of estimated parameters is studied through simulations.

### 6.2 MIMO Model of Magnetic Bearing with Rigid Rotor

A free body diagram of the rigid rotor is shown in Figure 6.1. The forces  $F_j$  for  $j = 1, \dots, 4$  are provided by the two radial bearings, which are at distances  $L$  from the rotor center of geometric.  $O - XYZ$  is the inertial frame fixed in the space,  $x$ ,  $y$  are the displacements of the center of geometric along the  $X$  and  $Y$  directions. Both  $X$  and  $Y$  axes are inclined at  $45^\circ$  with the horizontal. The rotor is assumed

constrained along the  $Z$  directions. The  $x$  and  $y$  displacements are given with respect to the inertial frame. It is assumed in this analysis that the nominal gaps and forces in the bearings are in the same radial plane; thus, the effects of non-collocation are ignored.  $\theta$  and  $\psi$  are angles of rotation about the  $X$  and the  $Y$  axis respectively. These angles are assumed to be small. We also assume that the center of mass does not coincide with the geometric center. However, the axis of rotation is still aligned with the rotor's major principal axis; therefore, the dynamic unbalance is neglected and only static unbalance is assumed. In Figure 6.1, the static unbalance  $\varepsilon$  is the

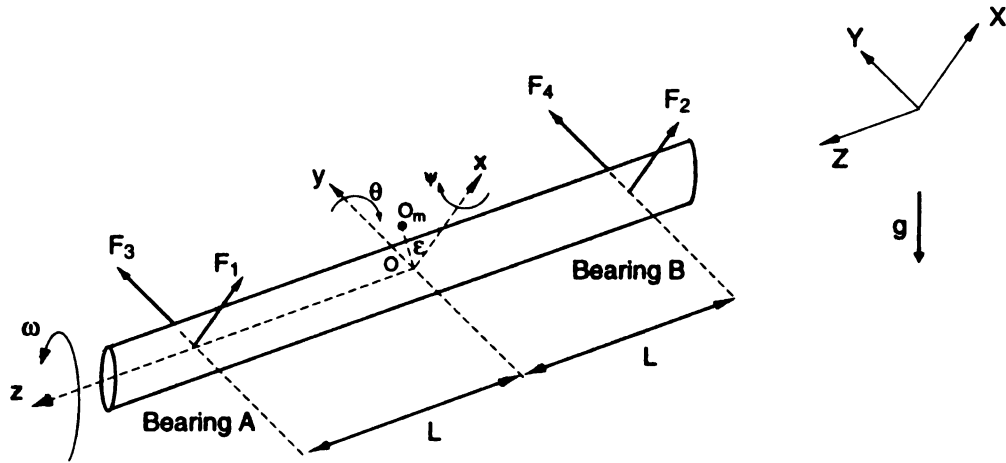


Figure 6.1. Freebody diagram of a magnetically levitated rigid-rotor

distance between the rotor's geometric center  $O$  and its center of mass  $O_m$  on the  $x$ - $y$  plane. The resulting dynamics equations, in terms of  $x$ ,  $y$ ,  $\theta$ , and  $\psi$ , are given by

$$m\ddot{x} = F_1 + F_2 + m\omega^2\varepsilon \cos(\omega t + \theta_u) - mg/\sqrt{2} \quad (6.1a)$$

$$m\ddot{y} = F_3 + F_4 + m\omega^2\varepsilon \sin(\omega t + \theta_u) - mg/\sqrt{2} \quad (6.1b)$$

$$I_T\ddot{\theta} = (F_1 - F_2)L - I_a\omega\dot{\psi} \quad (6.1c)$$

$$I_T \ddot{\psi} = (F_3 - F_4)L - I_a \omega \dot{\theta} \quad (6.1d)$$

where  $m$  is the total mass of the rotor,  $I_a$  and  $I_T$  are the axial and transverse mass moment of inertias, and the forces

$$F_j = k \left[ \left( \frac{i_{10j} + i_j}{l - x_j} \right)^2 - \left( \frac{i_{20j} - i_j}{l + x_j} \right)^2 \right] \quad j = 1, \dots, 4 \quad (6.2)$$

Linearization of the external forces about  $x_j = 0$  and  $i_j = 0$  gives

$$F_j = F_{0j} + K_{cj}i_j + K_{sj}x_j \quad (6.3)$$

Since the bearings are identical and symmetrical, we may write  $i_{10j} = i_{10}$  and  $i_{20j} = i_{20}$ . Also, we can obtain  $K_{cj} = K_c$  and  $K_{sj} = K_s$  that are defined by Eqs.(2.6) and (2.5). Assuming the static unbalance  $\varepsilon$  is small compared to  $L$ , the following relations can be obtained from geometry:

$$x_1 = x + L\theta, \quad x_2 = x - L\theta, \quad x_3 = y + L\psi, \quad x_4 = y - L\psi \quad (6.4)$$

and we can write the equation of motion about  $x = 0$ ,  $y = 0$ ,  $\theta = 0$ , and  $\psi = 0$  as

$$m \begin{Bmatrix} \ddot{x}_1 \\ \ddot{x}_2 \\ \ddot{x}_3 \\ \ddot{x}_4 \end{Bmatrix} = \underline{\mathbf{K}}_c \begin{Bmatrix} i_1 \\ i_2 \\ i_3 \\ i_4 \end{Bmatrix} + \underline{\mathbf{K}}_s \begin{Bmatrix} x_1 \\ x_2 \\ x_3 \\ x_4 \end{Bmatrix} + \underline{\mathbf{G}} \begin{Bmatrix} \dot{x}_1 \\ \dot{x}_2 \\ \dot{x}_3 \\ \dot{x}_4 \end{Bmatrix} + \mathbf{f}_u \quad (6.5)$$

where

$$\underline{\mathbf{K}}_c \triangleq \begin{bmatrix} \underline{K}_c & \mathbf{0} \\ \mathbf{0} & \underline{K}_c \end{bmatrix}, \quad \text{and} \quad \underline{\mathbf{K}}_s \triangleq \begin{bmatrix} K_c(1 + \frac{mL^2}{I_t}) & -K_c(1 - \frac{mL^2}{I_T}) \\ -K_c(1 - \frac{mL^2}{I_T}) & K_c(1 + \frac{mL^2}{I_T}) \end{bmatrix} \quad (6.6)$$

are the open loop stiffness matrices,

$$\underline{\mathbf{K}}_s \triangleq \begin{bmatrix} \underline{K}_s & \mathbf{0} \\ \mathbf{0} & \underline{K}_s \end{bmatrix}, \quad \text{and} \quad \underline{K}_s \triangleq \begin{bmatrix} K_s(1 + \frac{mL^2}{I_T}) & -K_s(1 - \frac{mL^2}{I_T}) \\ -K_s(1 - \frac{mL^2}{I_T}) & K_s(1 + \frac{mL^2}{I_T}) \end{bmatrix} \quad (6.7)$$

are the actuator gain matrices,

$$\underline{\mathbf{G}} \triangleq \begin{bmatrix} 0 & 0 & -\frac{I_a\omega}{2I_T} & \frac{I_a\omega}{2I_T} \\ 0 & 0 & \frac{I_a\omega}{2I_T} & -\frac{I_a\omega}{2I_T} \\ \frac{I_a\omega}{2I_T} & -\frac{I_a\omega}{2I_T} & 0 & 0 \\ -\frac{I_a\omega}{2I_T} & \frac{I_a\omega}{2I_T} & 0 & 0 \end{bmatrix} \quad (6.8)$$

is the gyroscopic matrix, and

$$\mathbf{f}_u = m\omega^2\epsilon \begin{Bmatrix} \cos(\omega t + \phi_u) \\ \cos(\omega t + \phi_u) \\ \sin(\omega t + \phi_u) \\ \sin(\omega t + \phi_u) \end{Bmatrix} \quad (6.9)$$

is the unbalance force vector.

In practice, the gyroscopic effect is likely to be very small. It becomes important only when the rotor spins at extremely high speed, which is not the interest of our study. As the results, the coupled 4-DOF AMB system model can be decoupled as two 2-DOF system models. Let  $\mathbf{x} = [x_1 \ x_2]^T = [x_A \ x_B]^T$ ,  $\mathbf{I} = [i_1 \ i_2]^T = [i_A \ i_B]^T$ , then the equation of motion on one plane can be represented by

$$m\ddot{\mathbf{x}} \triangleq \underline{K}_c\mathbf{I} + \underline{K}_s\mathbf{x} + \underline{\mathbf{Y}}_u^T\phi_u \quad (6.10)$$

where

$$\underline{\mathbf{Y}}_u^T \triangleq m\omega^2 \begin{bmatrix} \sin(\omega t) & \cos(\omega t) \\ \sin(\omega t) & \cos(\omega t) \end{bmatrix} \quad (6.11)$$

It should be noticed that the unbalance disturbance,  $\phi_u$ , affects both axis at equal magnitude. Furthermore, the SRO disturbance vector is now represented by

$$\mathbf{d} \triangleq (d_A \quad d_B)^T \quad (6.12)$$

$$d_j \triangleq a_{0j} + \sum_{i=1}^n a_{ij} \sin(i\omega t) + b_{ij} \cos(i\omega t) \quad j = A, B \quad (6.13)$$

Using  $\mathbf{Y}^T$ , defined in Eqs.(2.13), we can also write

$$\mathbf{d} = \underline{\mathbf{Y}}^T \Phi, \quad \mathbf{d} \in \mathfrak{R}^2 \quad (6.14)$$

where

$$\underline{\mathbf{Y}}^T \triangleq \begin{pmatrix} \mathbf{Y}^T & \mathbf{0} \\ \mathbf{0} & \mathbf{Y}^T \end{pmatrix}, \quad \underline{\mathbf{Y}}^T \in \mathfrak{R}^{2 \times (4n+2)}, \quad \mathbf{Y}^T \in \mathfrak{R}^{2n+1} \quad (6.15)$$

$$\Phi \triangleq \begin{pmatrix} \phi_A \\ \phi_B \end{pmatrix}, \quad \Phi \in \mathfrak{R}^{4n+2}, \quad \phi_A, \phi_B \in \mathfrak{R}^{2n+1} \quad (6.16)$$

and  $\phi_j$  is defined by Eq.(2.14) for  $j = A$  and  $B$ .

The following vectored equations used in the 2-DOF system model are generalized from the definitions in the single-DOF system model provided in section 2.5.

Position sensor signal:

$$\mathbf{x}_s = \mathbf{x} + \mathbf{d}, \quad \mathbf{x}_s \in \mathfrak{R}^2 \quad (6.17)$$

Estimate of geometric position:

$$\bar{\mathbf{x}} \triangleq \mathbf{x}_s - \hat{\mathbf{d}}, \quad \text{equivalently} \quad \bar{\mathbf{x}} = \mathbf{x} + \tilde{\mathbf{d}}, \quad \bar{\mathbf{x}} \in \mathfrak{R}^2 \quad (6.18)$$

Estimate of SRO disturbance:

$$\hat{\mathbf{d}} \triangleq (\hat{d}_A \quad \hat{d}_B)^T, \quad \hat{\mathbf{d}} \in \mathfrak{R}^2 \quad (6.19)$$

where

$$\hat{d}_j \triangleq \hat{a}_{0j} + \sum_{i=1}^n \hat{a}_{ij} \sin(i\omega t) + \hat{b}_{ij} \cos(i\omega t) \quad j = A, B \quad (6.20)$$

SRO disturbance parameter error:

$$\tilde{\mathbf{d}} \triangleq (\mathbf{d} - \hat{\mathbf{d}}) = \underline{\mathbf{Y}}^T \tilde{\Phi}, \quad \tilde{\mathbf{d}} \in \mathfrak{R}^2 \quad (6.21)$$

Weighted sum of estimated velocity and position:

$$\bar{\mathbf{e}} \triangleq (\dot{\hat{\mathbf{x}}} + \lambda \hat{\mathbf{x}}), \quad \bar{\mathbf{e}} \in \mathfrak{R}^2 \quad (6.22)$$

Regressor matrix:

$$\underline{\mathbf{Y}}_m^T \triangleq \underline{\mathbf{K}}_s \underline{\mathbf{Y}}^T - m \underline{\ddot{\mathbf{Y}}}^T, \quad \underline{\mathbf{Y}}_m^T \in \mathfrak{R}^{(4n+2) \times 2} \quad (6.23)$$

Adaptation gain matrix for the SRO components:

$$\underline{\Gamma} \triangleq \begin{pmatrix} \Gamma & \mathbf{0} \\ \mathbf{0} & \Gamma \end{pmatrix}, \quad \underline{\Gamma} \in \mathfrak{R}^{(4n+2) \times (4n+2)}, \quad \Gamma \in \mathfrak{R}^{(2n+1) \times (2n+1)} \quad (6.24)$$

where  $\Gamma$  is defined in Eq.(2.24). The components of  $\Gamma$  are chosen such that  $\mathbf{0} < \underline{\Delta} < \mathbf{I}$

where

$$\underline{\Delta} \triangleq \underline{\mathbf{Y}}^T \underline{\Gamma} \underline{\mathbf{Y}}_m = \begin{pmatrix} \Delta_{AA} & \Delta_{AB} \\ \Delta_{AB} & \Delta_{BB} \end{pmatrix}, \quad \underline{\Delta} \in \mathfrak{R}^{2 \times 2} \quad (6.25)$$

$$\Delta_{AA} = \Delta_{BB} = \sum_{i=0}^n \gamma_i \left[ K_s \left( 1 + \frac{mL^2}{I_T} \right) + m(i\omega)^2 \right] \quad (6.26)$$

$$\Delta_{AB} = - \sum_{i=0}^n \gamma_i K_s \left( 1 - \frac{mL^2}{I_T} \right) \quad (6.27)$$

## 6.3 ASRC for 2-DOF systems

### 6.3.1 Controller Design

For AMB systems with negligible unbalance  $\underline{\mathbf{Y}}_u^T \tilde{\phi}_u = 0$ , Eq.(6.10) becomes

$$m\ddot{\mathbf{x}} = \underline{K}_c \mathbf{I} + \underline{K}_s \mathbf{x} \quad (6.28)$$

The following feedback control action and the adaptation law can be directly extended from the ASRC in the SISO case shown by Eqs.(3.2) and (3.3).

$$\mathbf{I} = -\underline{K}_c^{-1} [\underline{K}_s \mathbf{x} + m\lambda \dot{\mathbf{x}} + c\bar{\mathbf{e}}] \quad (6.29)$$

$$\dot{\tilde{\Phi}} = \underline{\Gamma} \underline{\mathbf{Y}}_m \bar{\mathbf{e}} \quad (6.30)$$

The proof of stability for the 2-DOF system model is similar the proof of the ASRC for single-DOF system model in section 3.3. Briefly, we can summarize the proof below.

Substituting Eq.(6.29) to Eq.(6.28) we obtain

$$m\ddot{\mathbf{x}} = -\underline{K}_s \tilde{\mathbf{d}} - m\lambda \dot{\mathbf{x}} - c\bar{\mathbf{e}} \quad (6.31)$$

Using the relation  $\ddot{\tilde{\mathbf{x}}} = \ddot{\mathbf{x}} + \ddot{\tilde{\mathbf{d}}}$  from Eq.(6.18), and  $\dot{\tilde{\mathbf{e}}} = \dot{\tilde{\mathbf{x}}} + \lambda \dot{\tilde{\mathbf{x}}}$  from Eq.(6.22), the

above equation can be rewritten as

$$m \dot{\mathbf{e}} = m \ddot{\mathbf{d}} - \underline{K} \tilde{\mathbf{d}} - c \bar{\mathbf{e}} \quad (6.32)$$

The term  $\ddot{\mathbf{d}}$  can be derived from Eq.(6.21).

$$\ddot{\mathbf{d}} = \underline{\ddot{\mathbf{Y}}}^T \tilde{\Phi} + 2 \underline{\dot{\mathbf{Y}}}^T \dot{\tilde{\Phi}} + \underline{\mathbf{Y}}^T \ddot{\tilde{\Phi}} \quad (6.33)$$

$$= \underline{\ddot{\mathbf{Y}}}^T \tilde{\Phi} + 2 \underline{\dot{\mathbf{Y}}}^T \underline{\Gamma} \underline{\mathbf{Y}}_m \dot{\mathbf{e}} + \underline{\mathbf{Y}}^T \underline{\Gamma} \underline{\dot{\mathbf{Y}}}_m \bar{\mathbf{e}} + \underline{\mathbf{Y}}^T \underline{\Gamma} \underline{\mathbf{Y}}_m \dot{\mathbf{e}} \quad (6.34)$$

In the above equation, the adaptation law in Eq.(6.30) is used to derive  $\ddot{\tilde{\Phi}}$ . Knowing  $\underline{\dot{\mathbf{Y}}}^T \underline{\Gamma} \underline{\mathbf{Y}}_m = \mathbf{0}$ ,  $\underline{\mathbf{Y}}^T \underline{\Gamma} \underline{\dot{\mathbf{Y}}}_m = \mathbf{0}$  and Eq.(6.25), we can write

$$\ddot{\mathbf{d}} = \underline{\ddot{\mathbf{Y}}}^T \tilde{\Phi} + \underline{\Delta} \dot{\mathbf{e}} \quad (6.35)$$

Therefore using Eqs.(6.23) and(6.35) we can express Eq.(6.32) as

$$m (\mathbf{I} - \underline{\Delta}) \dot{\mathbf{e}} = -\underline{\mathbf{Y}}_m^T \tilde{\Phi} - c \bar{\mathbf{e}} \quad (6.36)$$

Using the Lyapunov function candidate

$$V = \frac{1}{2} m \bar{\mathbf{e}}^T (\mathbf{I} - \underline{\Delta}) \bar{\mathbf{e}} + \frac{1}{2} \tilde{\Phi}^T \underline{\Gamma}^{-1} \tilde{\Phi}, \quad \mathbf{0} < \underline{\Delta} < \mathbf{I} \quad (6.37)$$

we can find its derivative along the trajectory of Eq.(6.36) as

$$\begin{aligned} \dot{V} &= m \bar{\mathbf{e}}^T (\mathbf{I} - \underline{\Delta}) \dot{\mathbf{e}} + \tilde{\Phi}^T \underline{\Gamma}^{-1} \dot{\tilde{\Phi}} \\ &= -m \bar{\mathbf{e}}^T \left( \underline{\mathbf{Y}}_m^T \tilde{\Phi} + c \bar{\mathbf{e}} \right) + \tilde{\Phi}^T \underline{\Gamma}^{-1} \dot{\tilde{\Phi}} \end{aligned} \quad (6.38)$$

The use of the adaptation law in Eq.(6.30) results to

$$\dot{V} = -c \bar{\mathbf{e}}^T \bar{\mathbf{e}} \leq 0 \quad (6.39)$$

Using Barbalat's lemma we can conclude that  $\bar{\mathbf{e}} \rightarrow \mathbf{0}$ ,  $\bar{\mathbf{x}} \rightarrow \mathbf{0}$  and  $\tilde{\Phi}$  is bounded. Furthermore, ones can find that the regressor vector  $\underline{\mathbf{Y}}_m^T \in \mathfrak{R}^{2 \times (4n+2)}$  does not meet the persistency of excitation condition. The analytical proof is a straightforward extension to higher dimensions of its counterpart in Eq.(3.14), which is not provided in this thesis since it is beyond the scope of this thesis. However, the convergence of estimated parameters and the performance of the closed-loop system are investigated by simulations in the next section.

Table 6.1. Simulation parameters for 2-DOF magnetic bearing systems

Angular speed: $\omega = 2\pi \times 25$ rad/s
Total rotor mass: $m = 4.86$ kg
Distance from rotor center to sensor-actuator: $L = 0.072$ m
Transverse moment of inertia : $I_T = 0.064$ kg/m <sup>2</sup>
Sensor runout in $x_1$ axis (bearing A): $a_0 = 2.5$ $\mu\text{m}$ $a_1 = 18.35$ $\mu\text{m}$ ; $b_1 = 4.92$ $\mu\text{m}$ ; $a_i = b_i = 0$ for $i \geq 2$
Sensor runout in $x_2$ axis (bearing B): $a_0 = -1$ $\mu\text{m}$ $a_1 = -12.07$ $\mu\text{m}$ ; $b_1 = 3.24$ $\mu\text{m}$ ; $a_i = b_i = 0$ for $i \geq 2$
Error gains: $\lambda = 400$ $s^{-1}$ ; $c = 1200$ kg/s
Plant initial conditions: $x(t=0) = -0.1 \times 10^{-3}$ m; $\theta(t=0) = 3 \times 10^{-4}$ rad $\dot{x}(t=0) = 0$ ; $\dot{\theta}(t=0) = 0$

### 6.3.2 Simulation Results

For simulations we use the bearing parameters shown in Table A.3 with the total mass of the rotor,  $m = 4.86$  kg. The controller parameters and the assumed SRO disturbance are shown in Table 6.1. The adaptation is performed up to the third harmonic using the adaptation gain matrix  $\Gamma = \text{diag}(1, 2, 2, 1, 1) \times 10^{-7}$  m/N for both axes as shown in Eq.(6.24). We can verify that

$$\underline{\Delta} = \begin{pmatrix} 0.4385 & -0.1467 \\ -0.1467 & 0.4385 \end{pmatrix}$$

which has eigenvalues of 0.585 and 0.292; thus the condition  $\mathbf{0} < \underline{\Delta} < \mathbf{I}$  is satisfied. All estimated parameters in both axes were initialized zero.

The simulation result in Figure 6.2 shows that at the steady state the geometric centers of both axes,  $x_A$  and  $x_B$ , become constant; thus the controller is able to remove the periodic disturbance due to the SRO. However,  $x_A$  and  $x_B$  converge to positions other than the origin. As seen in Figure 6.2 the DC parameters do not converge to the true values while the parameters of higher harmonics seen in Figure 6.3 converge to the true values. Therefore, generalizing the ASRC scheme from SISO to the MIMO system model can not guarantee the convergence of all estimated parameters to the true values. In section 6.5, we will present the effect of bias current excitation on ASRC in 2-DOF systems to solve this problem.

## 6.4 SRUC-BCE for 2-DOF Systems

### 6.4.1 Controller Design

In the presence of SRO and unbalance, the system dynamics are given by Eq.(6.10). The following feedback and adaptation laws, generalized from Eqs.(5.24) through

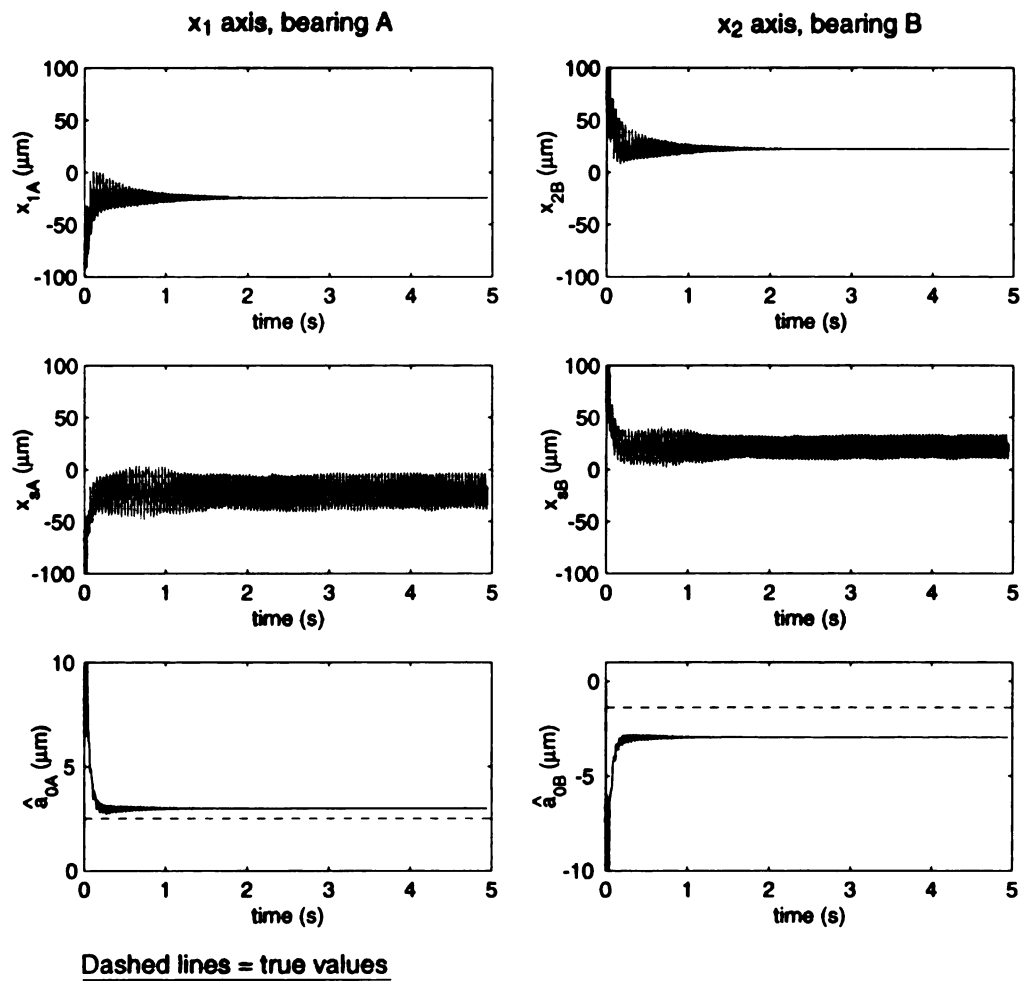


Figure 6.2. Geometric position, sensor signal, and DC component error of ASRC for 2-DOF system model

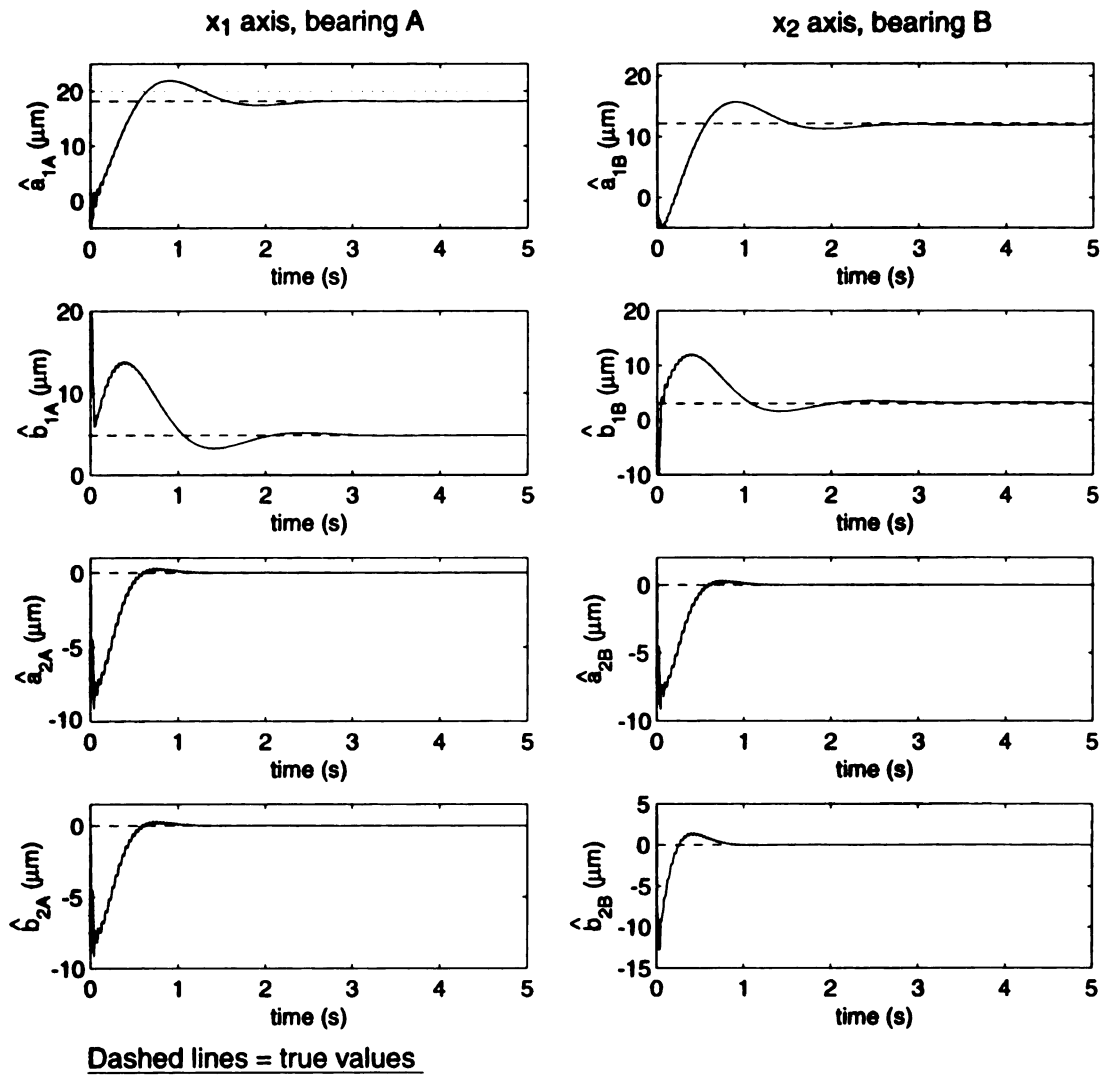


Figure 6.3. Higher harmonics error of ASRC for 2-DOF system model

(5.26), are considered.

$$\mathbf{I} = -\underline{K}_c^{-1} \left[ \underline{K}_s \mathbf{x} + m \lambda \dot{\mathbf{x}} + \frac{1}{2} m \underline{\Delta} + c \bar{\mathbf{e}} + \underline{\mathbf{Y}}_u^T \tilde{\phi}_u \right] \quad (6.40)$$

$$\dot{\tilde{\Phi}} = \underline{\Gamma} \underline{\mathbf{Y}}_m \bar{\mathbf{e}} \quad \dot{\tilde{\phi}}_u = -\underline{\Gamma}_u \underline{\mathbf{Y}}_u \bar{\mathbf{e}} \quad (6.41)$$

In each axis, we may excite the bias currents using the procedure outlined in Eqs.(5.3) through (5.20). We may also assume that the amplitude, frequency, and phase of the excitation are the same on both axes.

The following is the proof of stability that closely follows its counterpart in the 1-DOF case described in section 5.3.

$$m \ddot{\mathbf{x}} = -\underline{K}_s \underline{\mathbf{Y}}^T \tilde{\Phi} - m \lambda \dot{\mathbf{x}} - (c + \frac{1}{2} m \underline{\Delta}) \bar{\mathbf{e}} - \underline{\mathbf{Y}}_u^T \tilde{\phi}_u \quad (6.42)$$

Using the relations  $\ddot{\tilde{\mathbf{x}}} = \ddot{\mathbf{x}} + \ddot{\mathbf{d}}$  from Eq.(6.18), and  $\dot{\tilde{\mathbf{e}}} = \dot{\tilde{\mathbf{x}}} + \lambda \dot{\mathbf{x}}$  from Eq.(6.22), the above equation can be rewritten as

$$m \dot{\tilde{\mathbf{e}}} = m \ddot{\mathbf{d}} - \underline{K}_s \underline{\mathbf{Y}}^T \tilde{\Phi} - (c + \frac{1}{2} m \underline{\Delta}) \bar{\mathbf{e}} - \underline{\mathbf{Y}}_u^T \tilde{\phi}_u \quad (6.43)$$

From Eqs.(6.21) and (6.41), we can write

$$\ddot{\mathbf{d}} = \underline{\ddot{\mathbf{Y}}}^T \tilde{\Phi} + 2 \underline{\dot{\mathbf{Y}}}^T \dot{\tilde{\Phi}} + \underline{\mathbf{Y}}^T \ddot{\tilde{\Phi}} \quad (6.44)$$

$$= \underline{\ddot{\mathbf{Y}}}^T \tilde{\Phi} + 2 \underline{\dot{\mathbf{Y}}}^T \underline{\Gamma} \underline{\mathbf{Y}}_m \dot{\bar{\mathbf{e}}} + \underline{\mathbf{Y}}^T \underline{\Gamma} \underline{\dot{\mathbf{Y}}}_m \bar{\mathbf{e}} + \underline{\mathbf{Y}}^T \underline{\Gamma} \underline{\mathbf{Y}}_m \dot{\bar{\mathbf{e}}} \quad (6.45)$$

Knowing  $\underline{\dot{\mathbf{Y}}}^T \underline{\Gamma} \underline{\mathbf{Y}}_m = 0$  and the relations in Eq.(6.25) the above equation becomes

$$\ddot{\mathbf{d}} = \underline{\ddot{\mathbf{Y}}}^T \tilde{\Phi} + \underline{\Delta} \bar{\mathbf{e}} + \underline{\Delta} \dot{\bar{\mathbf{e}}} \quad (6.46)$$

Utilizing Eqs.(6.23) and (6.46), we can expressed Eq.(6.43) as

$$m(\mathbf{I} - \underline{\Delta})\dot{\bar{\mathbf{e}}} = -\underline{\mathbf{Y}}_m^T \tilde{\Phi} + \frac{1}{2}m\dot{\underline{\Delta}}\bar{\mathbf{e}} - c\bar{\mathbf{e}} - \underline{\mathbf{Y}}_u^T \tilde{\phi}_u \quad (6.47)$$

Using the Lyapunov function candidate

$$V = \frac{1}{2} \left[ \bar{\mathbf{e}}^T (\mathbf{I} - \underline{\Delta}) m \bar{\mathbf{e}} + \tilde{\Phi}^T \underline{\Gamma}^{-1} \tilde{\Phi} + \tilde{\phi}_u^T \underline{\Gamma}_u^{-1} \tilde{\phi}_u \right] \quad (6.48)$$

we can write

$$\dot{V} = m\bar{\mathbf{e}}^T (\mathbf{I} - \underline{\Delta}) \dot{\bar{\mathbf{e}}} - \frac{1}{2}m\bar{\mathbf{e}}^T \dot{\underline{\Delta}}\bar{\mathbf{e}} + \tilde{\Phi}^T \underline{\Gamma}^{-1} \dot{\tilde{\Phi}} + \tilde{\phi}_u^T \underline{\Gamma}_u^{-1} \dot{\tilde{\phi}}_u \quad (6.49)$$

$$\dot{V} = -c\bar{\mathbf{e}}^T \bar{\mathbf{e}} \leq 0 \quad (6.50)$$

Again, using Barbalat's lemma we conclude that  $\bar{\mathbf{x}} \rightarrow \mathbf{0}$ ,  $\bar{\mathbf{e}} \rightarrow \mathbf{0}$ , and  $\tilde{\Phi}$  and  $\tilde{\phi}_u$  are bounded. Moreover, ones can find that the regressor vector  $[\underline{\mathbf{Y}}_m^T \quad -\underline{\mathbf{Y}}_u^T] \in \mathfrak{R}^{2 \times (4n+4)}$  satisfies the persistency of excitation condition. The analytical proof is a straightforward extension to higher dimensions of its counterpart in Eq.(5.40), which is not provided in this thesis since it is beyond the scope of this thesis. The effectiveness of SRUC-BCE for 2-DOF systems is further investigated by simulations.

## 6.4.2 Simulation Results

Simulations of the SRUC-BCE for 2-DOF model were performed using the parameters shown in Tables A.3 and 6.1. The adaptive controller considers up the second harmonic of the SRO and uses  $\Gamma = \text{diag}(1, 2, 2) \times 10^{-7}$  m/N for both axes. We can

verify that the condition  $\mathbf{0} < \underline{\Delta} < \mathbf{I}$  is satisfied knowing

$$\underline{\Delta} = \begin{pmatrix} 0.2869 & -0.11 \\ -0.11 & 0.1869 \end{pmatrix}$$

and the eigenvalues of  $\underline{\Delta}$  are 0.397 and 0.179. For the unbalance identification, the adaptation gain  $\Gamma_u = \text{diag}(3, 3) \times 10^{-5} m/N$  was used. We assume that the true values of the unbalance:  $p = 86.6 \mu m$ , and  $q = 50.0 \mu m$ . We initialized all estimated parameters to zero and excite the bias currents in both axes after  $t = 5s$ . The amplitude of bias current excitation for both axes were set to 0.22 A with the frequency of 10 Hz.

The simulation result in Figure 6.4 shows that the controller is able to remove the periodic disturbance due to the SRO. However, the geometric centers of both axes converge to positions other than the origin when  $t < 5$ . After the bias current excitation, as seen in Figures (6.4) and (6.5), all estimated parameters converge to the true values within 250 s.

## 6.5 ASRC-BCE for 2-DOF systems

By removing all variables related to the unbalance, the controller proposed in section 6.4 may be reduced to obtain an ASRC with BCE. Therefore, assuming that the unbalance force is negligible we may use following controller together with bias current excitation.

$$\mathbf{I} = -\underline{K}_c^{-1} \left[ \underline{K}_s \mathbf{x} + m\lambda \dot{\mathbf{x}} + \frac{1}{2} m \dot{\underline{\Delta}} + c\bar{\mathbf{e}} \right] \quad (6.51)$$

$$\dot{\underline{\Phi}} = \underline{\Gamma} \underline{Y}_m \bar{\mathbf{e}} \quad (6.52)$$

The proof of stability for this system is trivial. It can be easily established from section 6.4 by removing all variables related to unbalance. Therefore, we can also conclude

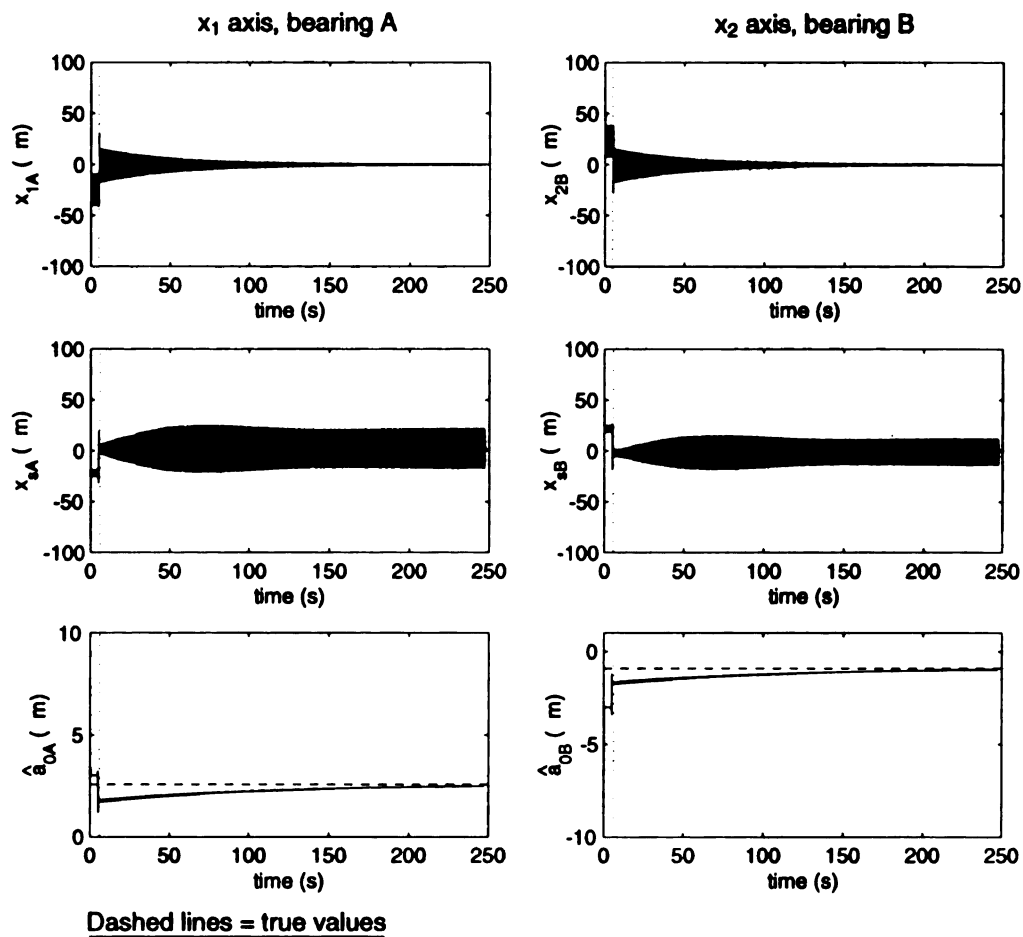


Figure 6.4. Geometric position, sensor signal, and DC component error of SRUC-BCE for 2-DOF system model

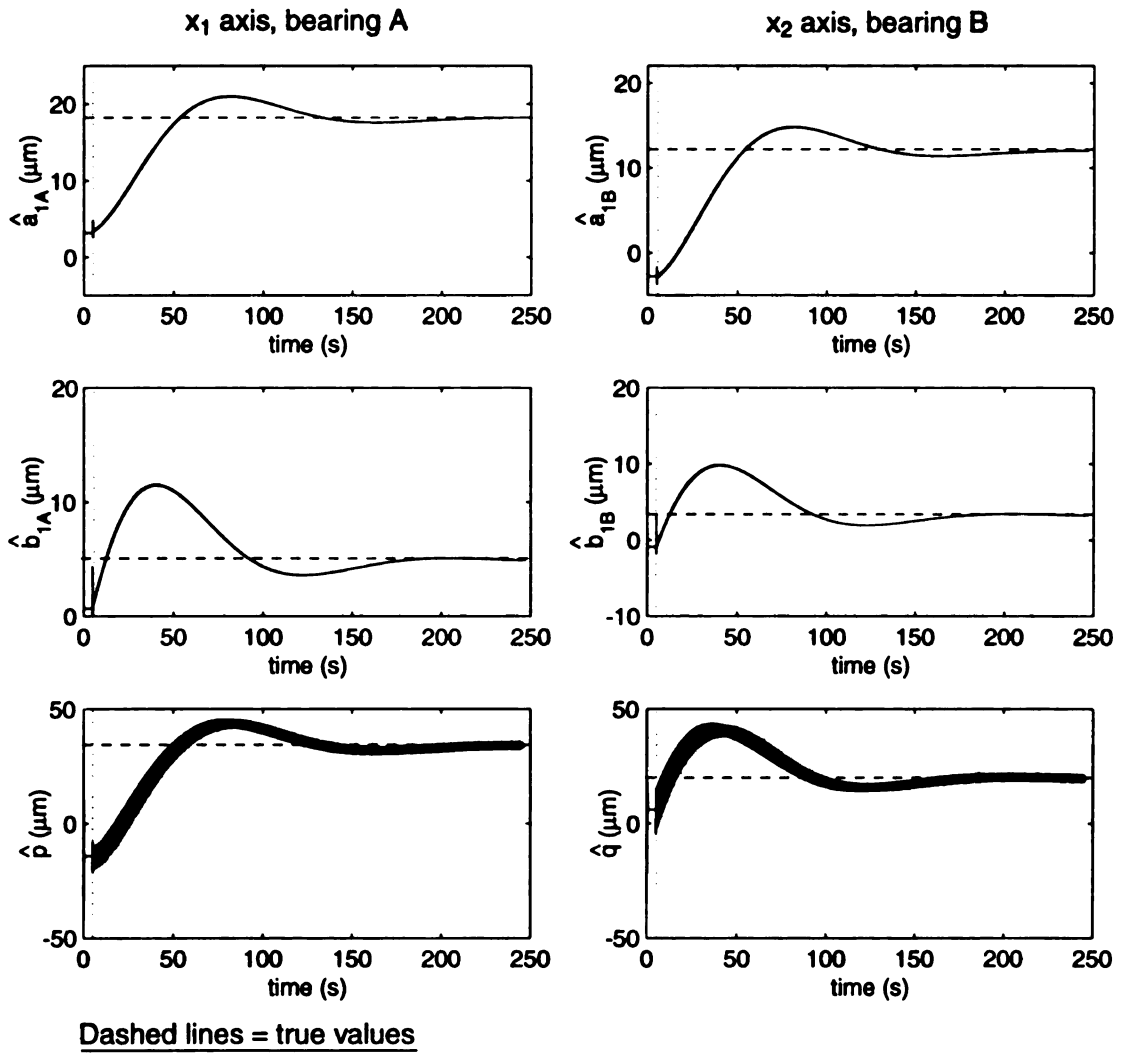


Figure 6.5. Higher harmonics error of SRUC-BCE for 2-DOF system model

that  $\bar{\mathbf{e}} \rightarrow \mathbf{0}$ ,  $\bar{\mathbf{x}} \rightarrow \mathbf{0}$  and  $\Phi$  is bounded using the Barbalat's lemma. Similarly, ones can find that the regressor vector  $\underline{\mathbf{Y}}_m^T \in \mathfrak{R}^{2 \times (4n+2)}$  satisfies the persistency of excitation condition. The analytical proof is a straightforward extension to higher dimensions of its counterpart in Eq.(3.14), which is not provided in this thesis since it is beyond the scope of this thesis. Figures 6.6 and 6.7 show that a relatively small amplitude of bias current excitation, 0.05A with frequency of 10 Hz can effectively stabilize the rotor geometric center in both axes to the origin. The excitation is started at  $t = 2$  second. It can be seen that the DC components converge to their true values in 2 seconds after the bias current excitation commences.

## 6.6 Summary and Remarks

The effectiveness of the adaptive algorithms in MIMO systems has been investigated. The stability proofs of the adaptive algorithms for the MIMO model are very similar to their counterparts in the SISO model. The proof of convergence of estimated parameters was however not pursued analytically. Instead we used numerical simulations to observe that ASRC in MIMO systems, unlike in SISO systems, requires bias current excitation for proper estimation of all parameters and geometric center stabilization. In the absence of bias current excitation the DC components of SRO are not estimated correctly. A relatively small amplitude of bias current excitation, however, results in very fast convergence of the DC components to their true values. The extension of our SRUC-BCE algorithm to MIMO systems from SISO system was straightforward and results in geometric center stabilization with proper identification of SRO in both bearings as well as mass unbalance.

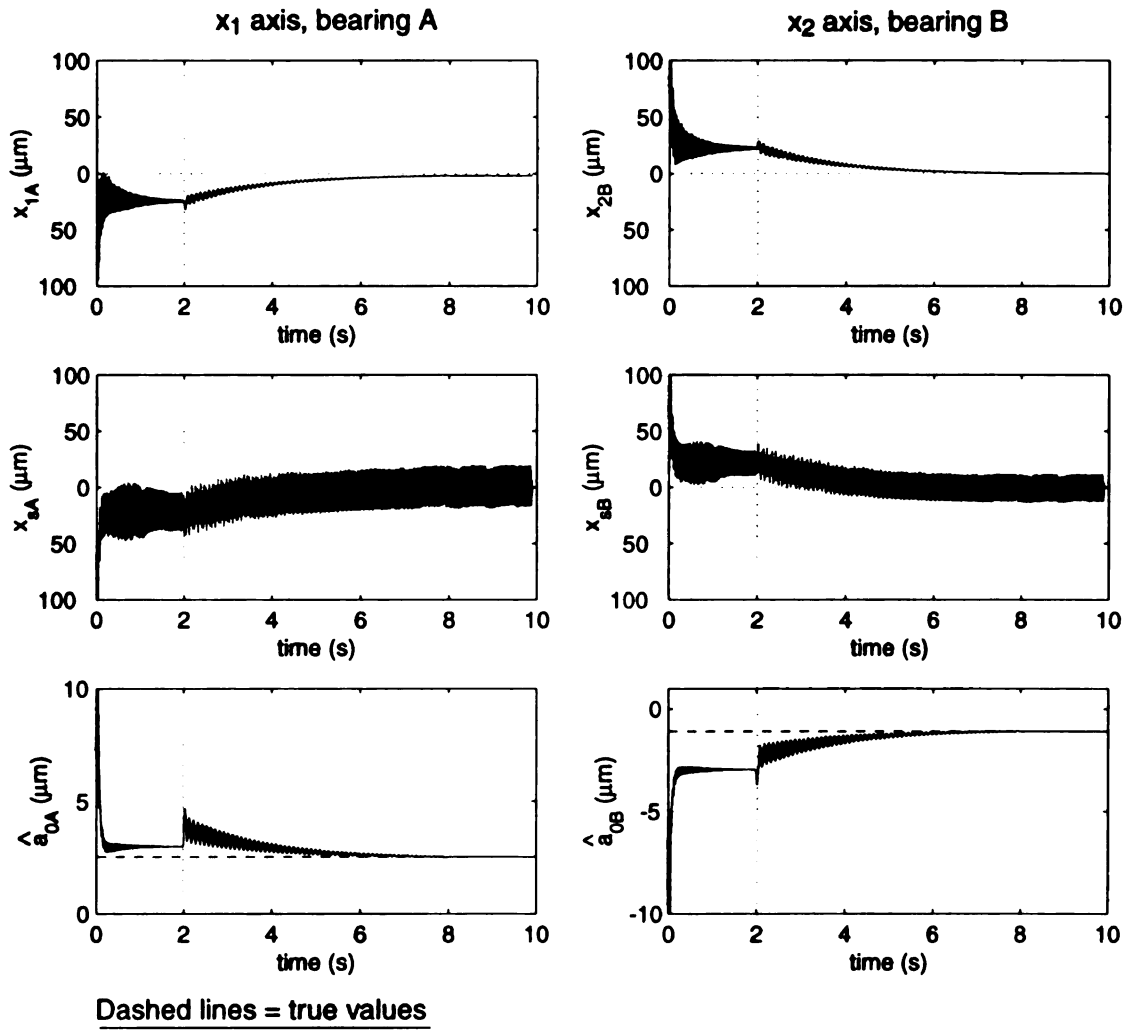


Figure 6.6. Geometric position, sensor signal and DC component error of ASRC-BCE for 2-DOF system model

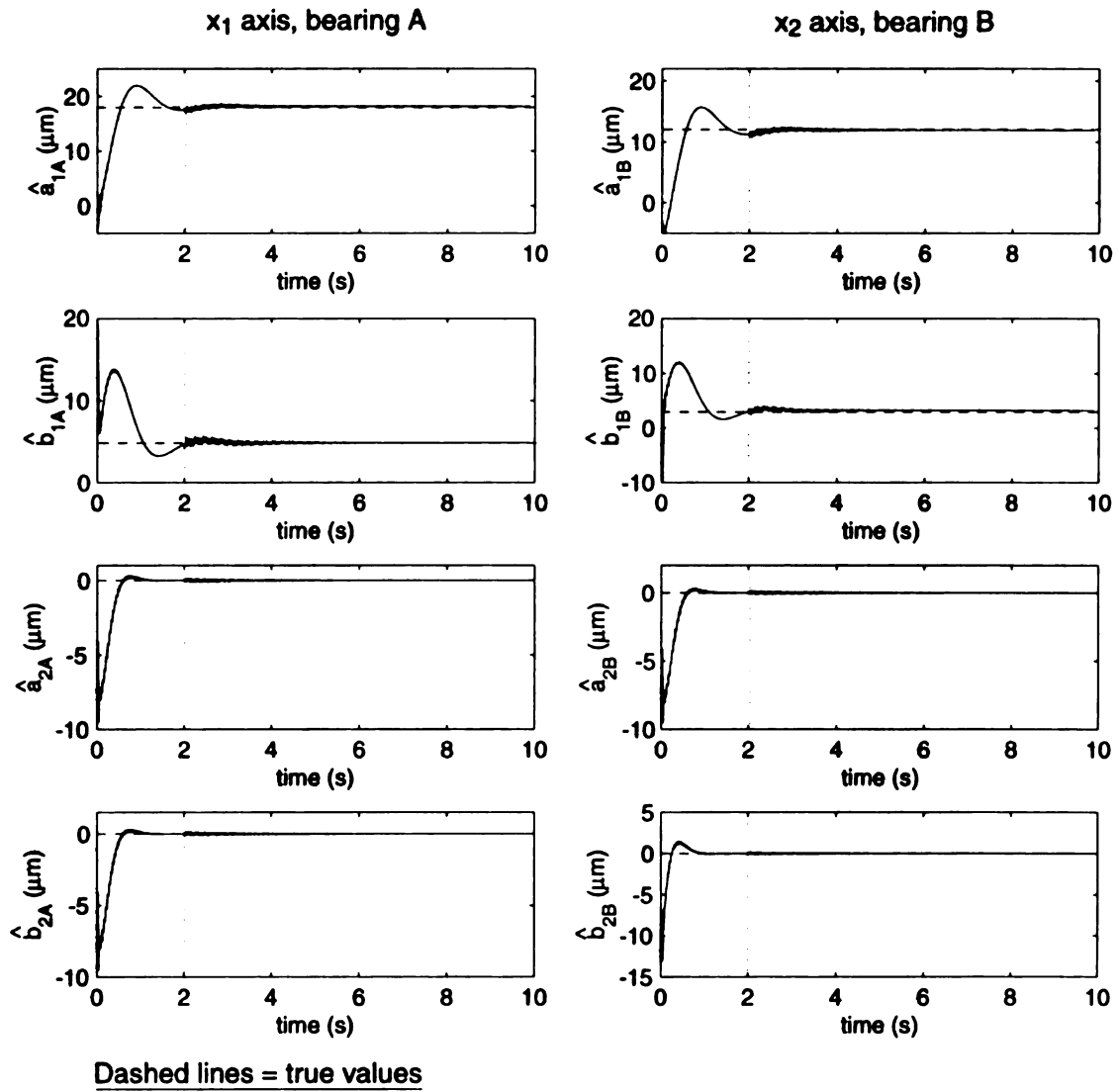


Figure 6.7. Higher harmonics error of ASRC-BCE for 2-DOF system model

# CHAPTER 7

## Conclusions

### 7.1 Research Summary

The results presented in this thesis establish a new adaptive control framework for identification and compensation of periodic disturbances in active magnetic bearing systems with a rigid rotor. The advantages of the algorithms include robustness to uncertain plant parameters, simplicity of design, and ease of implementation. The algorithms are shown to apply to magnetic bearing systems modeled both as SISO and MIMO systems.

Within this framework, we first design an algorithm for adaptive compensation of sensor runout in SISO model, assuming that the mass unbalance is negligible. The algorithm is developed using powerful tools such as Lyapunov stability theory and persistency of excitation concept. We prove that the algorithm guarantees stability of the rotor geometric center about the origin and correct identification of the harmonics of sensor runout disturbance. Using passivity analysis we show that the algorithm is robust to plant parameter uncertainties. The averaging method successfully predicts the convergence rate of the adaptation; thus, the averaging method can be useful in the selection of controller gains in our algorithm. Simulation and experimental results validate the effectiveness of the algorithm.

We next address the problem of rotor stabilization about the geometric center in

the presence of combined sensor runout and mass unbalance. Our first approach to this problem is based on multiple speeds. This approach lacks robustness and has a number of drawbacks including the need for speed alteration, which will not be permissible in many applications. To overcome the limitations, we develop a new method for simultaneous on-line identification of both disturbances at constant rotor speed. This is achieved through persistency of excitation generated by methodical bias current excitation that does not alter the equilibrium condition of the rotor. After successful demonstration of the approach through simulations and experiments, we study the effects of excitation frequency, excitation amplitude, and harmonic content of excitation on the convergence of parameters. The robustness of the algorithm to parametric uncertainties and convergence rate of the parameters was also investigated.

We further develop an adaptive algorithm that allows identification of both sensor runout and unbalance simultaneously without changing the angular speed. Using bounded external excitation such as bias current excitation we show that the regressor vector can be made persistently exciting to guarantee the convergence of estimated parameters to the true values. We verify that the excitation with one harmonic at the frequency about a half of the rotor frequency can be used. With the help of the passivity analysis, the effect of uncertain plant parameters to the convergence of estimate parameters are studied. It reveals that the algorithm is robust to the uncertainties in mass and magnetic stiffness. However, the rotor center of geometric may slightly fluctuate due to the uncertainty in the actuator gain. In order to predict the effect of the control and plant parameters to the convergence rate of the adaptation, the averaging method is again utilized. However, it was found that the averaging system could not capture the important dynamics of the system; thus simulations are still preferred to investigate the convergence rate of the adaptation. Both simulation and experimental results validate the effectiveness of the algorithm.

Finally, we investigate the extension of the algorithms for MIMO system model.

The stability proofs for using the adaptive algorithms are presented. However, due to the complexity of the MIMO system, we evaluate the convergence of the estimated parameters by simulations only to illustrate the possibility of extension.

## 7.2 Future Work

The present work has revealed a number of areas that warrant additional investigation and research. In the SISO system model, one may modify the algorithm to include a robust control term such that the stability is still guaranteed in the presence of unmodeled dynamics. The robust control term may also be designed to improve the algorithm in the presence of time varying uncertainty in the actuator gain. In the MIMO system model, modification of the adaptive controller will be required if gyroscopic forces are taken into account. Within saturation limits, the optimum bias current excitation for rapid parameter estimation is a subject that needs further investigation. Since the stability proof of the proposed algorithms assume that the operation is at a constant angular speed, one may also investigate the stability of the closed-loop system when the angular speed varies. The effectiveness of the adaptive algorithms using MIMO system model still needs to be verified experimentally. Extending the MIMO system model to include the effect of rotor flexibility may also be pursued.

# **APPENDICES**

## APPENDIX A

### Experimental Set-up

#### A.1 Magnetic Bearing Set-Up

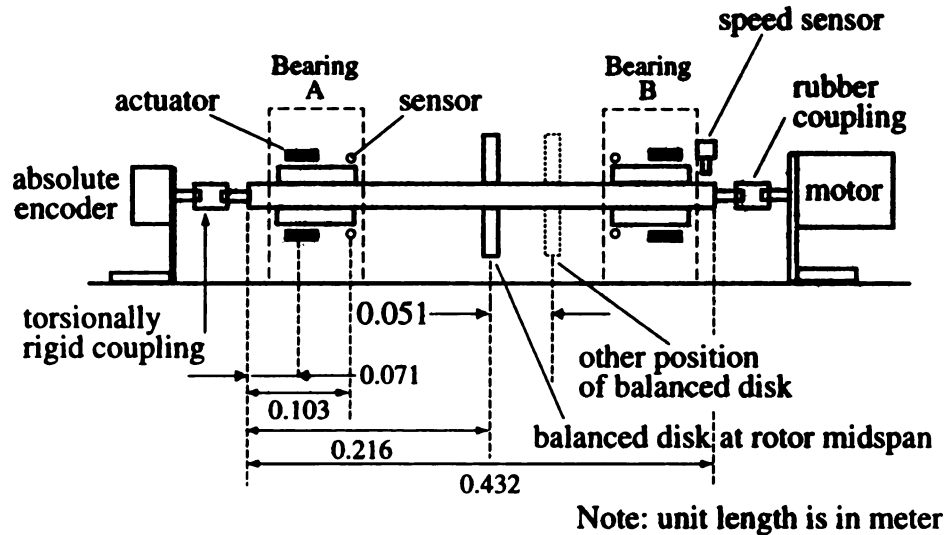


Figure A.1. Magnetic bearing rig schematic

#### A.2 Structural-Dynamic Analysis of Two-Bearing Rotor

Structural-dynamic analysis was performed to determine the mode shapes and the resonant frequencies of the two-bearing rotor. The rotor dimensions are shown in Figure A.3 and Table A.1. A program "MODAL" is used to generate a modally reduced state space model of a single free-free rotor. This program is provided by ROMAC Laboratory, University of Virginia. The detail instruction for the program is available in reference [20]. To utilize the MODAL program, we discretize the rotor as shown in Figure A.3. The input to the program is provided by file name **msu4.dat**. The results of the analysis are summarized in Table A.1 and Figure A.4.

To evaluate the effect of bearing stiffness to the rotor resonant frequency, the use of rotor critical speed map is useful as described in reference [5]. We generated the rotor critical speed map using a ROMAC's program "CRTSP\_2" with the input file **msu4a.dat**. In this program gyroscopic effect is suppressed [20]. The result is shown in Figure A.5.

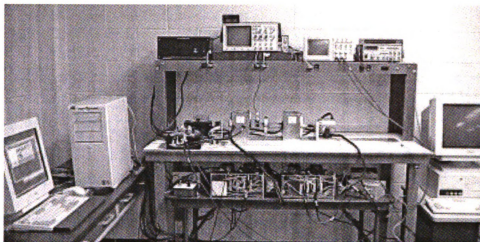


Figure A.2. Picture of magnetic bearing set-up

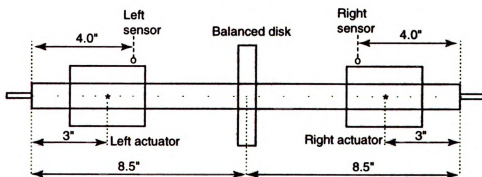


Figure A.3. Dimension of two-bearing rotor with balanced disk

Table A.1. Two-bearing rotor data

Total weight of the two-bearing rotor with balanced disk : 10.7 $lb_m$
Rotor shaft: length = 17 in, diameter = 1 in
Journal bearing: length = 3 in, diameter = 2.4 in
Left-tip: length = 1 in, diameter = 0.25 in
Right-tip: length = 1 in, diameter = 0.3 in
Balanced disk: length = 0.75 in, diameter = 4 in

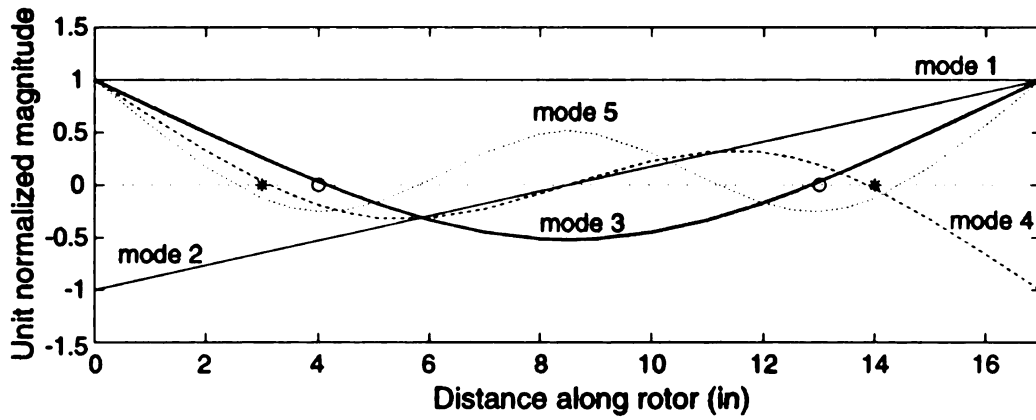


Figure A.4. Free-free modes shapes of rotor

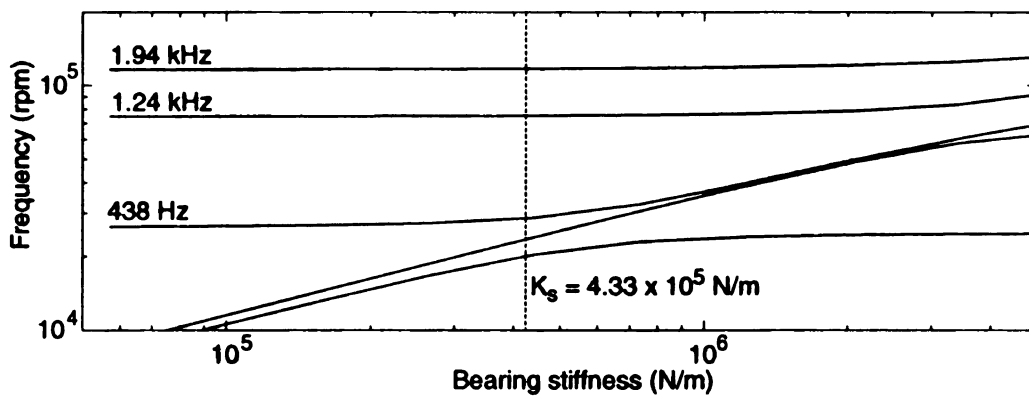


Figure A.5. Rotor critical speed map

Table A.2. Free-free undamped natural frequencies of rotor

Mode	Frequency
1	0
2	0
3	438 Hz
4	1.24 kHz
5	1.94 kHz

Input for ROMAC's software version 1.5, program MODAL.  
 ROMAC is copyright of University of Virginia.

File name: **msu4.dat**

MSU's 17in rotor model  
 jds, 8 June 2000  
 derived from

```

23
5
-1      -3      2      0.
0.0    1.00    0.9843  0.  0.  0.  29.5  0.28
0.0    1.00    0.9843  0.  0.  0.  29.5  0.28
1.033  0.50    0.9843  0.  0.  0.  29.5  0.28
0.0    0.50    0.9843  0.  0.  0.  29.5  0.28
1.033  0.50    0.9843  0.  0.  0.  29.5  0.28 1 1 0 0 "Left actuator"
0.0    0.50    0.9843  0.  0.  0.  29.5  0.28
1.033  1.00    0.9843  0.  0.  0.  29.5  0.28 0 1 0 0 "Left sensor"
0.0    1.00    0.9843  0.  0.  0.  29.5  0.28
0.0    1.00    0.9843  0.  0.  0.  29.5  0.28
0.0    1.00    0.9843  0.  0.  0.  29.5  0.28
0.0    0.50    0.9843  0.  0.  0.  29.5  0.28
0.9    0.50    0.9843  0.  0.  0.  29.5  0.28
0.0    1.00    0.9843  0.  0.  0.  29.5  0.28
0.0    1.00    0.9843  0.  0.  0.  29.5  0.28
0.0    1.00    0.9843  0.  0.  0.  29.5  0.28
0.0    1.00    0.9843  0.  0.  0.  29.5  0.28
1.033  0.50    0.9843  0.  0.  0.  29.5  0.28 0 1 0 0 "Right sensor"
0.0    0.50    0.9843  0.  0.  0.  29.5  0.28
1.033  0.50    0.9843  0.  0.  0.  29.5  0.28 1 1 0 0 "Right actuator"
0.0    0.50    0.9843  0.  0.  0.  29.5  0.28
1.033  1.00    0.9843  0.  0.  0.  29.5  0.28
0.0    1.00    0.9843  0.  0.  0.  29.5  0.28
0.0    0.00    0.9843  0.  0.  0.  29.5  0.28
10.    200000.  2
1
  
```



### A.3 Plant Parameters

Table A.3. Magnetic bearing parameters for single-DOF Model

Parameter	Value
Half-rotor mass, $m$	2.43 kg
Electromagnetic force constant, $k$	$2.82 \times 10^{-6} \text{ Nm}^2/\text{A}^2$
Nominal air gap, $l$	$0.508 \times 10^{-3} \text{ m}$
Top bias current, $i_{10}^*$	2.41 A
Bottom bias current, $i_{20}^*$	2.06 A
Actuator gain, $K_c^*$	97.71 N/A
Sensor gain, $G_s$	$2 \times 10^4 \text{ V/m}$
Open-loop stiffness, $K_s^*$	$4.33 \times 10^5 \text{ N/m}$

Note that for constant bias currents cases as in Chapters 3 and 4, and section 6.3:  
 $i_{10} = i_{10}^*$ ,  $i_{20} = i_{20}^*$ ,  $K_c = K_c^*$ , and  $K_s = K_s^*$ .

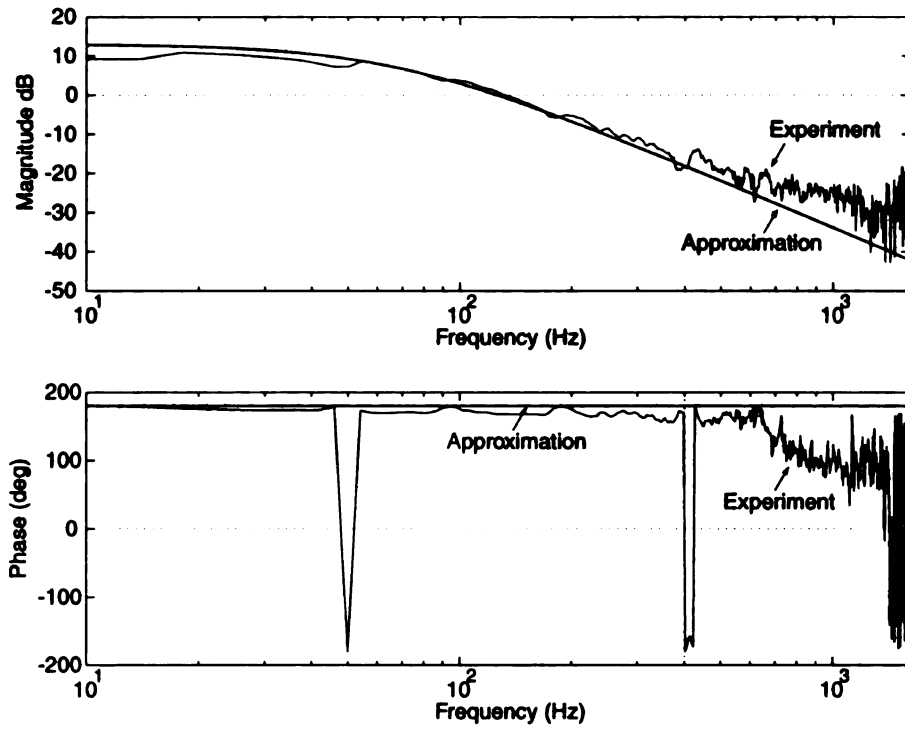


Figure A.6. Bode plot of single-DOF magnetic bearing model

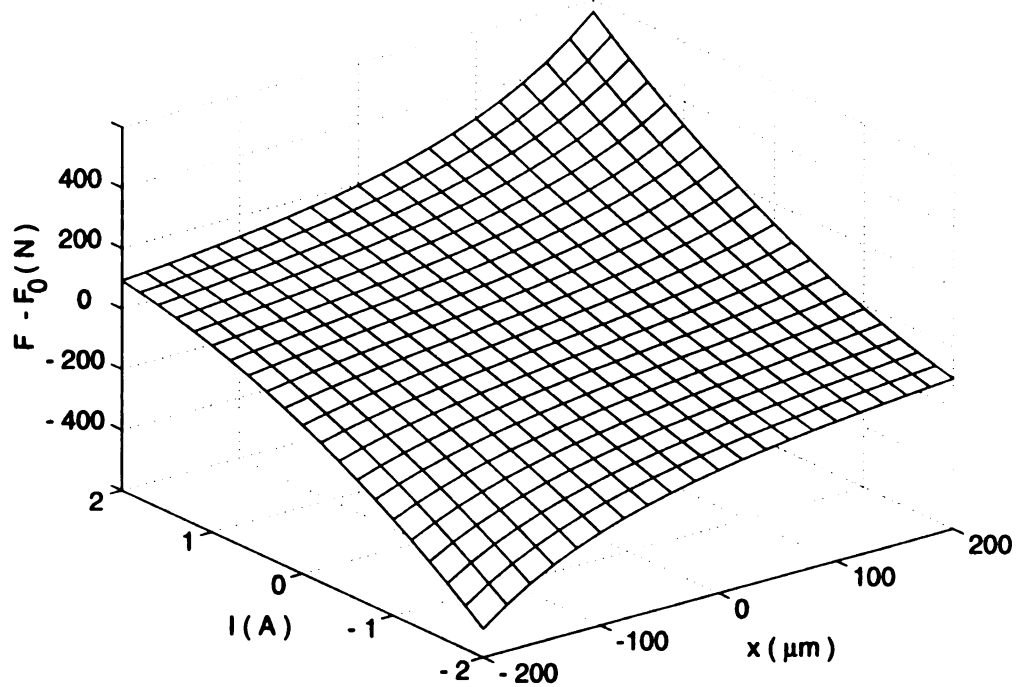


Figure A.7. 3-D Plot of magnetic force surface

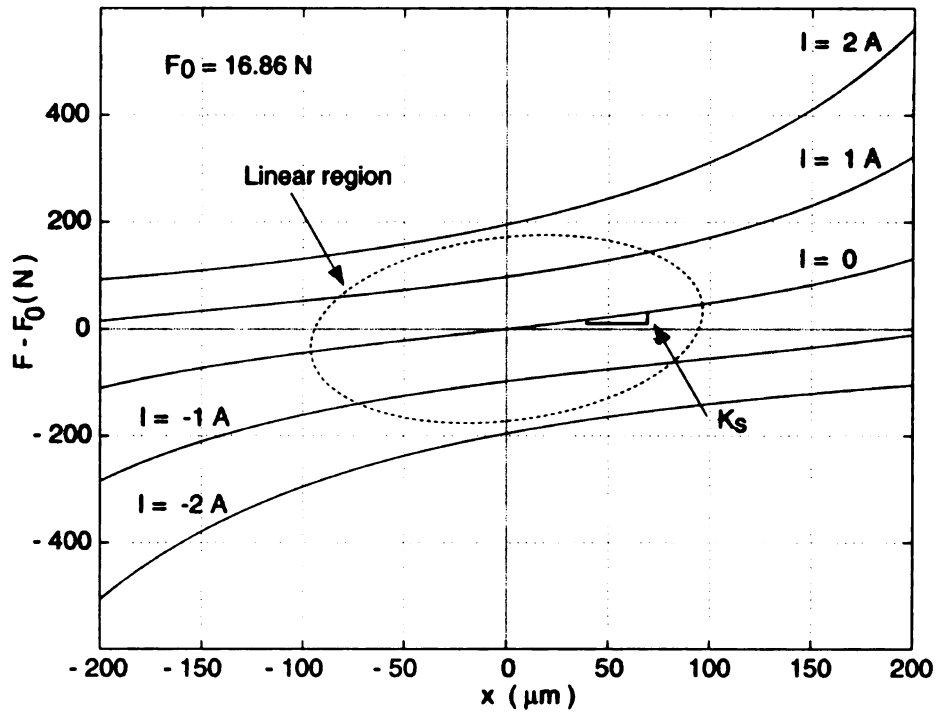


Figure A.8. Magnetic force vs. Position

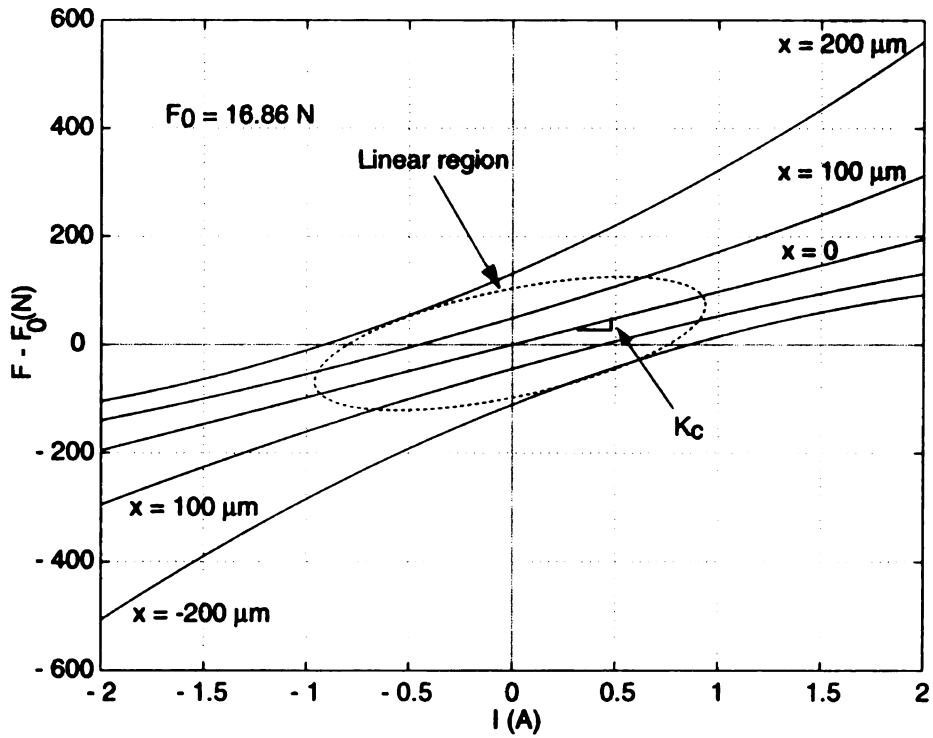


Figure A.9. Magnetic force vs. Current

## A.4 Power Amplifier Data

The power amplifiers are manufactured by Advanced Motion Controls Inc. Each power amplifier unit consists of a power supply that converts 120 VAC to 80 VDC with a maximum current of 15 A. This power supply hosts four 25A-Series PWM servo amplifiers with model number 12A8. The specifications of the PWM servo amplifiers are given in Table A.4. The servo amplifier is set to the current-mode. Each servo amplifier requires that the resistor labeled R30 on the board be replaced with 900 K-Ohm in order to achieve 1.6 kHz bandwidth for the corresponding magnetic coil inductance of 13 mH. The bode plot of the servo amplifier is shown in Figure A.10. Transfer function of the servo amplifier can be approximated by

$$G_{amp}(s) = \frac{I_{out}(s)}{V_{in}(s)} = \frac{0.5(2\pi \times 1600)^2}{s^2 + 2(0.5)(2\pi \times 1600)s + (2\pi \times 1600)^2} \quad (\text{A.1})$$

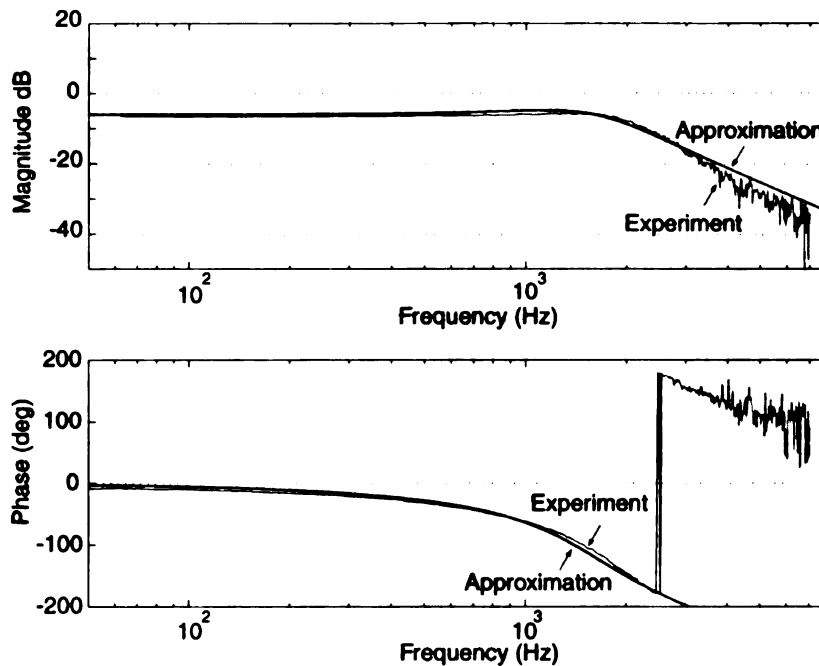


Figure A.10. Bode plot of servo amplifier



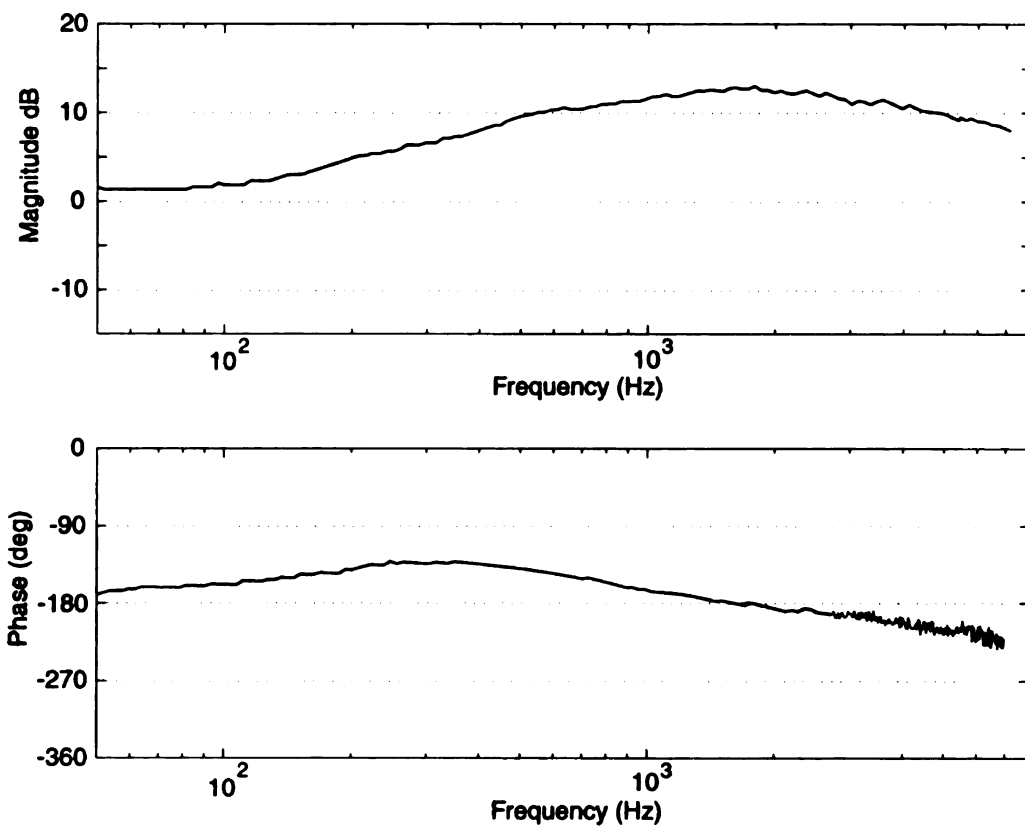


Figure A.12. Bode plot of analog PD controller  $V_{out}(S)/V_{in}(s)$

## **A.6 Radial Position Sensor**

The magnetic bearing assembly used in the experiment is supplied by Revolve Technologies Inc. It includes radial position sensors and the magnetic coil actuators. User manual describing the sensor-actuator of the Revolve's magnetic bearing system is provided in reference [29]. The important characteristics of the sensors can be summarized as follows. The sensors are inductive bridge type. They are mounted on a ring that allows concentric mounting in the magnetic bearing assembly. A pair of inductive sensors connected in series, looking at opposing sides of shaft. The inductance of each sensor varies inversely as the gap between the sensor and the journal. The sensor together with the signal conditioning system has the bandwidth of about  $10\text{ kHz}$ .

## **A.7 Digital Signal Processors**

The Digital Signal Processor package for the implementation of the primary control algorithm is manufactured by dSPACE. The package includes

1. DS1003 DSP Board : This DSP is based on TMS320C40 floating-point codes and has the on-board memory of 768 KWords.
2. DS2001 A/D Board: The board has 5 A/D channels capable of simultaneous sample and hold with 16 bit resolution.
3. DS2101 D/A Board: The board has 5 D/A boards capable of simultaneous sample and hold with 16 bit resolution.
4. dSPACE Tools Software : The software is version 2.1 that requires the TI C-Compiler version 4.7 and Matlab/Simulink-R11. The software is capable of implementing the control algorithms constructed on Simulink to the DSP Board. The software can display and record both the variables and time histories. It also permits changing of parameters on-line.

The above dSPACE boards are slotted into the ISA buses of a standard PC with Windows NT 4.0 as the operating system.

Another DSP package, product of Integrated Motions, model MX31 was utilized to generate the geometric center based on manual identification. The MX31 communicates with a PC through serial port. It requires Windows 95, Matlab version 4.2c.1 and Simulink version 1.3c.

## A.8 Absolute Encoder

An optical-rotary encoder, model CP-550-08AN, manufactured by Computer Optical Products Inc., is used to track the angular position of the rotor. As shown in Figure A.1, the encoder is attached to left-tip of the rotor using a torsionally rigid coupling. The encoder has the resolution of 8 bits with a linear-analog output of 10 V per revolution. We arrange the encoder such that  $0^\circ$  angle position generates 0V. In order to generate smooth  $\sin(\omega t)$  and  $\cos(\omega t)$  functions on a DSP, the Simulink block diagram below was used.

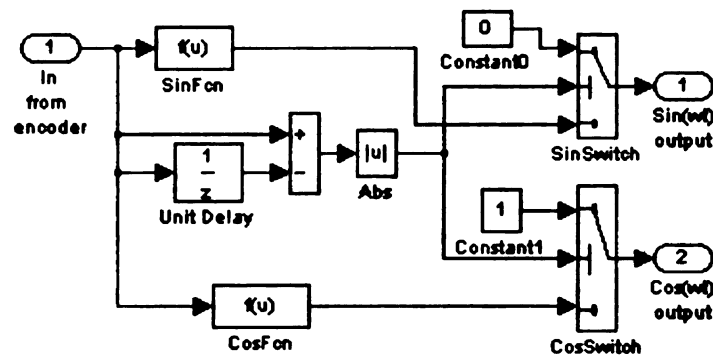


Figure A.13. Simulink block diagram for the absolute encoder

## APPENDIX B

### Analysis of Persistently Exciting Condition

Definition of Persistency of Excitation (PE) [25, 32]:

A vector valued  $\mathbf{u} \in \mathfrak{R}^n$  is said to be persistently exciting (PE), if there exists constants  $T_o, \alpha_1, \alpha_2 > 0$  such that

$$\alpha_2 \mathbf{I} \geq \frac{1}{T_o} \int_t^{t+T_o} \mathbf{u}^T \mathbf{u} d\tau \geq \alpha_1 \mathbf{I}, \quad \forall t > 0 \quad (\text{B.1})$$

where  $\mathbf{I}$  is the identity matrix,  $\mathbf{I} \in \mathfrak{R}^{n \times n}$ . Alternatively, the above definition of PE means that the matrix  $\mathbf{Q} \triangleq \frac{1}{T_o} \int_t^{t+T_o} \mathbf{u}^T \mathbf{u} d\tau$  is bounded and positive definite.

For the sake of brevity, without loss of generality, we consider up to the second harmonic components to prove the PE conditions. There are several ways to determine the positive definiteness of a matrix [26] such as:

1. Use the Sylvester's Criterion for Positive Definiteness:

A necessary and sufficient condition for a real symmetric matrix  $\mathbf{A} \in \mathfrak{R}^{n \times n}$  to be positive definite is that the determinant of  $\mathbf{A}$  be positive and the successive principal minors of the determinant of  $\mathbf{A}$  be positive the all principal minors are positive; that is, we must have

$$\begin{aligned} \mathbf{A}_1 \triangleq a_{11} > 0, \quad \mathbf{A}_2 \triangleq \begin{vmatrix} a_{11} & a_{12} \\ a_{21} & a_{22} \end{vmatrix} \geq 0, \\ \mathbf{A}_3 \triangleq \begin{vmatrix} a_{11} & a_{12} & a_{13} \\ a_{21} & a_{22} & a_{23} \\ a_{31} & a_{32} & a_{33} \end{vmatrix} > 0, \quad \dots, \quad \mathbf{A}_n \triangleq |\mathbf{A}| > 0 \end{aligned} \quad (\text{B.2})$$

2. Find the minimum eigenvalue  $\lambda_{min}$  of the matrix:

If  $\text{Re}[\lambda_{min}(A)] > 0$  then the matrix  $A$  is positive definite.

The Sylvester's criterion is useful to find the analytical conditions that guarantee positive definiteness of a matrix, in particular when the matrix has few nonzero off-diagonal terms. For a large matrix with many non-zero off-diagonal terms, finding the minimum eigenvalue numerically may become more practical.

## B.1 ASRC: Equation 3.14

From Eq.(2.23) we can write

$$\mathbf{Y}_m = \begin{pmatrix} \sqrt{\sigma_0} \\ \sqrt{\sigma_1} \sin(\omega t) \\ \sqrt{\sigma_1} \cos(\omega t) \\ \sqrt{\sigma_2} \sin(2\omega t) \\ \sqrt{\sigma_2} \cos(2\omega t) \end{pmatrix} \quad (\text{B.3})$$

where  $\sigma_i \triangleq [K_s + m(i\omega)^2]^2 > 0$  for  $i=0, 1$  and  $2$ . In this case  $\sigma_i$  is constant. By taking  $T_o = \frac{2\pi}{\omega}$ , the middle term of Eq.(3.14) becomes

$$\frac{\omega}{2\pi} \int_t^{t+\frac{2\pi}{\omega}} \mathbf{Y}_m \mathbf{Y}_m^T d\tau = \frac{1}{2} \begin{pmatrix} 2\sigma_0 & 0 & 0 & 0 & 0 \\ 0 & \sigma_1 & 0 & 0 & 0 \\ 0 & 0 & \sigma_1 & 0 & 0 \\ 0 & 0 & 0 & \sigma_2 & 0 \\ 0 & 0 & 0 & 0 & \sigma_2 \end{pmatrix} \triangleq \mathbf{Q} \quad (\text{B.4})$$

It is clear that  $\mathbf{Q}$  is bounded. We can easily verify using the Sylvester's criterion that  $\mathbf{Q}$  is positive definite. This concludes the proof that  $\mathbf{Y}_m$  is PE.

## B.2 SRUC Using Multiple Speeds: Equation 4.25

From Eq.(4.22)

$$\mathbf{Y}_E = \begin{pmatrix} \sqrt{\sigma_0} \\ \sqrt{\sigma_2} \sin(2\omega t) \\ \sqrt{\sigma_2} \cos(2\omega t) \end{pmatrix} \quad (\text{B.5})$$

where  $\sigma_i \triangleq [K_s + m(i\omega)^2]^2 > 0$  for  $i=0$  and  $2$ . In this case  $K_s$  is constant. By taking  $T_o = \frac{2\pi}{\omega}$ , the middle term of Eq.(4.25) becomes

$$\frac{\omega}{2\pi} \int_t^{t+\frac{2\pi}{\omega}} \mathbf{Y}_E \mathbf{Y}_E^T d\tau = \frac{1}{2} \begin{pmatrix} 2\sigma_0 & 0 & 0 \\ 0 & \sigma_2 & 0 \\ 0 & 0 & \sigma_2 \end{pmatrix} \triangleq \mathbf{Q} \quad (\text{B.6})$$

$\mathbf{Q}$  is bounded and positive definite. This concludes the proof that  $\mathbf{Y}_E$  is PE.

### B.3 SRUC-BCE: Equation 5.41

In this case  $K_s$  varies according to  $K_s = K_s^* + \xi_s \sin(\omega_e t) > 0$  where  $\xi_s \triangleq \frac{8ki_{10}A}{l^3} > 0$  is the resulting amplitude of variation in bearing stiffness and  $\omega_e \triangleq 2\pi f_e$  is the frequency of excitation. The Eq.(5.40) can be written as

$$\mathbf{Y}_{mu} = \begin{pmatrix} \sqrt{\sigma_0^*} + \xi_s \sin(\omega_e t) \\ [\sqrt{\sigma_1^*} + \xi_s \sin(\omega_e t)] \sin(\omega t) \\ [\sqrt{\sigma_1^*} + \xi_s \sin(\omega_e t)] \cos(\omega t) \\ [\sqrt{\sigma_2^*} + \xi_s \sin(\omega_e t)] \sin(2\omega t) \\ [\sqrt{\sigma_2^*} + \xi_s \sin(\omega_e t)] \cos(2\omega t) \\ -m\omega^2 \sin(\omega t) \\ -m\omega^2 \cos(\omega t) \end{pmatrix} \quad (\text{B.7})$$

where  $\sigma_i^* \triangleq [K_s^* + m(i\omega)^2]^2 > 0$  for  $i = 1$  and  $2$ . We can also write

$$\mathbf{Y}_{mu} = \begin{pmatrix} \sqrt{\sigma_0^*} + \xi_s \sin(\omega_e t) \\ \sqrt{\sigma_1^*} \sin(\omega t) - \frac{1}{2}\xi_s \cos(\omega_{h1}t) + \frac{1}{2}\xi_s \cos(\omega_{l1}t) \\ \sqrt{\sigma_1^*} \sin(\omega t) + \frac{1}{2}\xi_s \sin(\omega_{h1}t) + \frac{1}{2}\xi_s \sin(\omega_{l1}t) \\ \sqrt{\sigma_2^*} \sin(2\omega t) - \frac{1}{2}\xi_s \cos(\omega_{h2}t) + \frac{1}{2}\xi_s \cos(\omega_{l2}t) \\ \sqrt{\sigma_2^*} \sin(2\omega t) + \frac{1}{2}\xi_s \sin(\omega_{h2}t) + \frac{1}{2}\xi_s \sin(\omega_{l2}t) \\ -m\omega^2 \sin(\omega t) \\ -m\omega^2 \cos(\omega t) \end{pmatrix} \quad (\text{B.8})$$

where  $\omega_{hi} = (\omega_e + i\omega)$  and  $\omega_{li} = (\omega_e - i\omega)$  for  $i = 1$  and  $2$ .

Let the middle term of Eq.(5.39)

$$\mathbf{Q} \triangleq \frac{1}{T_o} \int_t^{t+T_o} \mathbf{Y}_{mu} \mathbf{Y}_{mu}^T d\tau \quad (\text{B.9})$$

The structure of  $\mathbf{Q}$  depends on the value  $\omega_e$  relative to the value of  $\omega$ . We can calculate  $\mathbf{Q}$  by letting  $T_o$  as the period in which all signals of different frequencies in the regressor vector  $\mathbf{Y}_{mu}$  complete their full cycle. In the following cases, we define  $\sigma_i \triangleq \sigma_i^* + \frac{1}{2}\xi_s^2 = [K_s^* + m(i\omega)^2]^2 + \frac{1}{2}\xi_s^2 > 0$  for  $i = 0, 1$  and  $2$ ; and  $\zeta \triangleq m\omega^2 \sqrt{\sigma_1^*} > 0$ .

Case 1:  $0 < \omega_e < 2\omega$ ,  $\omega_e \neq \frac{1}{2}\omega$ ,  $\omega_e \neq \omega$ ,  $\omega_e \neq \frac{3}{2}\omega$

$$\mathbf{Q} = \frac{1}{2} \begin{pmatrix} 2\sigma_0 & 0 & 0 & 0 & 0 & 0 & 0 \\ 0 & \sigma_1 & 0 & 0 & 0 & -\zeta & 0 \\ 0 & 0 & \sigma_1 & 0 & 0 & 0 & -\zeta \\ 0 & 0 & 0 & \sigma_2 & 0 & 0 & 0 \\ 0 & 0 & 0 & 0 & \sigma_2 & 0 & 0 \\ 0 & -\zeta & 0 & 0 & 0 & m^2\omega^4 & 0 \\ 0 & 0 & -\zeta & 0 & 0 & 0 & m^2\omega^4 \end{pmatrix} \quad (\text{B.10})$$

Let  $\mathbf{Q}_i$ ,  $i = 1, 2, \dots, 7$  denote the determinants of the upper left square submatrices of  $\mathbf{Q}$ . Using the Sylvester's criterion shown in Eq.(B.2), we can find that

$$\begin{aligned} \mathbf{Q}_1 &= \sigma_0 > 0, & \mathbf{Q}_2 &= \sigma_0\sigma_1 > 0, & \mathbf{Q}_3 &= \sigma_0\sigma_1^2 > 0, & \mathbf{Q}_4 &= \sigma_0\sigma_1^2\sigma_2 > 0, \\ \mathbf{Q}_5 &= \sigma_0\sigma_1^2\sigma_2^2 > 0, & \mathbf{Q}_6 &= \frac{1}{4}m^2\omega^4\xi_s^2\sigma_0\sigma_1\sigma_2^2 > 0, & \mathbf{Q}_7 &= \frac{1}{8}m^4\omega^8\xi_s^4\sigma_0\sigma_2^2 > 0 \end{aligned}$$

Thus, we can conclude that  $\mathbf{Q}$  is a positive definite matrix and  $\mathbf{Y}_{mu}$  is PE. In this case, ones may also recognize that in general  $\mathbf{Y}_{mu}$  is PE since for  $\mathbf{Q} \in \mathbb{R}^{n \times n}$  we can easily find that  $\mathbf{Q}_i > 0$  for  $i = 1, 2, \dots, n$ .

Case 2:  $\omega_e = \frac{1}{2}\omega$

$$\mathbf{Q} = \frac{1}{2} \begin{pmatrix} 2\sigma_0 & 0 & -\frac{1}{2}\xi_s^2 & 0 & 0 & 0 & 0 \\ 0 & \sigma_1 & 0 & -\frac{1}{4}\xi_s^2 & 0 & -\zeta & 0 \\ -\frac{1}{2}\xi_s^2 & 0 & \sigma_1 & 0 & -\frac{1}{4}\xi_s^2 & 0 & -\zeta \\ 0 & -\frac{1}{4}\xi_s^2 & 0 & \sigma_2 & 0 & 0 & 0 \\ 0 & 0 & -\frac{1}{4}\xi_s^2 & 0 & \sigma_2 & 0 & 0 \\ 0 & -\zeta & 0 & 0 & 0 & m^2\omega^4 & 0 \\ 0 & 0 & -\zeta & 0 & 0 & 0 & m^2\omega^4 \end{pmatrix} \quad (\text{B.11})$$

Using the Sylvester's criterion, we can find that

$$\mathbf{Q}_1 = \sigma_0 > 0, \quad \mathbf{Q}_2 = \sigma_0\sigma_1 > 0$$

$$\mathbf{Q}_3 = \frac{1}{2}\sigma_1 \left( 2\sigma_0 \left[ (K_s^* + m\omega^2)^2 + \frac{1}{2}\xi_s^2 \right] - \frac{1}{4}\xi_s^4 \right) > 0 \quad \text{since } \sigma_0 > \frac{1}{4}\xi_s^2$$

$$\mathbf{Q}_4 = \frac{1}{2} \left( \sigma_2 \left[ (K_s^* + m\omega^2)^2 + \frac{1}{2}\xi_s^2 \right] - \frac{1}{16}\xi_s^4 \right) \times \\ \left( 2\sigma_0 \left[ (K_s^* + m\omega^2)^2 + \frac{1}{2}\xi_s^2 \right] - \frac{1}{4}\xi_s^4 \right) > 0 \quad \text{since } \sigma_2 > \frac{1}{8}\xi_s^2 \text{ and } \sigma_0 > \frac{1}{4}\xi_s^2$$

$$\mathbf{Q}_5 = \frac{1}{2} \left( \sigma_2 \left[ (K_s^* + m\omega^2)^2 + \frac{1}{2}\xi_s^2 \right] - \frac{1}{16}\xi_s^4 \right) \times \mathbf{Q}_{5a} > 0 \\ \text{since}$$

$$\mathbf{Q}_{5a} = 20(K_s^*)^5 m\omega^2 + 66(K_s^*)^4 m^2\omega^4 + 80(K_s^*)^3 m^3\omega^6 + \\ 32(K_s^*)^2 m^4\omega^8 + 16\xi_s^2 m^4\omega^8 + \frac{9}{2}\xi_s^4 m^2\omega^4 + \\ 2(K_s^*)^6 + \frac{1}{16}\xi_s^6 + 20(K_s^*)^3 m\omega^2\xi_s^2 + \frac{9}{8}(K_s^*)^2\xi_s^4 + \\ 50(K_s^*)^2 m^2\omega^4\xi_s^2 + 40 m^2 m^3\omega^6 K_s^* + 3\xi_s^4 K_s^* m\omega^2 + 3(K_s^*)^4\xi_s^2 > 0 \\ \text{and } \sigma_2 > \frac{1}{8}\xi_s^2$$

$$\mathbf{Q}_6 = \frac{1}{2}\mathbf{Q}_{6a}\mathbf{Q}_{5a} > 0$$

$$\text{where } \mathbf{Q}_{6a} = \frac{1}{2}(K_s^*)^2 m^2\omega^4\xi_s^2 + 4\xi_s^2 m^3\omega^6 K_s^* + 8\xi_s^2 m^4\omega^8 + \frac{3}{16}\xi_s^4 m^2\omega^4 > 0$$

$$\mathbf{Q}_7 = \frac{1}{2}\mathbf{Q}_{6a}\mathbf{Q}_{7a} > 0$$

$$\text{where } \mathbf{Q}_{7a} = 4m^4\omega^8\xi_s^4 + 16m^4\omega^8(K_s^*)^2\xi_s^2 + \frac{1}{16}m^2\omega^4\xi_s^6 + (K_s^*)^4 m^2\omega^4\xi_s^2 + \\ 8(K_s^*)^3 m^3\omega^6\xi_s^2 + \frac{5}{8}m^2\omega^4(K_s^*)^2\xi_s^4 + 2m^3\omega^6 K_s^*\xi_s^4 > 0$$

Therefore, we can conclude that  $\mathbf{Q}$  is a positive definite matrix and  $\mathbf{Y}_{\mathbf{mu}}$  is PE.

Case 3:  $\omega_e = \frac{3}{2}\omega$

$$\mathbf{Q} = \frac{1}{2} \begin{pmatrix} 2\sigma_0 & 0 & 0 & 0 & 0 & 0 & 0 \\ 0 & \sigma_1 & 0 & \frac{1}{4}\xi_s^2 & 0 & -\zeta & 0 \\ 0 & 0 & \sigma_1 & 0 & -\frac{1}{4}\xi_s^2 & 0 & -\zeta \\ 0 & \frac{1}{4}\xi_s^2 & 0 & \sigma_2 & 0 & 0 & 0 \\ 0 & 0 & -\frac{1}{4}\xi_s^2 & 0 & \sigma_2 & 0 & 0 \\ 0 & -\zeta & 0 & 0 & 0 & m^2\omega^4 & 0 \\ 0 & 0 & -\zeta & 0 & 0 & 0 & m^2\omega^4 \end{pmatrix} \quad (\text{B.12})$$

Using the Sylvester's criterion, we can find that

$$\mathbf{Q}_1 = \sigma_0 > 0, \quad \mathbf{Q}_2 = \sigma_0\sigma_1 > 0, \quad \mathbf{Q}_3 = \sigma_0\sigma_1^2 > 0$$

$$\mathbf{Q}_4 = \frac{\sigma_0\sigma_1}{2}Q_{4a} > 0$$

$$\text{where } Q_{4a} = \left( \sigma_2 \left[ (K_s^* + m\omega^2)^2 + \frac{1}{2}\xi_s^2 \right] - \frac{1}{16}\xi_s^4 \right) > 0 \quad \text{since } \sigma_2 > \frac{1}{8}\xi_s^2$$

$$\mathbf{Q}_5 = \frac{\sigma_0}{2}Q_{4a} > 0$$

$$\mathbf{Q}_6 = \sigma_0Q_{4a}Q_{6a} > 0$$

$$\text{where } Q_{6a} = \frac{1}{2}(K_s^*)^2m^2\omega^4\xi_s^2 + 4\xi_s^2m^3\omega^6K_s^* + 8\xi_s^2m^4\omega^8 + \frac{3}{16}\xi_s^4m^2\omega^4 > 0$$

$$\mathbf{Q}_7 = \sigma_0Q_{6a} > 0$$

Therefore, we can conclude that  $\mathbf{Q}$  is a positive definite matrix and  $\mathbf{Y}_{\text{mu}}$  is PE.

Case 4: for  $\omega_e = 2\omega$ ,

$$\mathbf{Q} = \frac{1}{2} \begin{pmatrix} 2\sigma_0 & 0 & 0 & Q_{02} & 0 & 0 & 0 \\ 0 & \sigma_1 & \xi_s \sigma_1^* & 0 & 0 & -\zeta & -Q_{1u} \\ 0 & \xi_s \sigma_1^* & \sigma_1 & 0 & 0 & -Q_{1u} & -\zeta \\ Q_{02} & 0 & 0 & \sigma_2^* + \frac{3}{4}\xi_s^2 & 0 & 0 & 0 \\ 0 & 0 & 0 & 0 & \sigma_2^* + \frac{1}{4}\xi_s^2 & 0 & 0 \\ 0 & -\zeta & -Q_{1u} & 0 & 0 & m^2\omega^4 & 0 \\ 0 & -Q_{1u} & -\zeta & 0 & 0 & 0 & m^2\omega^4 \end{pmatrix} \quad (\text{B.13})$$

where  $Q_{02} = \xi_s(\sqrt{\sigma_2^*} + \sqrt{\sigma_0^*})$ ,  $Q_{1u} = \frac{1}{2}\xi_s m\omega^2$

Using the Sylvester's criterion, we can also find that  $\mathbf{Q}$  is positive definite. The analytical proof here is omitted. The use of computer program with symbolic manipulation capability will show that  $\mathbf{Q}$  satisfies the Sylvester's criterion for positive definiteness. However, finding the eigenvalues numerically is more practical. We can easily find that the minimum eigenvalue  $\lambda_{min} > 0$ . Therefore,  $\mathbf{Y}_{mu}$  is PE.

Case 5: for  $\omega_e = \omega$ ,

$$\mathbf{Q} = \frac{1}{2} \begin{pmatrix} 2\sigma_0 & Q_{01} & 0 & 0 & -\frac{1}{2}\xi_s^2 & -Q_{1u} & 0 \\ Q_{01} & \sigma_1^* + \frac{3}{4}\xi_s^2 & 0 & 0 & -Q_{12} & -\zeta & 0 \\ 0 & 0 & \sigma_1^* + \frac{1}{4}\xi_s^2 & 0 & 0 & 0 & -\zeta \\ 0 & 0 & 0 & \sigma_2 & 0 & 0 & -Q_{1u} \\ -\frac{1}{2}\xi_s^2 & -Q_{12} & 0 & 0 & \sigma_2 & Q_{1u} & 0 \\ -Q_{1u} & -\zeta & 0 & 0 & Q_{1u} & m^2\omega^4 & 0 \\ 0 & 0 & -\zeta & -Q_{1u} & 0 & 0 & m^2\omega^4 \end{pmatrix} \quad (\text{B.14})$$

where  $Q_{01} = \xi_s(K_s^* + \sqrt{\sigma_1^*})$ ,  $Q_{1u} = \frac{1}{2}\xi_s m\omega^2$ , and  $Q_{12} = \frac{1}{2}\xi_s(\sqrt{\sigma_1^*} + \sqrt{\sigma_2^*})$ .

In this case, numerical evaluation shows that  $\mathbf{Q}$  has two eigenvalues at the origin. Therefore  $\mathbf{Y}_{mu}$  is not PE.

## APPENDIX C

### Parameter Convergence Using Averaging Method

The following two-times scale averaging method is adopted from Sastry and Bodson [32] for a system having a regressor vector.

#### C.1 Convergence Rate of ASRC

Consider the system in Chapter 3 of the form

$$\dot{\tilde{\phi}} = \Gamma \bar{\mathbf{Y}}_m \bar{e} \quad (\text{C.1})$$

$$M\ddot{\bar{x}} + C\dot{\bar{x}} + K\bar{x} = -\mathbf{Y}_m^T \tilde{\phi} \quad (\text{C.2})$$

$$\dot{\bar{e}} = \dot{\bar{x}} + \lambda \bar{x} \quad (\text{C.3})$$

where  $\tilde{\phi}, \bar{\mathbf{Y}}_m, \mathbf{Y}_m \in \mathfrak{R}^{2n+1}$ ,  $\bar{e}, \bar{x} \in \mathfrak{R}$ , and  $M, C, K, \lambda > 0$ . The above three expressions are obtained from Eqs.(3.19), (3.26) and (2.22) respectively.

In short, we can denote Eqs.(C.1) and (C.2) as

$$\dot{\bar{e}} = \frac{s + \lambda}{Ms^2 + Cs + K} (-\mathbf{Y}_m^T \tilde{\phi}) = -G(s)[\mathbf{Y}_m^T \tilde{\phi}] \triangleq -\bar{G}(\mathbf{Y}_m^T \tilde{\phi}) \quad (\text{C.4})$$

where  $\bar{G}(\cdot)$  is a signal vector and  $G(s)$  is an SPR transfer function

$$G(s) = \frac{s + \lambda}{Ms^2 + Cs + K} \quad (\text{C.5})$$

and Eq.(C.1) becomes

$$\dot{\tilde{\phi}} = -\Gamma \bar{\mathbf{Y}}_m [\bar{G}(\mathbf{Y}_m^T \tilde{\phi})] \quad (\text{C.6})$$

When  $\Gamma \rightarrow 0$ ,  $\tilde{\phi}(t)$  varies slowly compared to  $\bar{e}$ , the time scales of their variation become separated.  $\tilde{\phi}(t)$  is called the slow state,  $\bar{e}(t)$  the fast state and the system in Equations (C.1) to (C.3) a two-time scale system. In the limit as  $\Gamma \rightarrow 0$ ,  $\tilde{\phi}(t)$  may be considered frozen in Equations (C.2) and (C.3), so that

$$\bar{G}(\mathbf{Y}_m^T \tilde{\phi}) = \bar{G}(\mathbf{Y}_m^T \tilde{\phi}) \quad (\text{C.7})$$

The result of averaging theory, Eq.(C.6) therefore can be approximated by

$$\dot{\tilde{\phi}}_{av} = -\Gamma \mathbf{AVG}\{\bar{\mathbf{Y}}_m \bar{G}(\mathbf{Y}_m^T)\} \tilde{\phi}_{av} \quad (\text{C.8})$$

where

$$\text{AVG}\{\bar{\mathbf{Y}}_m \bar{G}(\mathbf{Y}_m^T)\} \triangleq \frac{1}{T} \int_{t_0}^{t_0+T} \bar{\mathbf{Y}}_m \bar{G}(\mathbf{Y}_m^T) dt \quad (\text{C.9})$$

where  $T = \frac{2\pi}{\omega}$ . The function  $\text{AVG}\{\bar{\mathbf{Y}}_m \bar{G}(\mathbf{Y}_m^T)\}$  is commonly written as  $\mathbf{R}(0)$  and called as the correlation matrix.

For simplicity, we will consider  $n$  up to the second harmonic; thus, we use  $\mathbf{Y}_m$  defined in Eq.(B.3). Furthermore, from the definition in Eq.(3.20), we can write

$$\bar{\mathbf{Y}}_m = \begin{pmatrix} \sqrt{\bar{\sigma}_0} \\ \sqrt{\bar{\sigma}_1} \sin(\omega t) \\ \sqrt{\bar{\sigma}_1} \cos(\omega t) \\ \sqrt{\bar{\sigma}_2} \sin(2\omega t) \\ \sqrt{\bar{\sigma}_2} \cos(2\omega t) \end{pmatrix} \quad (\text{C.10})$$

where  $\bar{\sigma}_i^* \triangleq [\bar{K}_i^* + \bar{m}(i\omega)^2]^2$ . We then obtain

$$\bar{G}(\bar{\mathbf{Y}}_m) = \begin{pmatrix} \frac{\lambda}{K} \sqrt{\bar{\sigma}_0} \\ |G(j\omega)| \sqrt{\bar{\sigma}_1} \sin(\omega t + \angle G(j\omega)) \\ |G(j\omega)| \sqrt{\bar{\sigma}_1} \cos(\omega t + \angle G(j\omega)) \\ |G(j2\omega)| \sqrt{\bar{\sigma}_2} \sin(2\omega t + \angle G(j2\omega)) \\ |G(j2\omega)| \sqrt{\bar{\sigma}_2} \cos(2\omega t + \angle G(j2\omega)) \end{pmatrix} \quad (\text{C.11})$$

The product of  $\bar{\mathbf{Y}}_m \bar{G}(\mathbf{Y}_m^T)$  may be expanded as the sum of products of sinusoids. Further, for  $i = 1$  and 2

$$\sin(i\omega t + \angle G(j i\omega)) = \sin(i\omega t) \cos(\angle G(j i\omega)) + \cos(i\omega t) \sin(\angle G(j i\omega)) \quad (\text{C.12})$$

$$\cos(i\omega t + \angle G(j i\omega)) = \cos(i\omega t) \cos(\angle G(j i\omega)) - \sin(i\omega t) \sin(\angle G(j i\omega)) \quad (\text{C.13})$$

Since the products of sinusoids at different frequencies have zero average, as do products of sin's with cos's of any frequency, we obtain

$$\mathbf{R}(0) = \begin{pmatrix} R_0 & 0 & 0 & 0 & 0 \\ 0 & R_1 & 0 & 0 & 0 \\ 0 & 0 & R_1 & 0 & 0 \\ 0 & 0 & 0 & R_2 & 0 \\ 0 & 0 & 0 & 0 & R_2 \end{pmatrix} \quad (\text{C.14})$$

where

$$R_0 = \frac{\lambda}{K} \sqrt{\bar{\sigma}_0} \sqrt{\sigma_0} \quad (\text{C.15})$$

$$R_1 = \frac{1}{2} \sqrt{\bar{\sigma}_1} \sqrt{\sigma_1} |G(j\omega)| \cos(\angle G(j\omega)) = \frac{1}{2} \sqrt{\bar{\sigma}_1} \sqrt{\sigma_1} \mathbf{Re}\{G(j\omega)\} \quad (\text{C.16})$$

$$R_2 = \frac{1}{2} \sqrt{\bar{\sigma}_2} \sqrt{\sigma_2} |G(j2\omega)| \cos(\angle G(j2\omega)) = \frac{1}{2} \sqrt{\bar{\sigma}_2} \sqrt{\sigma_2} \mathbf{Re}\{G(j2\omega)\} \quad (\text{C.17})$$

Using the familiar SPR condition, we know  $G(s)$  is real for real  $s$  and  $\mathbf{Re}\{G(j\omega)\} > 0, \forall \omega \in (-\infty, \infty)$ . Therefore  $R_0, R_1, R_2 > 0, \forall \omega \in (-\infty, \infty)$ . The final results are tabulated in Table 3.1.

## C.2 Convergence Rate of SRUC-BCE

Consider the system from Chapter 5 of the form

$$\dot{\tilde{\phi}} = \Gamma \mathbf{Y}_m \bar{e} \quad (\text{C.18})$$

$$\dot{\tilde{\phi}}_u = \Gamma_u \mathbf{Y}_u \bar{e} \quad (\text{C.19})$$

$$m(1 - \Delta)\dot{\bar{e}} + (c - \frac{1}{2} m\dot{\Delta})\bar{e} = -\mathbf{Y}_m^T \tilde{\phi} + \mathbf{Y}_u^T \tilde{\phi}_u \quad (\text{C.20})$$

where  $\tilde{\phi}, \mathbf{Y}_m \in \mathfrak{R}^3; \tilde{\phi}_u, \mathbf{Y}_u \in \mathfrak{R}^2; \bar{e}, \bar{x} \in \mathfrak{R}; \Delta, c, \lambda > 0$ ; and  $(c - \frac{1}{2} m\dot{\Delta}) > 0$ . The above expressions are obtained from Eqs.(5.25), (5.26), and (5.36). We may write these equations as

$$\bar{e} = \frac{-\mathbf{Y}_{mu}^T \tilde{\phi}_{mu}}{m(1 - \Delta)s + (c - \frac{1}{2} m\dot{\Delta})} = -G(s)[\mathbf{Y}_{mu}^T \tilde{\phi}_{mu}] \triangleq -\bar{G}(\mathbf{Y}_{mu}^T \tilde{\phi}_{mu}) \quad (\text{C.21})$$

where  $\mathbf{Y}_{mu}$  is given in Appendix B.3,  $\tilde{\phi}_{mu}^T = \begin{pmatrix} \tilde{\phi}^T & \tilde{\phi}_u^T \end{pmatrix}$  and  $G(s)$  is a time varying SPR transfer function

$$G(s) = \frac{1}{m(1 - \Delta)s + (c - \frac{1}{2} m\dot{\Delta})} \quad (\text{C.22})$$

For relative small variation of  $\Delta$  about its nominal value  $\Delta_0$ , we may approximate the above transfer function to

$$G_0(s) = \frac{1}{m(1 - \Delta_0)s + c} \quad (\text{C.23})$$

thus we can approximate  $\bar{e}$  in Eq.(C.21) by

$$\bar{e} \simeq -\bar{G}_0(\mathbf{Y}_{mu}^T \tilde{\phi}_{mu}) \quad (C.24)$$

and Eqs.(C.18) and (C.19) become

$$\dot{\tilde{\phi}}_{mu} \simeq -\Gamma_{mu} \bar{Y}_{mu} [\bar{G}_0(\mathbf{Y}_{mu}^T \tilde{\phi}_{mu})] \quad (C.25)$$

where

$$\Gamma_{mu} \triangleq \begin{pmatrix} \Gamma & 0 \\ 0 & -\Gamma_u \end{pmatrix} \quad (C.26)$$

By assuming  $\Gamma$  and  $\Gamma_u$  are relatively small,  $\phi_{mu}$  varies slowly compared to  $\bar{e}$ . Thus  $\phi_{mu}$  can be considered frozen in Eq.(C.21), so that

$$\bar{G}_0(\mathbf{Y}_m^T \tilde{\phi}) = \bar{G}_0(\mathbf{Y}_m^T) \tilde{\phi} \quad (C.27)$$

The result of averaging theory, Eq.(C.25) therefore can be approximated by

$$\dot{\tilde{\phi}}_{av} = -\Gamma_{mu} \text{AVG}\{\mathbf{Y}_{mu} \bar{G}_0(\mathbf{Y}_{mu}^T)\} \tilde{\phi}_{av} \quad (C.28)$$

where

$$\text{AVG}\{\mathbf{Y}_{mu} \bar{G}_0(\mathbf{Y}_{mu}^T)\} \triangleq \frac{1}{T} \int_{t_0}^{t_0+T} \mathbf{Y}_{mu} \bar{G}_0(\mathbf{Y}_{mu}^T) dt = \mathbf{R}(0) \quad (C.29)$$

In the following we consider several cases of  $\omega_e$  relative to  $\omega$ .

Case 1:  $0 < \omega_e < \omega$ ,  $\omega_e \neq \frac{1}{2}\omega$ ,  $\omega_e \neq \omega$ ,  $\omega_e \neq \frac{3}{2}\omega$

$$\mathbf{R}(0) = \begin{pmatrix} R_0 & 0 & 0 & 0 & 0 & 0 & 0 \\ 0 & R_1 & 0 & 0 & 0 & -R_{1u} & 0 \\ 0 & 0 & R_1 & 0 & 0 & 0 & -R_{1u} \\ 0 & 0 & 0 & R_2 & 0 & 0 & 0 \\ 0 & 0 & 0 & 0 & R_2 & 0 & 0 \\ 0 & -R_{1u} & 0 & 0 & 0 & R_u & 0 \\ 0 & 0 & -R_{1u} & 0 & 0 & 0 & R_u \end{pmatrix} \quad (C.30)$$

where

$$R_0 = \frac{\sigma_0^*}{c} + \frac{\frac{1}{2}\xi_s^2}{m(1 - \Delta_0)\omega_e + c} \quad (C.31)$$

$$R_i = \frac{\frac{1}{2}\sigma_i^*}{m(1 - \Delta_0)(i\omega) + c} + \frac{\frac{1}{4}\xi_s}{m(1 - \Delta_0)(\omega_{hi}) + c} + \frac{\frac{1}{4}\xi_s}{m(1 - \Delta_0)(\omega_{li}) + c} \quad (\text{C.32})$$

for  $i = 1$  and  $2$ .

$$R_u = \frac{\frac{1}{2}m^2\omega^4}{m(1 - \Delta_0)\omega + c} \quad (\text{C.33})$$

$$R_{1u} = \frac{\frac{1}{2}\sqrt{\sigma_1^*}m\omega^2}{m(1 - \Delta_0)\omega + c} \quad (\text{C.34})$$

Case 2:  $\omega_e = \frac{1}{2}\omega$

$$\mathbf{R}(0) = \begin{pmatrix} R_0 & 0 & -R_{01} & 0 & 0 & 0 & 0 \\ 0 & R_1 & 0 & -R_{12} & 0 & -R_{1u} & 0 \\ -R_{01} & 0 & R_1 & 0 & -R_{12} & 0 & -R_{1u} \\ 0 & -R_{12} & 0 & R_2 & 0 & 0 & 0 \\ 0 & 0 & -R_{12} & 0 & R_2 & 0 & 0 \\ 0 & -R_{1u} & 0 & 0 & 0 & R_u & 0 \\ 0 & 0 & -R_{1u} & 0 & 0 & 0 & R_u \end{pmatrix} \quad (\text{C.35})$$

where  $R_0, R_1, R_2, R_u$  and  $R_{1u}$  are defined in Eqs.(C.31) to (C.34) and

$$R_{01} = \frac{\frac{1}{4}\xi_s^2}{m(1 - \Delta_0)\omega_e + c} \quad (\text{C.36})$$

$$R_{12} = \frac{\frac{1}{8}\xi_s^2}{m(1 - \Delta_0)\omega_e + c} \quad (\text{C.37})$$

Case 3:  $\omega_e = \frac{3}{2}\omega$

$$\mathbf{R}(0) = \begin{pmatrix} R_0 & 0 & 0 & 0 & 0 & 0 & 0 \\ 0 & R_1 & 0 & R_{12} & 0 & -R_{1u} & 0 \\ 0 & 0 & R_1 & 0 & -R_{12} & 0 & -R_{1u} \\ 0 & R_{12} & 0 & R_2 & 0 & 0 & 0 \\ 0 & 0 & -R_{12} & 0 & R_2 & 0 & 0 \\ 0 & -R_{1u} & 0 & 0 & 0 & R_u & 0 \\ 0 & 0 & -R_{1u} & 0 & 0 & 0 & R_u \end{pmatrix} \quad (\text{C.38})$$

where  $R_0, R_1, R_2, R_u$  and  $R_{1u}$  are defined in Eqs.(C.31) to (C.34) and

$$R_{12} = \frac{\frac{1}{8}\xi_s^2}{m(1 - \Delta_0)\frac{\omega}{2} + c} \quad (\text{C.39})$$

## APPENDIX D

### Passivity

We adopt the passivity definitions from references [12, 13, 18] in order to evaluate the robustness of our adaptive control systems in the present of uncertain plant parameters.

Consider the systems of the form

$$\begin{aligned}\dot{x} &= f(x, t) + g(x, t)u \\ y &= h(x, t)\end{aligned}\tag{D.1}$$

with  $x \in \mathfrak{R}^n$ ,  $y \in \mathfrak{R}^m$ ,  $u \in \mathfrak{R}^m$ , and  $f, g, h$  continuous in  $t$  and smooth in  $x$ . Suppose  $f(0, t) = 0$  and  $h(0, t) = 0$  for all  $t \geq 0$ .

**Definition D.1** *The system (D.1) is said to be passive if there exists a continuous non-negative ("storage") function  $W$  which satisfies  $W(0, t) = 0, \forall t_0 \geq 0$  such that for all  $x, u \in \mathfrak{R}^n \times \mathfrak{R}^m$  and  $t \geq t_0 \geq 0$*

$$\int_{t_0}^t y^T(\tau)u(\tau)d\tau \geq W(x(t), t) - W(x(t_0), t_0)\tag{D.2}$$

**Definition D.2** *The system (D.1) is said to be strictly passive if there exist a continuous non-negative (storage) function  $W$  and a positive definite function (dissipation rate)  $\psi \in \mathfrak{R}^n$  such that for all  $x, u \in \mathfrak{R}^m \times \mathfrak{R}^n$  and  $t \geq t_0 \geq 0$ ,*

$$\int_{t_0}^t y^T(\tau)u(\tau)d\tau \geq W(x(t), t) - W(x(t_0), t_0) + \int_{t_0}^t \psi(x(\tau))d\tau\tag{D.3}$$

**Lemma D.1** *Suppose the system (D.1) is strictly passive. If  $W$  is positive definite, radially unbounded, and decrescent, that is, if there exist class  $K_\infty$  functions  $\alpha_1$  and  $\alpha_2$  such that  $\alpha_1(|x|) \leq W(x, t) \leq \alpha_2(|x|), \forall (x, t) \in \mathfrak{R}^n \times \mathfrak{R}_+$ , then, for  $u \equiv 0$ , the equilibrium  $x = 0$  of (D.1) is globally uniformly asymptotically stable. The proof can be obtained in reference [18].*

Using the block diagram in Figure D.1 and the definitions

$$H_1 : \begin{aligned} \dot{x} &= f_1(x, t) + g_2(x, t)u \\ y_1 &= h_1(x, t) \end{aligned} \quad (D.4)$$

$$H_2 : \begin{aligned} \dot{x} &= f_2(x, t) + g_2(x, t)u \\ y_2 &= h_2(x, t) \end{aligned} \quad (D.5)$$

we can state the following theorem.

**Theorem D.1** *If the system  $H_1$  is strictly passive with storage function  $W_1$  and dissipation rate  $\psi_1$  independent of  $x_2$  and the system  $H_2$  is passive with storage function  $W_2$  independent of  $x_1$ . Then the equilibrium point  $x = 0$  is globally uniformly stable and  $\lim_{t \rightarrow \infty} = 0$ . The proof can be obtained in references [13, 18].*

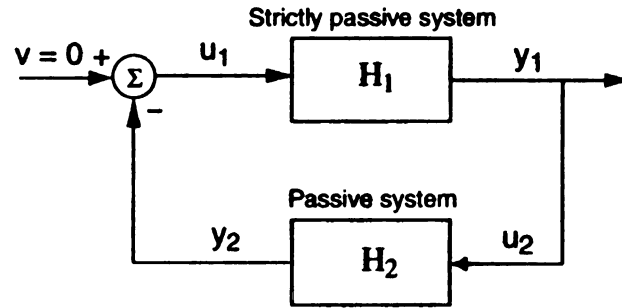


Figure D.1. Feedback configuration for passivity analysis

The following result is due to Kalman-Yakubovich lemma that shows the closeness of the Lyapunov stability and passivity concepts.

**Definition D.3** *A linear time varying system*

$$H_1 : \begin{aligned} \dot{z} &= \mathbf{A}(t)z + \mathbf{B}(t)u_1 \\ y_1 &= \mathbf{C}(t)z \end{aligned} \quad (D.6)$$

*is called strictly passive if it satisfies the following relations:*

$$\dot{P}(t) + P(t)\mathbf{A}(t) + \mathbf{A}^T(t)P(t) = -\mathbf{Q}(t) < 0 \quad (D.7)$$

$$P(t)\mathbf{B}(t) = \mathbf{C}^T(t) \quad (D.8)$$

for some uniformly bounded positive definite matrices  $P(t)$  and  $Q(t)$ .

For linear time-invariant systems, the following definition is commonly used to represent the strictly passive condition.

**Definition D.4** A rational transfer function  $G(s)$  is said to be positive real if  $G(s)$  is real for all real  $s$ , and  $\operatorname{Re}\{G(s)\} \geq 0$  for all  $\operatorname{Re}\{s\} \geq 0$ .

The following lemmas are used in the study of the effect of plant parameter uncertainties to the SRUC-BCE algorithm in Chapter 5.

**Lemma D.2** The system  $H_2$  that has  $u_2 = \bar{e}$  as the input and  $y_2 = \mathbf{Y}_m^T \tilde{\phi} - \mathbf{Y}_u^T \tilde{\phi}_u + \frac{\rho_m}{m} \mathbf{Y}_u^T \hat{\phi}_u$  as the output, obtained from Eq.(5.53) when  $m$  is uncertain, is passive for sufficiently small  $|\rho_m|$  and relatively small amplitude of bias current excitation.

**Proof:** To simplify the problem, we define new variables

$$\tilde{\phi}_{u\rho} \triangleq \begin{pmatrix} \tilde{p}_\rho \\ \tilde{q}_\rho \end{pmatrix} = \phi_u - \left(1 + \frac{\rho_m}{m}\right) \hat{\phi}_u \quad (\text{D.9})$$

Therefore the output equation can be written as  $y_2 = \mathbf{Y}_m^T \tilde{\phi} - \mathbf{Y}_u^T \tilde{\phi}_{u\rho}$  and the adaptation law in Eq.(5.47) become

$$\begin{aligned} \dot{\tilde{a}}_0 &= \gamma_0 K_s \bar{e} \\ \dot{\tilde{a}}_i &= \gamma_i [K_s + \bar{m}i^2\omega^2] \sin(i\omega t) \bar{e} \\ \dot{\tilde{b}}_i &= \gamma_i [K_s + \bar{m}i^2\omega^2] \cos(i\omega t) \bar{e}, \quad i = 1, 2, \dots, n \\ \dot{\tilde{p}}_\rho &= -\left(1 + \frac{\rho_m}{m}\right) \gamma_p \bar{m} \omega^2 \sin(\omega t) \bar{e} \\ \dot{\tilde{q}}_\rho &= -\left(1 + \frac{\rho_m}{m}\right) \gamma_q \bar{m} \omega^2 \cos(\omega t) \bar{e} \end{aligned}$$

It should be noted that  $K_s$  is time varying as shown in Eq.(5.22) and  $\rho_m$  is constant. For a sufficiently small  $|\rho_m|$ , we may assume  $\left(1 + \frac{\rho_m}{m}\right) > 0$  and  $\bar{m} > 0$ . We further define new variables

$$\begin{aligned} \rho_i(t) &= \frac{K_s + mi^2\omega^2}{\gamma_i(K_s + \bar{m}i^2\omega^2)} > 0 \quad \text{for } i = 0, 1, 2, \dots, n \\ \rho_p &= \frac{m}{\gamma_p \bar{m} \left(1 + \frac{\rho_m}{m}\right)} > 0 \quad \rho_q = \frac{m}{\gamma_q \bar{m} \left(1 + \frac{\rho_m}{m}\right)} > 0 \end{aligned}$$

For a relatively small bias current excitation we may assume that there exist a constant  $c_1$  such that  $\rho_i(t) > c_1$  for all  $t$ . Therefore, recalling the definition D.1 for a passive system we can obtain

$$\begin{aligned}
\int_0^t y_2 u_2 dt &= \int_0^t [\mathbf{Y}_m^T \tilde{\phi} - \mathbf{Y}_u^T \tilde{\phi}_{u\rho}] \bar{e} dt \\
&= \int_0^t K_s \tilde{a}_0 \bar{e} dt + \sum_{i=1}^n \left\{ \int_0^t (K_s + mi^2 \omega^2) [\tilde{a}_i \sin(i\omega t) \bar{e} + \tilde{b}_i \cos(i\omega t) \bar{e}] dt \right\} - \\
&\quad m\omega^2 \int_0^t \tilde{p} \sin(\omega t) \bar{e} dt - m\omega^2 \int_0^t \tilde{q} \cos(\omega t) \bar{e} dt \\
&= \int_0^t \rho_0 \tilde{a}_0 \dot{\tilde{a}}_0 dt + \sum_{i=1}^n \left\{ \int_0^t \rho_i [\tilde{a}_i \dot{\tilde{a}}_i + \tilde{b}_i \dot{\tilde{b}}_i] dt \right\} + \\
&\quad \rho_p \int_0^t \tilde{p}_\rho \dot{\tilde{p}}_\rho dt + \rho_q \int_0^t \tilde{q}_\rho \dot{\tilde{q}}_\rho dt \\
&> W[\tilde{\phi}(t), \phi_u(t), \hat{\phi}_u(t)] - W[\tilde{\phi}(0), \phi_u(0), \hat{\phi}_u(0)]
\end{aligned}$$

where

$$\begin{aligned}
W[\tilde{\phi}(t), \tilde{\phi}_u(t), \hat{\phi}_u(t)] &= \frac{c_1}{2} \tilde{a}_0^2(t) + \sum_{i=1}^n \frac{c_1}{2} [\tilde{a}_i^2(t) + \tilde{b}_i^2(t)] + \\
&\quad \frac{\rho_p}{2} \tilde{p}_\rho^2(t) + \frac{\rho_q}{2} \tilde{q}_\rho^2(t)
\end{aligned}$$

$$\begin{aligned}
W[\tilde{\phi}(0), \tilde{\phi}_u(0), \hat{\phi}_u(0)] &= \frac{c_1}{2} \tilde{a}_0^2(0) + \sum_{i=1}^n \frac{c_1}{2} [\tilde{a}_i^2(0) + \tilde{b}_i^2(0)] + \\
&\quad \frac{\rho_p}{2} \tilde{p}_\rho^2(0) + \frac{\rho_q}{2} \tilde{q}_\rho^2(0)
\end{aligned}$$

Since  $W[\tilde{\phi}(t), \tilde{\phi}_u(t), \hat{\phi}_u(t)]$  is a positive definite storage function, by definition D.1 the system  $H_2$  is passive.

**Lemma D.3** *The system  $H_2$  that has  $u_2 = \bar{e}$  as the input and  $y_2 = \mathbf{Y}_m^T \tilde{\phi} - \mathbf{Y}_u^T \tilde{\phi}_u$  as the output, obtained from Eq.(5.65) when  $K_s$  is uncertain, is passive for sufficiently small  $|\rho_s|$  and relatively small amplitude of bias current excitation.*

**Proof:** The adaptation law in Eqs.(5.57) and (5.26) can be written as

$$\begin{aligned}
\dot{\tilde{a}}_0 &= \gamma_0 \bar{K}_s \bar{e} \\
\dot{\tilde{a}}_i &= \gamma_i [\bar{K}_s + mi^2 \omega^2] \sin(i\omega t) \bar{e}
\end{aligned}$$

$$\begin{aligned}
\dot{\tilde{b}}_i &= \gamma_i [\bar{K}_s + mi^2\omega^2] \cos(i\omega t) \bar{e}, \quad i = 1, 2, \dots, n \\
\dot{\tilde{p}} &= -\gamma_p m\omega^2 \sin(\omega t) \bar{e} \\
\dot{\tilde{q}} &= -\gamma_q m\omega^2 \cos(\omega t) \bar{e}
\end{aligned}$$

It should be noted that  $K_s$  is time varying as shown in Eq.(5.22). We define new variables

$$\begin{aligned}
\rho_i(t) &= \frac{K_s + mi^2\omega^2}{\gamma_i(\bar{K}_s + \bar{m}i^2\omega^2)} > 0 \quad \text{for } i = 0, 1, 2, \dots, n \\
\rho_p &= \frac{1}{\gamma_p} > 0 \quad \rho_q = \frac{1}{\gamma_q} > 0
\end{aligned}$$

For a relatively small bias current excitation we may assume that there exist a constant  $c_1$  such that  $\rho_i(t) > c_1$  for all  $t$ . Therefore, recalling the definition D.1 for a passive system we can obtain

$$\begin{aligned}
\int_0^t y_2 u_2 dt &= \int_0^t [\mathbf{Y}_m^T \tilde{\phi} - \mathbf{Y}_u^T \tilde{\phi}_u] \bar{e} dt \\
&= \int_0^t K_s \tilde{a}_0 \bar{e} dt + \sum_{i=1}^n \left\{ \int_0^t (K_s + mi^2\omega^2) [\tilde{a}_i \sin(i\omega t) \bar{e} + \tilde{b}_i \cos(i\omega t) \bar{e}] dt \right\} - \\
&\quad m\omega^2 \int_0^t \tilde{p} \sin(\omega t) \bar{e} dt - m\omega^2 \int_0^t \tilde{q} \cos(\omega t) \bar{e} dt \\
&= \int_0^t \rho_0 \tilde{a}_0 \dot{\tilde{a}}_0 dt + \sum_{i=1}^n \left\{ \int_0^t \rho_i [\tilde{a}_i \dot{\tilde{a}}_i + \tilde{b}_i \dot{\tilde{b}}_i] dt \right\} + \\
&\quad \rho_p \int_0^t \tilde{p} \dot{\tilde{p}} dt + \rho_q \int_0^t \tilde{q} \dot{\tilde{q}} dt \\
&> W[\tilde{\phi}(t), \phi_u(t), \hat{\phi}_u(t)] - W[\tilde{\phi}(0), \phi_u(0), \hat{\phi}_u(0)]
\end{aligned}$$

where

$$\begin{aligned}
W[\tilde{\phi}(t), \tilde{\phi}_u(t), \hat{\phi}_u(t)] &= \frac{c_1}{2} \tilde{a}_0^2(t) + \sum_{i=1}^n \frac{c_1}{2} [\tilde{a}_i^2(t) + \tilde{b}_i^2(t)] + \\
&\quad \frac{\rho_p}{2} \tilde{p}^2(t) + \frac{\rho_q}{2} \tilde{q}^2(t) \\
W[\tilde{\phi}(0), \tilde{\phi}_u(0), \hat{\phi}_u(0)] &= \frac{c_1}{2} \tilde{a}_0^2(0) + \sum_{i=1}^n \frac{c_1}{2} [\tilde{a}_i^2(0) + \tilde{b}_i^2(0)] + \\
&\quad \frac{\rho_p}{2} \tilde{p}^2(0) + \frac{\rho_q}{2} \tilde{q}^2(0)
\end{aligned}$$

Since  $W[\tilde{\phi}(t), \tilde{\phi}_u(t), \hat{\phi}_u(t)]$  is a positive definite storage function, by definition D.1 the system  $H_2$  is passive.

**Lemma D.4** *The system  $H_2$  that has  $u_2 = \bar{e}$  as the input and  $y_2 = \mathbf{Y}_m^T \tilde{\phi} - \mathbf{Y}_u^T \tilde{\phi}_u - \frac{\rho_c(t)}{\bar{K}_c} \mathbf{Y}_u^T \hat{\phi}_u$  as the output, obtained from Eq.(5.69) when  $K_c$  is uncertain, is passive for a sufficiently small  $|\rho_c|$  and relatively small amplitude of bias current excitation.*

**Proof:** We first define new variables

$$\tilde{\phi}_{u\rho} \triangleq \begin{pmatrix} \tilde{p}_\rho \\ \tilde{q}_\rho \end{pmatrix} = \phi_u - \left(1 - \frac{\rho_c}{\bar{K}_c}\right) \hat{\phi}_u \quad (\text{D.14})$$

Therefore the output equation can be written as  $y_2 = \mathbf{Y}_m^T \tilde{\phi} - \mathbf{Y}_u^T \tilde{\phi}_{u\rho}$ . For sufficiently small  $\rho_c$  we may assume that  $\left(1 - \frac{\rho_c}{\bar{K}_c}\right) > 0$ .

From the adaptation law in Eqs.(5.57) and (5.26) we obtain

$$\begin{aligned} \dot{\tilde{a}}_0 &= \gamma_0 K_s \bar{e} \\ \dot{\tilde{a}}_i &= \gamma_i [K_s + mi^2\omega^2] \sin(i\omega t) \bar{e} \\ \dot{\tilde{b}}_i &= \gamma_i [K_s + mi^2\omega^2] \cos(i\omega t) \bar{e}, \quad i = 1, 2, \dots, n \\ \dot{\tilde{p}} &= -\gamma_p m \left(1 - \frac{\rho_c}{\bar{K}_c}\right) \omega^2 \sin(\omega t) \bar{e} \\ \dot{\tilde{q}} &= -\gamma_q m \left(1 - \frac{\rho_c}{\bar{K}_c}\right) \omega^2 \cos(\omega t) \bar{e} \end{aligned}$$

We further define

$$\begin{aligned} \rho_i(t) &= \frac{K_s + mi^2\omega^2}{\gamma_i(K_s + mi^2\omega^2)} > 0 \quad \text{for } i = 0, 1, 2, \dots, n \\ \rho_p(t) &= \frac{1}{\gamma_p \left(1 - \frac{\rho_c}{\bar{K}_c}\right)} > 0 \quad \rho_q(t) = \frac{1}{\gamma_q \left(1 - \frac{\rho_c}{\bar{K}_c}\right)} > 0 \end{aligned}$$

For a relatively small bias current excitation we may assume that there exist constants  $c_1$ ,  $c_2$ , and  $c_3$  such that  $\rho_i(t) > c_1$ ,  $\rho_p(t) > c_2$ , and  $\rho_q(t) > c_3$  for all  $t$ . Recall the

definition D.1 for a passive system

$$\begin{aligned}
\int_0^t y_2 u_2 dt &= \int_0^t \left[ \mathbf{Y}_m^T \tilde{\phi} - \mathbf{Y}_u^T \tilde{\phi}_{u\rho} \right] \bar{e} dt \\
&= \int_0^t K_s \tilde{a}_0 \bar{e} dt + \sum_{i=1}^n \left\{ \int_0^t (K_s + mi^2 \omega^2) \left[ \tilde{a}_i \sin(i\omega t) \bar{e} + \tilde{b}_i \cos(i\omega t) \bar{e} \right] dt \right\} - \\
&\quad m\omega^2 \int_0^t \tilde{p} \sin(\omega t) \bar{e} dt - m\omega^2 \int_0^t \tilde{q} \cos(\omega t) \bar{e} dt \\
&= \int_0^t \rho_0 \tilde{a}_0 \dot{\tilde{a}}_0 dt + \sum_{i=1}^n \left\{ \int_0^t \rho_i \left[ \tilde{a}_i \dot{\tilde{a}}_i + \tilde{b}_i \dot{\tilde{b}}_i \right] dt \right\} + \\
&\quad \int_0^t \rho_p \tilde{p}_\rho \dot{\tilde{p}}_\rho dt + \int_0^t \rho_q \tilde{q}_\rho \dot{\tilde{q}}_\rho dt \\
&> W[\tilde{\phi}(t), \tilde{\phi}_u(t), \hat{\phi}_u(t)] - W[\tilde{\phi}(0), \tilde{\phi}_u(0), \hat{\phi}_u(0)]
\end{aligned}$$

where

$$\begin{aligned}
W[\tilde{\phi}(t), \tilde{\phi}_u(t), \hat{\phi}_u(t)] &= \frac{c_1}{2} \tilde{a}_0^2(t) + \sum_{i=1}^n \frac{c_1}{2} \left[ \tilde{a}_i^2(t) + \tilde{b}_i^2(t) \right] + \\
&\quad \frac{c_2}{2} \tilde{p}_\rho^2(t) + \frac{c_3}{2} \tilde{q}_\rho^2(t) \\
W[\tilde{\phi}(0), \tilde{\phi}_u(0), \hat{\phi}_u(0)] &= \frac{c_1}{2} \tilde{a}_0^2(0) + \sum_{i=1}^n \frac{c_1}{2} \left[ \tilde{a}_i^2(0) + \tilde{b}_i^2(0) \right] + \\
&\quad \frac{c_2}{2} \tilde{p}_\rho^2(0) + \frac{c_3}{2} \tilde{q}_\rho^2(0)
\end{aligned}$$

Since  $W[\tilde{\phi}(t), \tilde{\phi}_u(t), \hat{\phi}_u(t)]$  is a positive definite storage function, by definition D.1 the system  $H_2$  is passive.

# **BIBLIOGRAPHY**

## BIBLIOGRAPHY

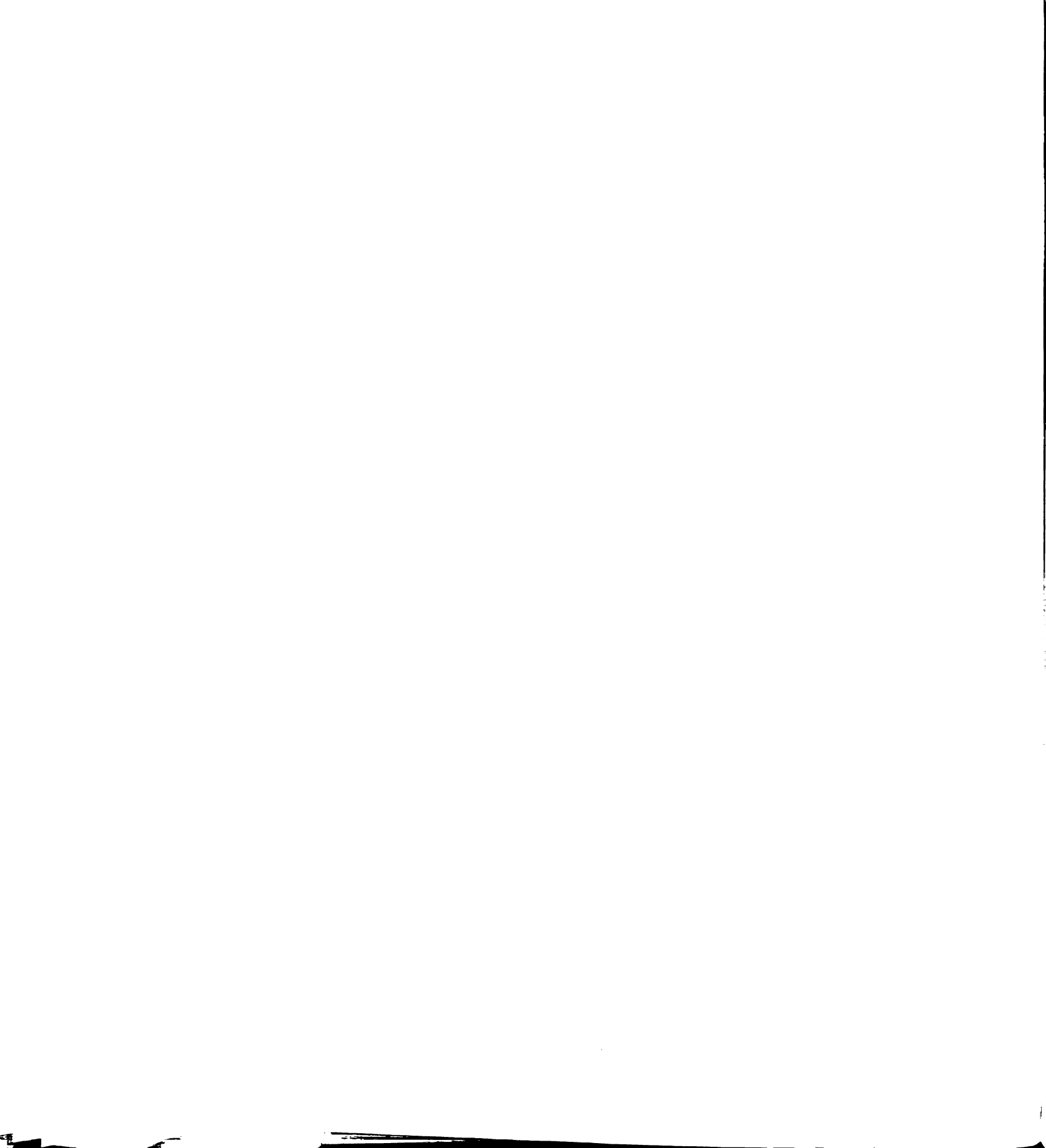
- [1] Advanced Motion Controls PWM Servo Amplifier, *Catalog and Technical Manual 1996*, Camarillo, CA 93012.
- [2] Batty, R., 1988, *Notch Filter Control of Magnetic Bearings*, MS Thesis, Massachusetts Institute of Technology, Cambridge, MA.
- [3] Bleuler, H., Gahler, C., Herzog, R., Larsonneur, R., Mizuno, T., Siegwart, R., and Woo, S. -J., 1994, *Application of Digital Signal Processors for Industrial Magnetic Bearings*, IEEE Transactions on Control Systems Technology, Vol. 2, No. 4, pp. 280-289.
- [4] Chen, D., and Paden, B., 1993, *Adaptive Linearization of Hybrid Step Motors: Stability Analysis*, IEEE Transactions on Automatic Control, Vol. 38, No. 6, pp. 874-887 .
- [5] Childs, D., 1993, *Turbomachinery Rotordynamics: Phenomena, Modeling, and Analysis*, John Wiley & Sons, Inc., New York, NY 10158.
- [6] Fujita, M., Hatake, K., and Matsumura, F., 1993, *Loop Shaping Based Robust Control of a Magnetic Bearing*, IEEE Control Systems, pp. 57-65.
- [7] Herzog, R., Buhler, P., Gahler, C., and Larsonneur, R., 1996, *Unbalance Compensation using Generalized Notch Filters in Multivariable Feedback of Magnetic Bearings*, IEEE Transactions on Control Systems Technology, Vol. 4, No. 5, pp. 580-586.
- [8] Hisatani, M., and Koizumi, T., 1994, *Adaptive Filtering for Unbalance Vibration Suppression*, Proceedings of the Fourth International Symposium on Magnetic Bearings, ETH Zurich, Switzerland.
- [9] Hu, J., and Tomizuka, M., 1993, *A New Plug-in Adaptive Controller for Rejection of Periodic Disturbances*, ASME Journal of Dynamics, Systems, Measurements, and Controls, Vol. 115, pp. 543-546.
- [10] Ioannou, P. A, and Sun, J., 1996, *Robust Adaptive Control*, Prentice Hall, Upper Saddle River, NJ 07458.

- [11] Kanemitsu, Y., Kijimoto, S., Matsuda, K., and Jin, P.T., 1999, *Identification and Control of Unbalance and Sensor Runout on Rigid by Active Magnetic Bearing Systems*, Proceedings of the fifth International Symposium on Magnetic Suspension Technology, Santa Barbara, CA.
- [12] Kaufman, H., Barkana, I., and Sobel, K., 1991, *Direct Adaptive Control Algorithms: Theory and Applications*, Springer-Verlag, New York, NY 10010.
- [13] Khalil, H., 1996, *Nonlinear Systems*, 2nd Edition, Prentice-Hall, Upper Saddle River, NJ 07458.
- [14] Kim, C. -S., and Lee, C. -W., 1997, *In Situ Runout Identification in Active Magnetic Bearing System by Extended Influence Coefficient Method*, IEEE/ASME Transactions on Mechatronics, Vol. 2, No. 1, pp. 51-57.
- [15] Knospe, C. R., 1991, *Stability and Performance of Notch Filters for Unbalance Response*, Proceeding of International Symposium on Magnetic Suspension Technology, NASA Langley Research Center, Hampton, VA, NASA Conference Publication 3152.
- [16] Knospe, C. R., Hope, R. W., Tamer, S. M., and Fedigan, S. J., 1996, *Robustness of Adaptive Unbalance Control of Rotors with Magnetic Bearings*, Journal of Vibration and Control, Vol. 2, pp. 33-52.
- [17] Knospe, C. R., Tamer, S. M., and Fedigan, S. J., 1997, *Robustness of Adaptive Rotor Vibration Control to Structured Uncertainty*, ASME Journal of Dynamics, Systems, Measurements, and Controls, Vol. 119, pp. 243-250.
- [18] Krstic, M., Kanellakopoulos, I., and Kokotovic, P., 1995, *Nonlinear and Adaptive Control Design*, Wiley Interscience, New York, NY.
- [19] Lum, K. -Y., Coppola, V., and Bernstein, D., 1996, *Adaptive Autocentering Control for an Active Magnetic Bearing Supporting a Rotor with Unknown Mass Imbalance*, IEEE Transactions on Control Systems Technology, Vol. 4, No. 5, pp. 587-597.
- [20] Maslen, E. H., Sortore, C. K., and Meeker, D. C., 1997 *Analysis Software for Magnetic Bearing Audits*, ROMAC Laboratories, University of Virginia, Charlottesville, VA 22903.

- [21] Matsumura, F., Fujita, M., and Okawa, K., 1990, *Modeling and Control of Magnetic Bearing Systems Achieving a Rotation Around the Axis of Inertia*, Proceedings of the Second International Symposium on Magnetic Bearings, Tokyo, Japan, pp. 273-280.
- [22] Mizuno, T., and Higuchi, T., 1990, *Design of Magnetic Bearing Controllers Based on Disturbance Estimation*, Proceedings of the Second International Symposium on Magnetic Bearings, Tokyo, Japan, pp. 281-288.
- [23] Mohamed A. M., Matsumura, M., Namerikawa, T., and Lee, J., 1997, *Q-parameterization Control of Vibrations in a Variable Speed Magnetic Bearing*, Proceedings of 1997 IEEE International Conference on Control Applications, Hartford, CT.
- [24] Na, H. -S., and Park, Y., 1997, *An Adaptive Feedforward Controller for Rejection of Periodic Disturbances*, Journal of Sound and Vibration, Vol. 201, No. 4, pp. 427-435.
- [25] Narendra, K. S., and Annaswamy, A. M., 1989, *Stable Adaptive Systems*, Prentice-Hall, Englewood Cliffs, NJ 07632.
- [26] Ogata, K., 1990, *Modern Control Engineering*, 2nd Edition, Prentice-Hall, Englewood Cliffs, NJ 07632.
- [27] Paul, M., Hoffman, W., and Steffani, H. F., 1998, *Compensation for Unbalances with Aid of Neural Networks*, Proceedings of the Sixth International Symposium on Magnetic Bearings, Cambridge, MA.
- [28] Reining, K. D., and Desrochers, A. A., 1986, *Disturbance Accommodating Controllers for Rotating Mechanical Systems*, ASME Journal of Dynamics, Systems, Measurements, and Controls, Vol. 108, pp. 24-31.
- [29] Revolve Technologies Inc., 1997, *Magnetic Bearing Reference, Assembly and Sensor Conditioning Box User Manuals*, Calgary, Alberta, Canada T2R 0B3.
- [30] Rutland, N. K., Keogh, P. S., and Burrows, C. R., 1994, *Comparison of Controller Designs for Attenuation of Vibration in a Rotor Bearing System under Synchronous and Transient Conditions*, Proceedings of the Fourth International Symposium on Magnetic Bearings, ETH Zurich, Switzerland, pp. 107-112.
- [31] Sacks, A., Bodson, M., and Khosla, P., 1996, *Experimental Results of Adaptive Periodic Disturbance Cancellation in a High Performance Magnetic Disk Drive*,

ASME Journal of Dynamics, Systems, Measurements, and Controls, Vol. 118, pp. 416-424.

- [32] Sastry, S., and Bodson, M., 1989, *Adaptive Control: Stability, Convergence, and Robustness*, Prentice-Hall, Englewood Cliffs, NJ 07632.
- [33] Setiawan, J. D., Mukherjee, R., Maslen, E. H., and Song, G., 1999, *Adaptive Compensation of Sensor Runout and Mass Unbalance in Magnetic Bearing Systems*, Proceedings of IEEE/ASME International Conference on Advanced Intelligent Mechatronics, Atlanta, GA.
- [34] Shafai, B., Beale, S., Larocca, P., and Cusson, E., 1994, *Magnetic Bearing Control Systems and Adaptive Forced Balancing*, IEEE Control Systems, Vol. 14, pp.4-13.
- [35] Siegart, R., 1992, *Design and Applications of Active Magnetic Bearings (AMB) for Vibration Control*, Von Karman Institute Fluid Dynamics Lecture Series 1992-06, Vibration and Rotor Dynamics.
- [36] Slotine, J.-J., and Li, W., 1991, *Applied Nonlinear Control*, Prentice-Hall, Englewood Cliffs, NJ 07632.
- [37] Song, G., and Mukherjee, R., 1996, *Integrated Adaptive Robust Control of Active Magnetic Bearings*, IEEE International Conference on System, Man, and Cybernetics, Beijing, China.
- [38] Vidyasagar, M., 1993, *Nonlinear System Analysis*, 2nd Edition, Prentice Hall, Upper Saddle River, NJ 07458.



MICHIGAN STATE LIBRARIES



3 1293 02208 2618